MICROCOPY RESOLUTION TEST CHART
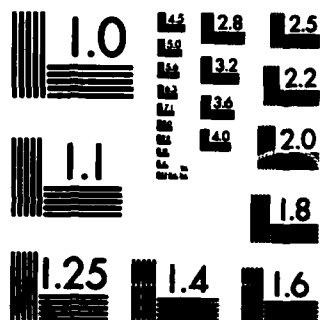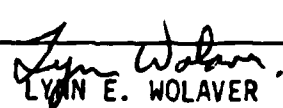
NATIONAL BUREAU OF STANDARDS-1963-A

SECURITY CLASSIFICATION OF THIS PAGE *(When Data Entered)*

REPORT DOCUMENTATION PAGE		READ INSTRUCTIONS BEFORE COMPLETING FORM
1. REPORT NUMBER AFIT/CI/NR 84-35D	**2. GOVT ACCESSION NO.** AD-A145575	**3. RECIPIENT'S CATALOG NUMBER**
4. TITLE *(and Subtitle)* The Saudi Arabian Heat Low: A Numerical Perspective		**5. TYPE OF REPORT & PERIOD COVERED** THESIS/DISSERTATION
		6. PERFORMING ORG. REPORT NUMBER
7. AUTHOR(s) Larry E. Freeman		**8. CONTRACT OR GRANT NUMBER(s)**
9. PERFORMING ORGANIZATION NAME AND ADDRESS AFIT STUDENT AT: Colorado State University		**10. PROGRAM ELEMENT, PROJECT, TASK AREA & WORK UNIT NUMBERS**
11. CONTROLLING OFFICE NAME AND ADDRESS AFIT/NR WPAFB OH 45433		**12. REPORT DATE** 1984
		13. NUMBER OF PAGES 203
14. MONITORING AGENCY NAME & ADDRESS *(if different from Controlling Office)*		**15. SECURITY CLASS.** *(of this report)* UNCLASS
		15a. DECLASSIFICATION/DOWNGRADING SCHEDULE

16. DISTRIBUTION STATEMENT *(of this Report)*

APPROVED FOR PUBLIC RELEASE; DISTRIBUTION UNLIMITED

DTIC
ELECTE
SEP 17 1984
B

17. DISTRIBUTION STATEMENT *(of the abstract entered in Block 20, if different from Report)*

18. SUPPLEMENTARY NOTES

APPROVED FOR PUBLIC RELEASE: IAW AFR 190-1

LYNN E. WOLAVER
Dean for Research and
Professional Development
2 Jul 84 AFIT, Wright-Patterson AFB OH

19. KEY WORDS *(Continue on reverse side if necessary and identify by block number)*

20. ABSTRACT *(Continue on reverse side if necessary and identify by block number)*

ATTACHED

DD $_{1\ JAN\ 73}^{FORM}$ 1473   EDITION OF 1 NOV 55 IS OBSOLETE   UNCLASS

SECURITY CLASSIFICATION OF THIS PAGE *(When Data Entered)*

84 09 13 009

AFIT RESEARCH ASSESSMENT

The purpose of this questionnaire is to ascertain the value and/or contribution of research accomplished by students or faculty of the Air Force Institute of Technology (AU). It would be greatly appreciated if you would complete the following questionnaire and return it to:

AFIT/NR
Wright-Patterson AFB OH 45433

RESEARCH TITLE: _The Saudi Arabian Heat Low: A Numerical Perspective_

AUTHOR: _Larry E. Freeman_

RESEARCH ASSESSMENT QUESTIONS:

1. Did this research contribute to a current Air Force project?

( ) a. YES   ( ) b. NO

2. Do you believe this research topic is significant enough that it would have been researched (or contracted) by your organization or another agency if AFIT had not?

( ) a. YES   ( ) b. NO

3. The benefits of AFIT research can often be expressed by the equivalent value that your agency achieved/received by virtue of AFIT performing the research. Can you estimate what this research would have cost if it had been accomplished under contract or if it had been done in-house in terms of manpower and/or dollars?

( ) a. MAN-YEARS _____   ( ) b. $_____

4. Often it is not possible to attach equivalent dollar values to research, although the results of the research may, in fact, be important. Whether or not you were able to establish an equivalent value for this research (3. above), what is your estimate of its significance?

( ) a. HIGHLY   ( ) b. SIGNIFICANT   ( ) c. SLIGHTLY   ( ) d. OF NO
      SIGNIFICANT   SIGNIFICANT   SIGNIFICANCE

5. AFIT welcomes any further comments you may have on the above questions, or any additional details concerning the current application, future potential, or other value of this research. Please use the bottom part of this questionnaire for your statement(s).

NAME   GRADE   POSITION

ORGANIZATION   LOCATION

STATEMENT(s):

AFIT/NR
WRIGHT-PATTERSON AFB OH 45433

OFFICIAL BUSINESS
PENALTY FOR PRIVATE USE. $300

NO POSTAGE
NECESSARY
IF MAILED
IN THE
UNITED STATES

BUSINESS REPLY MAIL
FIRST CLASS   PERMIT NO. 73236   WASHINGTON D.C.

POSTAGE WILL BE PAID BY ADDRESSEE

AFIT/ DAA
Wright-Patterson AFB OH 45433

ABSTRACT: Results are presented from several numerical experiments designed to simulate the Saudi Arabian "heat low" and to test the sensitivity of the "heat low" circulation to certain parameters. Data collected during the Summer Monsoon Experiment (1979) are analyzed to obtain vertical and temporal distributions of temperature, water vapor mixing ratio, and dust mass loading. These distributions, along with climatological vertical profiles of ozone and carbon dioxide, are used as input to broadband longwave and shortwave radiative transfer routines to obtain radiative heating rates over the Saudi Arabian desert and the western Arabian Sea for both clear and dust laden conditions. The magnitude of the surface sensible heat flux over the desert is parameterized by the net radiation at the desert surface. The sensible heat is vertically distributed over the desert according to the diurnal pattern of mixed layer growth as determined by a 1-dimensional mixed layer growth model. The horizontal gradients in the vertical distributions of radiative and sensible heating between the desert and the ocean are used to force a 2-dimensional, axisymmetric, dry, primitive equation model to simulate the "heat low" circulation. Results indicate that although the presence of dust is capable of producing a significant increase in the midday radiative heating of the middle troposphere, the impact of the elevated radiative heat source on the induced "heat low" circulation is small. The late afternoon low level cyclonic circulation over the desert has a vertical extent of ~300 mb and is characterized by upward vertical motion from the surface to near 500 mb.

PRIMARY REFERENCES:

Ackerman, S. A., and S. K. Cox, 1982: The Saudi Arabian heat low: aerosol distributions and thermodynamic structure. *J. Geophys. Res.* 87, C11, 8991-9002.

Ackerman, S. A., E. A. Smith and S. K. Cox, 1983: Surface and atmospheric radiative exchange over the Arabian Peninsula, Preprint Volume of Fifth Conference on Atmospheric Radiation, 31 October - 4 November, 1983, Baltimore, Maryland, 481-483.

Cox, S. K., M. C. Polifka, K. Griffith, A. Rockwood, and D. Starr, 1976: Radiative transfer computational routines for atmospheric science applications. Atmospheric Science Research Report, Colorado State University, Fort Collins, CO., 75 pp.

Hack, J. J., and W. H Schubert, 1976: Design of an axisymmetric primitive equation tropical cyclone model. *Atmospheric Science Paper*, #263, Colorado State University, Fort Collins, CO., 70 pp.

Lilly, D. K., 1968: Models of cloud-topped mixed layers under a strong inversion. *Quart. J. Roy. Meteorol. Soc.*, 94, 292-309.

DISSERTATION

THE SAUDI ARABIAN HEAT LOW: A NUMERICAL PERSPECTIVE

Submitted by

Larry Eugene Freeman

Atmospheric Science Department

In partial fulfillment of the requirements

for the Degree of Doctor of Philosophy

Colorado State University

Fort Collins, Colorado

Summer, 1984

84 09 13 009

COLORADO STATE UNIVERSITY

June 4, 1984

WE HEREBY RECOMMEND THAT THE DISSERTATION PREPARED UNDER

OUR SUPERVISION BY Larry Eugene Freeman

ENTITLED The Saudi Arabian Heat Low: A Numerical Perspective

BE ACCEPTED AS FULFILLING IN PART REQUIREMENTS FOR THE DEGREE OF

Doctor of Philosophy

Committee on Graduate Work

Adviser

Department Head

ABSTRACT

THE SAUDI ARABIAN HEAT LOW: A NUMERICAL PERSPECTIVE

Results are presented from several numerical experiments designed to simulate the Saudi Arabian "heat low" and to test the sensitivity of the "heat low" circulation to certain parameters. Data collected during the Summer Monsoon Experiment (1979) are analyzed to obtain vertical and temporal distributions of temperature, water vapor mixing ratio, and dust mass loading. These distributions, along with climatological vertical profiles of ozone and carbon dioxide, are used as input to broadband longwave and shortwave radiative transfer routines to obtain radiative heating rates over the Saudi Arabian desert and the western Arabian Sea for both clear and dust laden conditions. The magnitude of the surface sensible heat flux over the desert is parameterized by the net radiation at the desert surface. The sensible heat is vertically distributed over the desert according to the diurnal pattern of mixed layer growth as determined by a 1-dimensional mixed layer growth model.

The horizontal gradients in the vertical distributions of radiative and sensible heating between the desert and the ocean are used to force a 2-dimensional, axisymmetric, dry, primitive equation model to simulate the "heat low" circulation. Results indicate the desert surface sensible heat flux is the most important component in producing a realistic surface pressure gradient between the desert "heat low" and the adjacent ocean. Although the presence of dust is

capable of producing a significant increase in the midday radiative heating of the middle troposphere, the impact of the elevated radiative heat source on the induced "heat low" circulation is small. The diurnal character of the circulation exhibits a surface pressure minimum in the "heat low" near 1600L. However, the maximum in tangential wind occurs about 6 hours later. The late afternoon low level cyclonic circulation over the desert has a vertical extent of ~300 mb and is characterized by upward vertical motion from the surface to near 500 mb. Strong radiational cooling over the ocean surface dominates the low level temperature field and induces a long term downward trend. It is surmized that the inability to include external influences in the 2-dimensional model is responsible for this trend.

A 3-dimensional equatorial beta plane model which is solved using transforms in all three spatial coordinates is unsuccessfully employed to try to determine the impact of the Sahara desert on the locally induced "heat low" circulation over Saudi Arabia. Results from two experiments indicate the vertical transform technique employed in the model may be ill-suited to applications where complete vertical stratification is desired.

Larry Eugene Freeman
Atmospheric Science Department
Colorado State University
Fort Collins, Colorado 80523
Summer, 1984

ACKNOWLEDGMENTS

I am pleased to express my sincere gratitude to several people who made significant contributions to this research effort. Dr. Stephen K. Cox not only supplied computer resources and financial support, but also provided invaluable guidance and direction as my major professor and adviser. Dr. Wayne H. Schubert was very patient and extremely enlightening during many hours of consultation. I also thank Dr. Thomas B. McKee and Dr. H. Howard Frisinger for their comments during several committee meetings and for their thoughtful review of this research. Mr. Steven A. Ackerman and Dr. John M. Davis provided a great deal of information and assistance during numerous impromptu periods of discussion. A special debt is owed Ms. Melissa Tucker for her expert typing of all the drafts and the final version of this manuscript. Ms. Judy Sorbie drafted many of the figures which appear in this dissertation.

I am especially grateful to my wife, Ann, and to my son, Clayton, who were extremely supportive and understanding during this period of graduate study. They were often called upon and always found willing to make personal sacrifices in the interest of completing this research project. It was their unfaltering encouragement which allowed me to persevere through what seemed to be some rather dismal times.

TABLE OF CONTENTS

TABLE OF CONTENTS (Continued)

LIST OF TABLES

LIST OF FIGURES

LIST OF FIGURES (Continued)

I. INTRODUCTION

That region of the world bounded by east Africa on the west, Indochina on the east, the 30° south latitude belt and the 30° north latitude belt experiences perhaps the most dramatic annual meteorological cycle on earth. That cycle - known as the Southwest Indian Monsoon - is characterized by very large scale flow patterns which produce enormous amounts of precipitation over the Indian sub-continent in the wet summer season and very little precipitation during the dry winter. In fact, more than 75% of the annual rainfall over India occurs during the period from mid-June through late August (Ramage, 1971). The flows which produce this summer circulation originate in the southeasterly trades of the equatorial Southern Indian Ocean. As the airflow approaches the East African coast and crosses the equator into the northern hemisphere, the wind direction shifts to southerly. Along the coast of Somali, this flow becomes southwesterly and very strong with surface winds speeds of 10-15 m/s being sustained in that region throughout the summer months. This low-level southwesterly flow then proceeds across the Arabian Sea and into the Indian sub-continent where moisture is released in the form of torrential summer down pours (Trewartha and Horn, 1980). The northwestern portion of this region of the world is dominated by deserts which stretch westward from northwest India and Pakistan across Afghanistan, Iran, Iraq, Saudi Arabia and North Africa. During

the summer months, these deserts are characterized by a set of well developed, low level thermally induced pressure troughs known as "heat lows". These "heat lows" generally appear by late April, intensify through mid-July, then weaken through mid-September when they begin to disappear (Ramage, 1971). The vertical extent of these "heat lows" is thought to be very shallow. Rao (1976) describes the "heat low" over northwest India as extending about 1.5 km vertically and being capped by a very deep well-marked ridge which is assumed to be a part of the sub-tropical high pressure belt. In the region of the "heat lows", surface solar insolation is unimpeded by the presence of clouds. As a result, large amounts of sensible heat are transferred from the surface to the atmosphere in these desert "heat lows".

The relationship between the formation, duration, and intensity of these "heat lows" and the onset, duration, and intensity of the summer monsoonal circulation has long been a topic of conjecture. In one attempt to correlate the intensity of the "heat low" with monsoon activity, Ramage (1971) showed that the surface pressure at Jacobabad, Pakistan - near the center of the Pakistani "heat low" - was inversely related to the monsoon rains over a strip of the Indian sub-continent lying between 18° and 27° N. For the years 1962-1964, his results indicated that when the surface pressure within the Pakistani "heat low" decreased, the rainfall over India increased and vice-versa. In addition, he used results from Dixit and Jones (1965) to show that when the monsoon rains were intensified, the middle and upper tropospheric temperatures over the "heat low" were 2-6° C higher than during periods of weak rainfall. Ramage suggests that the increase in rainfall caused an increase in the middle and upper

tropospheric subsidence over the "heat low" and therefore caused a warming of the middle and upper troposphere and a reduction of the surface pressure in the "heat low". Rao (1976) argues that this correlation between the intensity of the "heat low" and the intensity of the monsoon rains may be related to the passage of middle to upper tropospheric troughs in the mid-latitude westerlies. The southern portions of such troughs are capable of causing an increase in the intensity of rainfall over India. Also, because these troughs would tend to weaken the middle to upper tropospheric ridge over the "heat low" and allow the pressure in the "heat low" to fall, it may then appear that the increase in rainfall and decrease in surface pressure were cause and effect related when in fact both effects were caused by the passage of an upper tropospheric trough. With some certainty the regions of the "heat lows" can be considered large sources of sensible heat for the atmosphere. However, whether the "heat lows" interact with the monsoon disturbances which bring the life giving rains to much of South Asia is as yet an unsolved problem.

In order to better our understanding of the summer monsoon circulation, an international experiment was conducted during the period May 1 - September 1, 1979, to investigate the heat balance, energetics, and kinetics of the circulation. The scientific objectives of this summer monsoon experiment (Summer MONEX) were separated into planetary-scale aspects and synoptic-scale regional aspects. Investigations of heat sources, onset of the monsoon, and breaks in the monsoon were included in the planetary scale aspects. The synoptic-scale regional aspects were investigated in an Arabian Sea Experiment and a Bay of Bengal Experiment. The latter experiment

was designed to investigate specifically the structure and dynamics of the monsoon depressions, troughs and other moist convective phenomena associated with the summer monsoon circulation. However, the Arabian Sea Experiment concerned itself with the physical mechanisms which drive the monsoonal circulation over the Arabian Sea and the synoptic-scale features which result from that circulation. One phase of this experiment was conducted from May 1 - May 15, 1979 and was entitled the Saudi Arabian Heat Source Experiment. This experiment was specifically designed to investigate the heat sources at the surface, within the atmosphere, and at the top of the atmosphere over Saudi Arabia and the western Arabian Sea (Summer MONEX Field Phase Report, 1981). This Pre-Onset Phase of Summer MONEX consisted mainly of flights over the Saudi Arabian desert and the Arabian Sea by a heavily instrumented Convair 990 aircraft. The aircraft not only made periodic descents through the atmosphere, but also made dropwindsonde observations of the vertical structure of the atmosphere over the desert and the adjacent ocean region. Most of the effort within the scientific community to date with regards to this data set has been diagnostic in nature.

One of the significant early findings of the analysis of this data set was the presence of an extensive layer of dust over the Saudi Arabian peninsula and the western Arabian Sea. The dust was found to exist as high as the ~525 mb level over the desert and ~580 mb level over the ocean. The dust particles which comprised this aerosol layer were found to range in size from about 0.8 microns to about 20 microns with maximum concentrations near 3 microns. The concentration of dust particles was found to decrease with increasing altitude.

Preliminary results indicated that this deep aerosol layer was radiatively active in the shortwave portion of the spectrum (Ackerman and Cox, 1982). Also, chemical analysis of the aerosol seemed to point to a local source region for the dust (Patterson et al., 1983). The thermodynamic structure of the Saudi Arabian "heat low" indicated a well mixed layer with a nearly constant potential temperature profile extending from the surface to ~650 mb (Ackerman and Cox, 1982; Blake et al., 1983). These initial findings seemed to raise a question about whether the classic concept of a shallow "heat low" is correct. If the "heat low" is characterized by a shallow layer of upward vertical motion with subsidence aloft, how could the dust be resident through the lower half of the troposphere and why would the potential temperature profile indicate a well mixed layer some 350-400 mb deep?

In order to examine the impact of the dust layer on the dynamics of a thermally induced circulation, and to try to make a first step toward answering the questions concerning the dynamics of the "heat low", a series of numerical experiments was undertaken. The basic concept behind these numerical experiments was to use the data collected during the Pre-Onset Saudi Arabian Phase of the Summer MONEX to determine realistic heating gradients between the desert region and the adjacent ocean area and to use these realistic gradients in numerical experiments to determine what the induced circulation would be. Toward that end, three numerical models were used in this study. The first model is a 1-dimensional model which was used to determine the diurnal pattern of mixed layer growth over the desert. The second model is a 2-dimensional, axisymmetric, primitive equation model which

was used to determine the 2-dimensional circulation which would be induced by the desert-ocean gradients in heating. This model has 15 discreet layers in the vertical with each layer representing approximately 60 mb in pressure. Finally, a 3-dimensional model developed on an equatorial beta plane and solved using transform techniques was employed to try to examine the impact on the induced 2-dimensional circulation of a large desert region external to the 2-dimensional domain. This thesis describes the analysis efforts which yielded the appropriate horizontal gradients in heating, the three numerical models which were employed, and the results from the modelling efforts.

In Chapter 2, the collection of the data which was used in this study is described. The analysis techniques which were employed to determine the vertical structure of the atmospheric state parameters such as temperature, moisture, and the radiatively active gases and dust are presented. The resulting vertical profiles of these state parameters for the desert and the ocean are then employed to determine the thermal forcing gradients. The method of determining the radiative heating component of the thermal forcing and the resulting vertical profiles of radiative heating as a function of time of day for both the desert and the ocean are described in Chapter 3. Also included in this chapter is the horizontal specification of the heating gradient between the desert profiles and the ocean profiles which were used in the 2-dimensional numerical model. The determination of the sensible heating component of the thermal forcing is described in Chapter 4. In order to determine the appropriate vertical distribution of sensible heating, a 1-dimensional numerical

model of the mixed layer depth was employed. A description of this model is included in Chapter 4. Chapter 5 contains detailed information of the structure of the 2-dimensional model as well as a description of the results from the experiments conducted with that model. At the end of this chapter is a brief summary of results and comparison with observations. Chapter 6 contains the same information for the 3-dimensional model. Finally, a summary of the analysis effort and some conclusions are presented in Chapter 7.

II. OBSERVATIONAL DATA

1.0 Collection of Data

As was stated in Chapter 1, one of the goals of the Pre-Onset Phase of the Summer MONEX was to try to understand the nature of the heat source over Saudi Arabia. Toward that end, during the period 6 May - 14 May 1979, several aircraft flights were conducted over the Rub'al Khali Desert of Saudi Arabia. The aircraft was a heavily instrumented NASA Convair 990 which operated out of Dhahran, Saudi Arabia. The 990 carried a dropwindsonde system to determine vertical profiles of pressure, temperature, relative humidity, and winds, Particle Measuring Systems Probes, .3 - 2.8 μm and .7 - 2.8 μm pyranometers, 4-50 μm pyrgeometers, as well as other particle and radiation sensors (Bolhofer et al., 1981). A typical flight path is shown in Figure 2.1. On this day, 12 May 79, the 990 left Dhahran at about 05:30L and flew several different paths over the desert returning to Dhahran at about 11:15L. As with most of the missions, the aircraft performed one stairstep descent to within about .5 km of the desert surface during the middle of the flight. This descent was accomplished to allow for a determination of the vertical structure of the prevailing atmospheric conditions. In addition, 10 dropwindsondes were launched from high altitudes at various locations over the desert. The flights conducted on May 9 and May 10 were very similar to the flight path on May 12 except that the 9 and 10 May flights were conducted somewhat later in the day. On May 6 and May 14, the flight
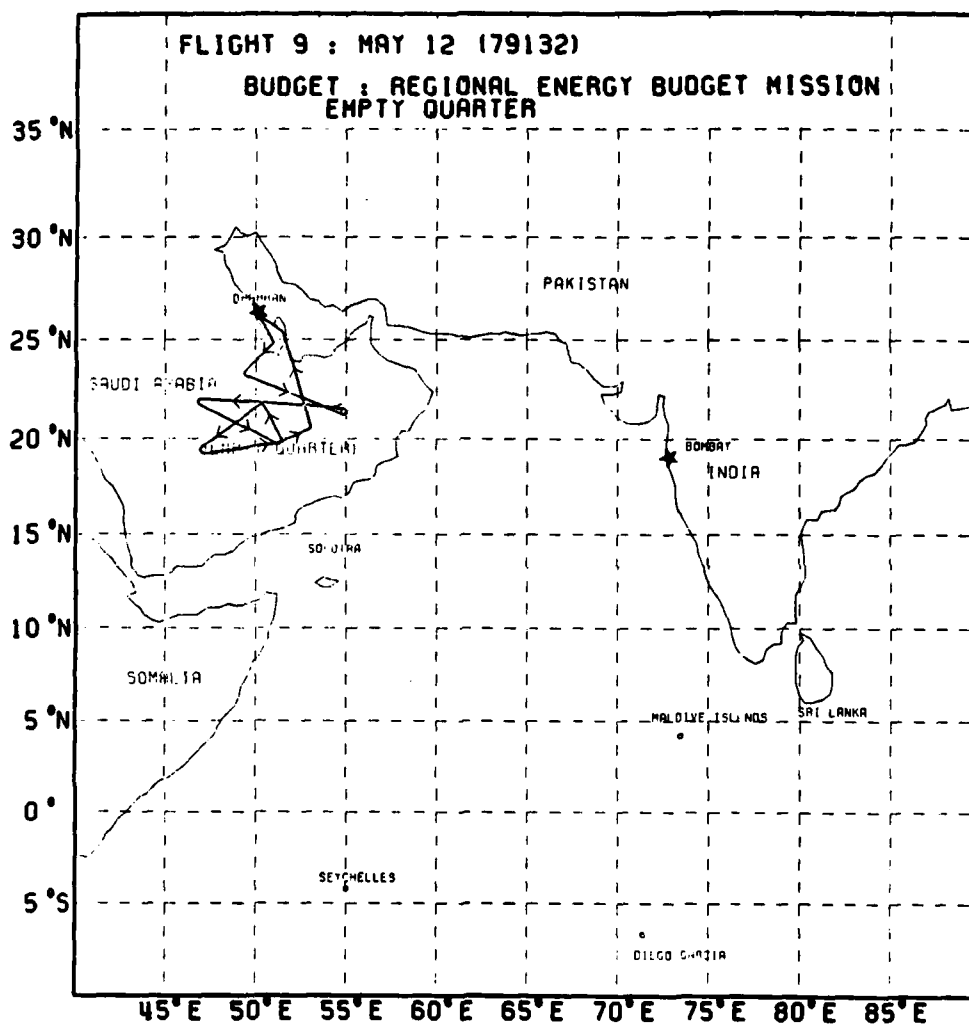
Figure 2.1 A typical flight path for the NASA Convair 990 during the Pre-Onset Phase of Summer MONEX (from Smith et al., 1980).

path included a leg over the western Arabian Sea so that the contrast between the ocean and desert could be determined. In addition a mission was conducted entirely over the Arabian Sea on 31 May 79 (Smith et al., 1980). It was the data collected during these aircraft flights which provided the main source of observational information for this study.

A second data source was available from an experiment conducted in the summer of 1981. During May and June of 1981, an instrumented surface station was placed at various locations in the Saudi Arabian desert. A schematic of the station is shown in Figure 2.2 (Smith et al., 1981a). The data from this surface station were used to supplement the data collected by the aircraft.

2.0 Data Analysis

The goal of the analysis effort was to produce reasonably accurate vertical profiles of temperature, water vapor mixing ratio, and dust mass loading. These data were required in order to determine the radiative heating component of the thermal forcing for the numerical models. The data were analyzed to obtain a diurnal representation in time and a desert-ocean contrast in space. It should be mentioned that the analysis of the dust mass loading was required in order to determine the impact of the dust on the thermal forcing.

The first step in the analysis process was to divide the dropwindsonde data into two categories according to whether or not the drop was made over the desert or over the ocean. There were 52 useable dropwindsonde data sets out of a total of 58 drops made. Of these 52, 18 were drops over the ocean and 34 were drops over the
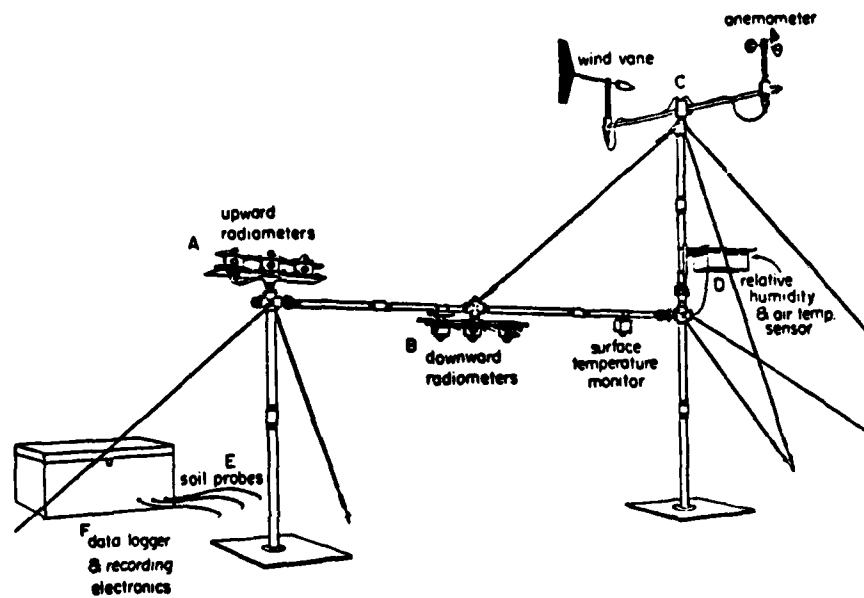
Figure 2.2 Schematic of the surface based observing station used during June 1981 in the Saudi Arabian desert (from Smith et al., 1981a).

desert. The dropwindsonde data consisted of pressure, temperature, dew point temperature, water vapor mixing ratio, wind direction and wind speed at about 5 mb increments from the aircraft flight level to about 950 mb. The reason for the termination of data above the surface was that the technique used to analyze the dropwindsonde signals required a continuous signal for some time increment above and below the level at which the data were being analyzed. Consequently, it was not possible to obtain data near the surface using the dropwindsonde because the unit itself impacted the surface before the required signal time had elapsed. The dropwindsonde data were analyzed at discrete pressure levels corresponding to the 15 layers in the 2-dimensional model.

By examining drops made over the desert at different times on a single day, it was apparent that the temperature above about 860 mb was relatively constant and did not vary a great deal diurnally. Only the temperatures below that level showed marked diurnal variation with the greater variability occurring at the lower levels. Since the dropwindsonde data did not reach the surface, data from the surface station were used to determine the air temperature near the surface and the actual temperature of the surface. From 860 mb to the aircraft flight level, the temperature profile was assumed to be constant in time. The profile was determined simply by averaging all the drop data over the desert at each pressure level. Below 860 mb, the desert drops were classified according to the time of day. A mean temperature for each quadrant of the day was obtained by averaging all the drops made within the quadrant. Then, a simple interpolation was accomplished to obtain the diurnal trace of temperature. At the

surface, the diurnal traces of air and surface temperature were obtained from the surface station data. Therefore, a vertical profile of temperature over the desert was available for each of the 24 hours of the day from the surface to the aircraft flight level. Over the ocean, the diurnal temperature changes were considered to be very small at all levels and therefore, only one vertical profile of temperature was obtained by averaging all available dropwindsonde data at each pressure level. The surface temperature of the ocean was fixed at 29°C based on the results of the Indian Ocean Expedition (Meteorological Atlas, 1972). Above the aircraft flight level in both the desert and ocean profiles, climatological data were used from a standard tropical atmosphere (McClatchey et al., 1972). The resulting temperature profiles are given in Table 2.1.

A vertical profile of water vapor mixing ratio was obtained for the desert and the ocean by averaging all available drops in each category. The diurnal variation in water vapor mixing ratio was assumed to be very small over the desert and over the ocean. The resulting water vapor mixing ratio profiles are shown in Figure 2.3 for both the desert and the ocean. Also shown is the climatological profile of water vapor mixing ratio from a Mid-Latitude Summer Atmosphere (McClatchey et al., 1972). Between 550 mb and 900 mb, the desert moisture profile indicates higher mixing ratios than over the ocean. In the lowest 100 mb, however, the mixing ratios over the ocean are considerably higher than over the desert. In addition, both the desert and ocean profiles are more moist than the mid-latitude summer climatological profile between 400 mb and 700 mb. In order to verify the dropwindsonde moisture profiles at mid-levels over the

TABLE 2.1a

Vertical temperature profiles for the desert and the ocean.
Temperatures are degrees Celsius.

	Desert		Ocean	
P(mb)	T_{sfc}	T_{air}	T_{sfc}	T_{air}
1010	See Diurnal Range in Table 2.1b		29.0	29.0
950	See Diurnal Range in Table 2.1b			24.6
890	See Diurnal Range in Table 2.1b			25.2
830		22.8		22.2
770		16.8		17.4
710		11.8		11.9
650		5.8		6.5
590		-1.2		1.5
530		-5.2		-2.9
470		-10.2		-8.9
410		-17.2		-16.5
350		-26.2		-25.9
290		-36.2		-34.6
230		-48.2		-46.2
170		-59.2		-59.2
110		-76.2		-76.2
60		-68.2		-68.2
30		-54.2		-54.2
6		-30.2		-30.2
1.6		-8.2		-8.2

TABLE 2.1b

Diurnal variation of temperature for the surface and the three lowest
layers of the atmosphere.   Temperatures are degrees Celsius.

	1010 mb		950 mb	890 mb
	T_{sfc}	T_{air}		
00	28.4	27.8	32.7	28.8
01	26.9	26.7	32.6	28.7
02	25.3	25.0	32.4	28.6
03	24.3	24.0	32.2	28.5
04	23.7	23.0	31.8	28.4
05	23.0	22.5	31.7	28.3
06	22.7	22.0	31.5	28.2
07	26.9	27.0	31.7	28.3
08	31.6	30.7	31.9	28.4
09	38.5	37.8	32.4	28.4
10	47.2	39.8	32.6	28.5
11	53.5	40.5	32.9	28.6
12	56.4	41.0	33.2	28.7
13	57.4	41.4	33.6	28.8
14	56.9	41.7	33.8	28.9
15	55.5	41.5	34.2	29.0
16	54.0	41.0	34.6	29.1
17	50.6	39.9	34.8	29.2
18	45.8	38.0	35.0	29.4
19	39.9	35.5	34.8	29.3
20	35.7	33.6	34.3	29.2
21	33.6	31.7	33.8	29.1
22	31.9	30.7	33.5	29.0
23	30.4	28.7	33.1	28.9
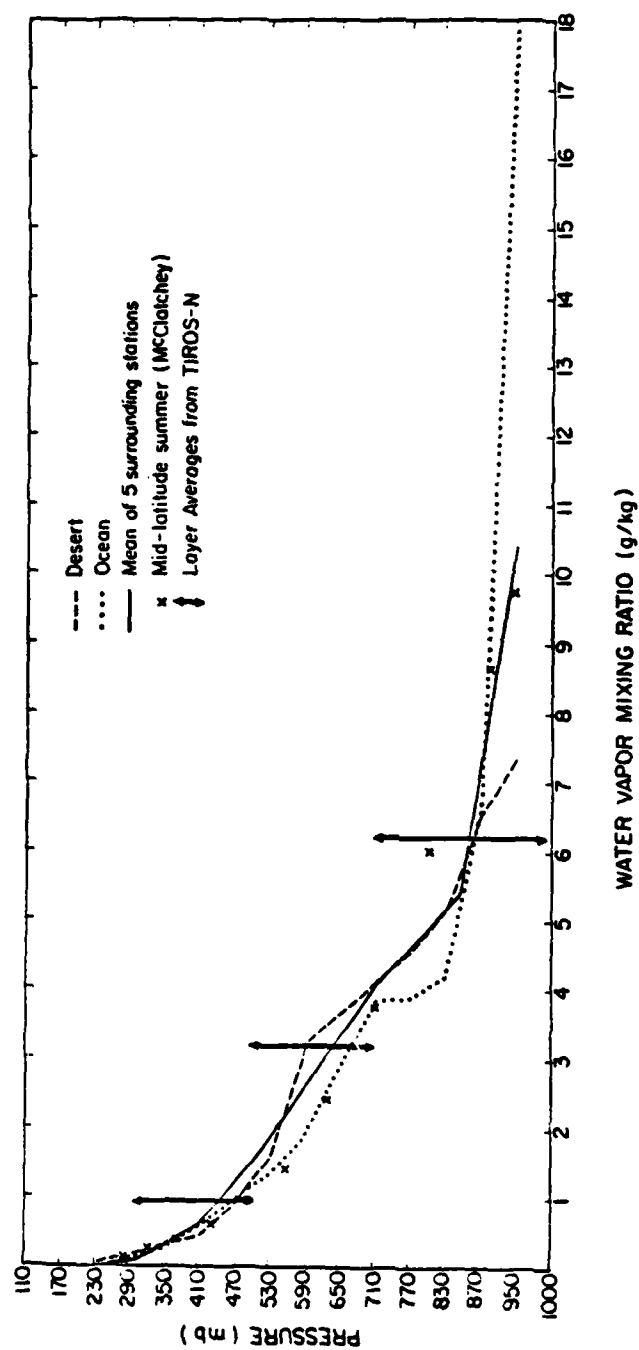
Figure 2.3 Vertical profiles of water vapor mixing ratio from dropwindsondes (desert, ocean), radiosondes (five surrounding stations), climatology (mid-latitude summer), and satellite (TIROS-N).

desert, an analysis of available upper air observations from regularly reporting radiosonde stations located near the desert was undertaken. The moisture data from five radiosonde stations for the second week of May in the years 1976, 1977, and 1978 were obtained from the Northern Hemisphere Data Tabulations. The stations and their locations are given in Table 2.2. The mean mixing ratio for this time period and for these five stations were obtained at each of the mandatory reporting levels. The result is plotted in Figure 2.3. The mean profile is in good agreement with both the desert and ocean profiles determined from the dropwindsonde data. A final check on the moisture profiles was provided by examining data collected by the TIROS-N satellite. One of the products available from the TIROS Operational Vertical Sounder is the layer precipitable water for three layers: the surface to 700 mb, 700-500 mb, and 500-300 mb. By multiplying the precipitable water for a given layer by the density of water, an optical mass can be obtained for the layer. It is then possible to compute a mean mixing ratio for that layer using the relation

$$\bar{q} = U_m \frac{g}{\Delta p} \qquad (2.2.1)$$

where $\bar{q}$ is the mean mixing ratio of the layer, U_m is the optical mass of the layer (equal to the precipitable water), g is the acceleration of gravity (9.81 m s^{-2}), and Δp is the pressure difference between the bottom and top of the layer. The available TIROS-N soundings for the period 6-14 May 79 were analyzed in this manner to obtain mean mixing ratios for the three layers. The results are plotted in Figure 2.3 at the midpoint of the layer with the arrows representing the layer over which the mean mixing ratio is applicable.

TABLE 2.2

Names and locations of the stations used to determine the mean
vertical profile of the water vapor mixing ratio for the years
1976-1978.

Station	Latitude ($^\circ$N)	Longitude ($^\circ$E)
Khamis Musheit	18.1	42.5
Jeddah	21.3	39.1
Gizan	16.5	42.4
Riyadh	24.4	46.4
Dhaharan	26.2	50.1

The agreement of this TIROS-N data with the dropwindsonde derived desert and ocean profiles and with the radiosonde derived mean mixing ratio profiles is apparent.

The dust mass loading was determined by using data collected by the Particle Measuring Systems Probes. Ackerman and Cox (1982) reported the dust mass loading as a function of height for flights over the desert on 9, 10, 12, and 14 May 79 and a flight over the ocean on 31 May 79. The mean dust mass loading profiles for the desert flights and the ocean flight are shown in Figure 2.4. It is important to note the differences between the profiles over the ocean and over the desert. The abscissa is a logarithmic scale. The maximum dust mass loading in the lowest layers over the desert is about five times as great as the low level oceanic dust mass loading. Above about 590 mb, the dust mass loading over the ocean and over the desert is very small. At 590 mb, the dust mass loading over the desert is twice as large as in the oceanic atmosphere. These profiles were used to describe the vertical structure of the dust over the desert and over the ocean.

In addition to the vertical profiles of temperature, water vapor mixing ratio, and dust mass loading, it was necessary to determine vertical profiles of carbon dioxide and ozone. These constituents are very important when determining the radiative heating component of the thermal forcing. Since no observations of either were available, climatological profiles were employed. The ozone profiles were determined by using mean tropical atmosphere profiles (McClatchey, 1972). The ozone profile is given in Table 2.3. Carbon dioxide
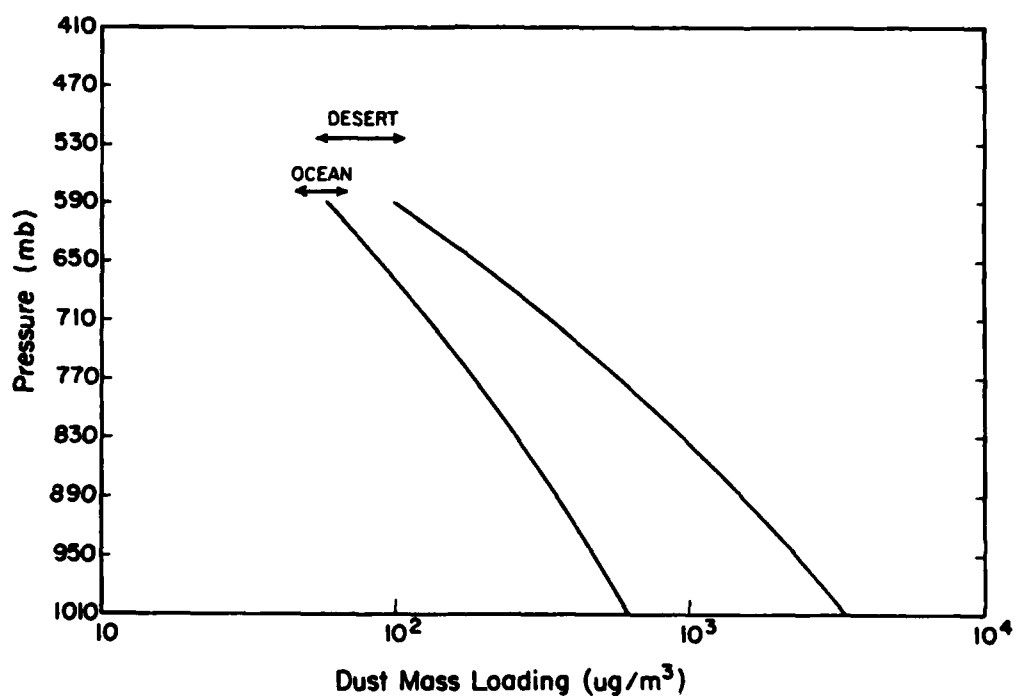
Figure 2.4 Mean vertical profiles of dust mass loading over the Saudi Arabian desert and over the western Arabian Sea during the Pre-Onset Phase of Summer MONEX (from Ackerman and Cox, 1982).

TABLE 2.3

Climatological vertical profile of ozone mxing ratio from McClatchey
et.al., 1972.

P(mb)	O_3 (ug/g)
1010	.051
950	.051
890	.053
830	.055
770	.056
710	.058
650	.059
590	.061
530	.064
470	.067
410	.072
350	.079
290	.092
230	.119
170	.163
110	.238
60	1.574
30	7.138
6	80.465
1.6	6.199

concentration was considered to be invariant in space and time and the mixing ratio was fixed at .486 g kg^{-1}.

The results of this analysis effort were vertical profiles of temperature, water vapor mixing ratio, carbon dioxide mixing ratio, and ozone mixing ratio over the desert and over the adjacent ocean. Because of strong diurnal variations near the surface, a vertical profile was produced for each hour of the day over the desert--24 profiles in all. Over the ocean, where diurnal variations are relatively insignificant, only one vertical profile was determined. In addition, a mean vertical profile of dust mass loading was determined for the desert and for the ocean. As will be explained in Chapter 3, these profiles were used as input to radiative transfer routines to compute the radiative heating component of the thermal forcing of the atmosphere for use in the numerical models.

III. DETERMINATION OF RADIATIVE FORCING

The first component of the thermal forcing derived in this study was the radiative heating of the atmosphere. In order to obtain the vertical structure of this component, broadband longwave and shortwave radiative transfer routines were employed. In addition, a parameterization scheme for the impact of dust on the radiative heating of the atmosphere was used. This scheme was developed by Ackerman and Cox (1982) from data collected during the Summer MONEX. The horizontal structure of this radiative component was specified according to an idealized concept of the desert-ocean interface. A brief description of the determination of the vertical structure of the radiative heating is provided in this chapter. Also, a description of the horizontal structure specification and the resulting radiative heating profiles are given at the end of the chapter.

1.0 Vertical Structure of the Radiative Heating

The vertical profiles of temperature (T), water vapor mixing ratio (q), carbon dioxide mixing ratio (CO_2), ozone mixing ratio (O_3), and dust mass loading (M) described in Chapter 2 were used as input to broadband longwave and shortwave radiative transfer routines entitled IRADLON and IRADSOL, respectively (a complete description of these routines can be found in Cox et al., 1976). Both routines provide upward and downward irradiances at specified pressure levels. Using these upward and downward irradiances at each level,

the radiative heating rates are computed for the intervening atmospheric layers using the expression

$$\frac{dT}{dt} = -\frac{g}{C_p} \frac{\Delta E_{net}}{\Delta p} \qquad (3.1.1)$$

where ΔE_{net} is the change through the layer of the net irradiance defined as the difference between the downward and upward irradiance at given pressure level, g is the acceleration of gravity, C_p is the specific heat capacity of dry air, and Δp is the thickness of the layer. A brief description of IRADLON and IRADSOL and a derivation of equation 3.1.1 are presented in Appendix A. Also, Appendix A contains a brief description of the parameterization of the impact of the dust which is used in the determination of radiative heating.

The 24 vertical profiles of temperature, water vapor mixing ratio, ozone mixing ratio, and carbon dioxide mixing ratio were used as input to IRADLON and IRADSOL to determine the radiative heating rate for each layer of the atmosphere at each hour of the day for the clear air case. This was accomplished for both the desert profiles where a surface albedo of .30 was specified and the ocean profiles where the surface albedo was set to .07. When the profiles of dust mass loading were included, the dust laden heating rates were obtained. The longwave and shortwave heating rates were then summed to give the net radiative heating rates for each layer. The results for the clear air case and the dust laden case are shown in Figure 3.1a for the desert profiles and in Figure 3.1b for the ocean profiles. The clear air case over the desert and the ocean indicates
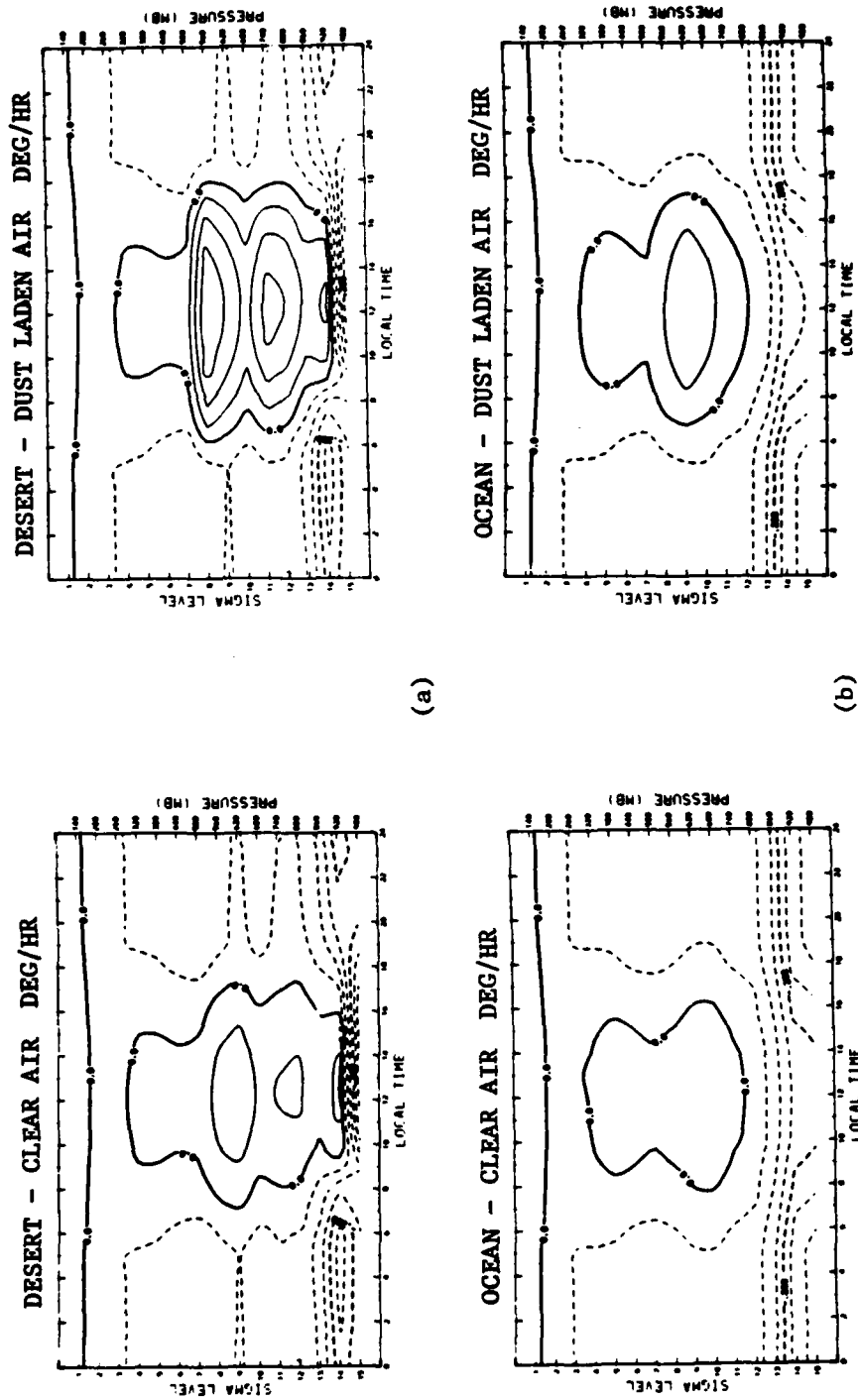
Figure 3.1 Vertical profiles of total (LW + SW) radiative heating as a function of local time for both the clear air case and the dust laden case over the desert (a) and the ocean (b). Contour interval is .05 deg/hr.

a period in the middle of the day when net radiative heating occurs. Over the desert, the heating extends from about 920 mb to 320 mb at local noon. Over the ocean, the depth of the noontime net radiative heating layer is from about 770 mb to 320 mb. The maximum heating occurs at 620 mb over the desert and at 680 mb over the ocean. However, the magnitude of the maximum heating is about twice as large over the desert (.0818 K hr^{-1}) as over the ocean (.0390 K hr^{-1}). This is most probably a result of the higher surface albedo over the desert providing a greater amount of shortwave radiation available for absorption in the upward directed stream. The impact of the dust is to increase the time over which net radiative heating occurs in both the desert and the ocean cases. In the clear desert case, the radiative heating at 620 mb begins at 0800L and lasts until about 1700L. In the dust laden desert case, the net radiative heating at 620 mb begins at 0700L and lasts until 1700L. At 800 mb, the net radiative heating for the clear desert begins at 0900L while for the dust laden desert, it begins at 0700L. Over the ocean, the depth of the layer in which net radiative heating occurs is extended downward from the clear case lower boundary of 770 mb to the dust laden lower boundary of about 800 mb. In both the desert and ocean cases, the magnitude of the net radiative heating is greatly enhanced by the presence of the dust. The maximum net radiative heating over the desert increases from .0818 K hr^{-1} for the clear case to .1941 K hr^{-1} for the dust laden case. Over the ocean the increase is from .0390 K hr^{-1} for the clear case to .0949 K hr^{-1} for the dust laden case. In all cases, except for the middle troposphere in the middle of the day, the atmosphere exhibits net radiative cooling.

The impact of the dust can be further emphasized by examining the vertical profile of the net 24 hour heating for each case. The net 24 hour heating for each layer was obtained by integrating the results in Figure 3.1 in time. These net 24 hour profiles are shown in Figure 3.2. The impact of the dust is to move the curves from the clear air cases to the right in the regions where the dust is present (below about 560 mb). In the desert case, the enhanced shortwave absorption by the dust is sufficient to provide a region between 530 and 830 mb where there is 24 hour net radiative heating. Over the ocean, the magnitude of the radiative cooling is simply reduced.

The pressure-time cross-sections shown in Figure 3.1 were used as the radiative component in the thermal forcing of the numerical models. For the 2-dimensional model, these radiative heating data were provided at hourly increments over the desert and over the ocean at each of the 15 atmospheric layers. In the model, a linear interpolation in time was accomplished in order to obtain heating rates at each time step.

2.0 Horizontal Structure of the Radiative Heating

Once the vertical structure of the radiative heating component of the thermal forcing had been determined, the horizontal structure was specified. The concept used to determine the horizontal structure is one wherein the desert is treated as a rather broad region of intense heating which varies slowly in space but may vary rapidly in time. The ocean, on the other hand, is treated as a very uniform region over which the heating varies slowly in time and not at all in space. Therefore, the horizontal structure of the radiative forcing was determined by a rather broad Gaussian shape which extends from the
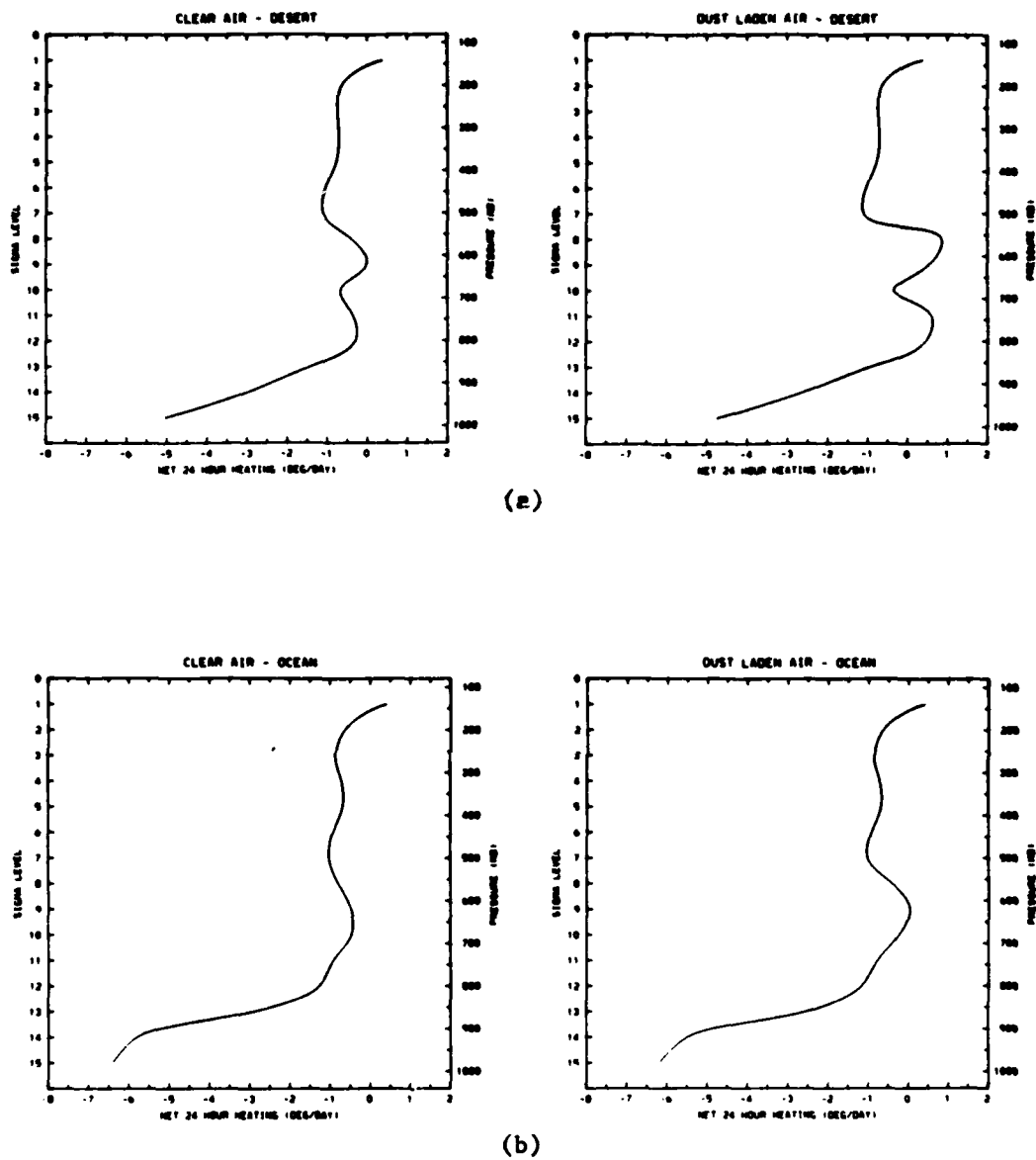
Figure 3.2 Vertical profiles of the net 24 hour total (LW + SW) radiative heating for both the clear air case and the dust laden case over the desert (a) and the ocean (b).

desert profile at the center of the model to within 125 km of the shoreline. The oceanic profile was used from the shoreline to the outer boundary of the model. In functional form, the radiative heating over the desert is given by

$$\dot{Q}_D(r) = \dot{Q}_D(r=0) \exp\left[-(r/1000)^2\right] \qquad 0 < r < 375 \text{ km} \qquad (3.2.1)$$

where $\dot{Q}_D$ is the radiative heating over the desert, and r is the radius from the center in kilometers. Over the ocean, the radiative heating is given by

$$\dot{Q}_O(r) = \dot{Q}_O(r = 500 \text{ km}) \qquad 500 \text{ km} \leq r < 1000 \text{ km} \qquad (3.2.2)$$

where $\dot{Q}_O$ is the radiative heating over the ocean. In the interface region between the desert and the ocean, a linear interpolation was performed from the desert value at 375 km to the ocean value at 500 km. That is, in the interface region the radiative heating is determined from

$$\dot{Q}(r) = \frac{\dot{Q}_O(500 \text{ km}) - \dot{Q}_D(375 \text{ km})}{125 \text{ km}} (r - 375 \text{ km})$$

$$+ \dot{Q}_D (375 \text{ km}) \qquad 375 \text{ km} \leq r \leq 500 \text{ km} \qquad (3.2.3)$$

where all terms have been identified earlier. In the 2-dimensional model, this horizontal structure is applied at each of the vertical layers. An example of this horizontal structure is provided at the end of Chapter 4 where the $\dot{Q}$ terms then represent the total thermal forcing due to both radiative and sensible heating.

IV.   DETERMINATION OF SENSIBLE FORCING

1.0 Magnitude of the Sensible Heating

The   second component of the thermal forcing derived in this study
was   the   sensible   heat   component.   To arrive at the proper sensible
heating, one begins with the surface energy balance equation given by

$$R = H + LE + G + \Delta F \qquad\qquad (4.1.1)$$

where R represents the   net radiation at the surface, H the sensible
heat   transfer,   LE   the   latent   heat   transfer,   G the storage in the
surface,   and ΔF the horizontal transfer within the surface itself.
The   magnitude of   each   of   these   terms is strongly dependent on the
character   of   the   surface.   Some   differences between land and water
surfaces   are   generally   accepted.   Sensible heating of the atmosphere
by   land surfaces usually exceeds that of water surfaces by a factor of
3.   Conversely,   the   latent heat transfer is about three times larger
from   a   water   surface than from a land surface.   While the horizontal
transfer   term   is   small   for   both   land   and   water   surfaces, it is
generally neglected for land surfaces (Sellers, 1965).

In   this   study,   the   desert   was   assumed to be completely dry so
that   the   latent   heat   transfer   term   was   neglected (LE = 0).
Furthermore,   the desert surface was assumed to be incapable of storing
energy   (G = 0)   and   the   surface   horizontal   transfer   term   was
neglected   (ΔF = 0).   The simplified energy balance equation for

the desert was then given by R - H. Therefore, the sensible heat transfer from the desert surface to the atmosphere was parameterized by the net radiation at the surface. This simplified treatment of the surface sensible heat transfer can be further justified by examining the results of an experiment conducted in the Saudi Arabian desert by Smith et al., during June 1981. In the experiment, an instrumented surface station was placed in the desert near Sharouwrah in what is known as the Saudi Arabian Empty Quarter. Sharouwrah is located about 1000 km southeast of Jeddah. The instruments on the surface station consisted of upward and downward pointing shortwave and longwave flux radiometers, air and surface temperature monitors, and soil probes (Smith et al., 1981a). Data from these instruments were used to obtain daily averages of the terms in the surface energy budget equation for a 25 day period from June 2 - June 27 (Julian Day 153-178). The results are shown in Figure 4.1. Since the daily averaged storage is approximately 0.0, the net radiation at the surface must be approximately balanced by sensible heat flux (Smith et al., 1981b).

In the case of a clear atmosphere, a by-product of the radiative heating calculations described in Chapter 3 was the net radiation at the surface. Since both the longwave routine IRADLON and the shortwave routine IRADSOL (assuming a surface albedo value) provided the upward and downward fluxes at the upper and lower boundary of each layer, it was a simple matter to compute the net radiation at the surface. The diurnal variation of the net radiation at the surface is shown in Figure 4.2 for the clear air case over the desert.
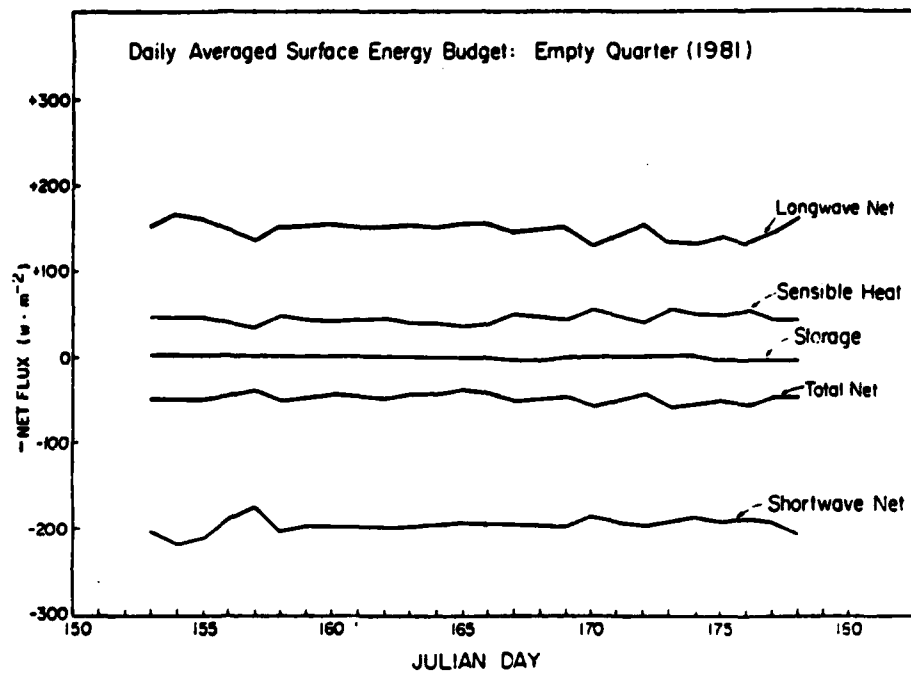
Figure 4.1 Daily averaged surface energy budget for the Saudi
Arabian desert during June 1981 (from Smith et al., 1981a).
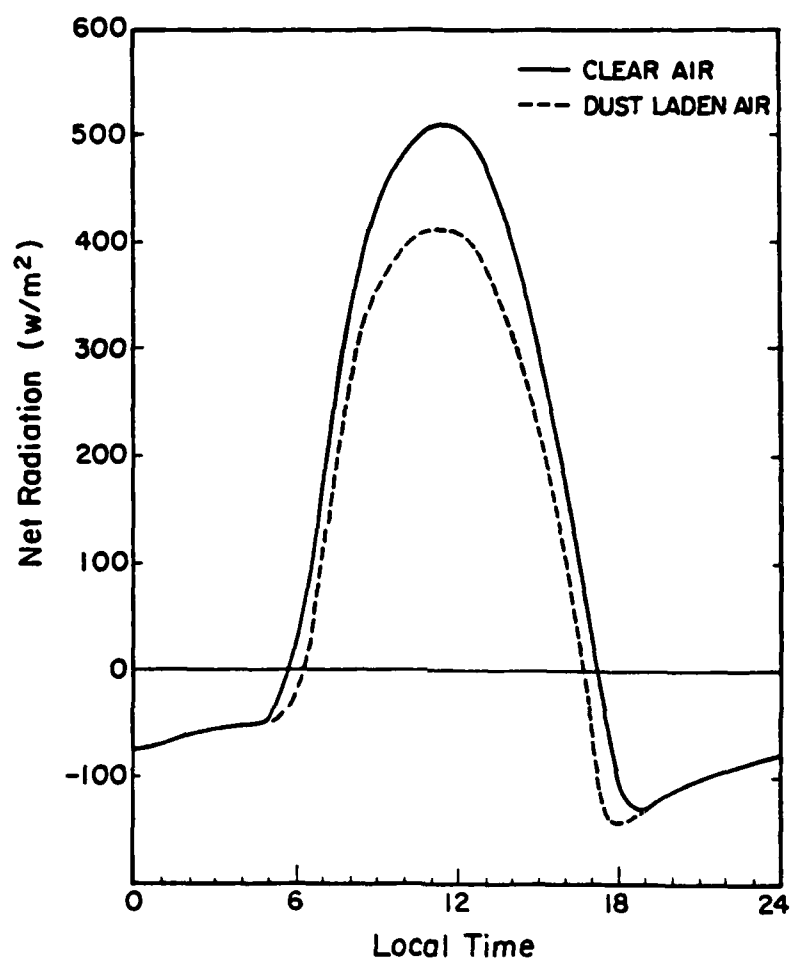
Figure 4.2 Net radiation at the desert surface as a function
of local time for both clear and dust laden atmospheres.

In the dust laden case, it was necessary to try to determine the impact of the dust on the net radiation at the surface. In addition to absorption, the dust could also be important in the scattering of shortwave radiation. In order to understand the scattering impact of the dust, a comparison was made between the total atmospheric transmittance as determined from the dust laden IRADSOL calculations and a monthly average total atmospheric transmittance (Ackerman et al., 1983) determined from the surface station data collected by Smith et al. (1981a). While Smith's data was collected in June and the IRADSOL computations were made for May, the comparison was considered to be a good first approximation to just how serious the scattering impact was. The total atmospheric transmittance was defined by

$$T = \downarrow SW_{sfc} \, / \, \downarrow SW_{top} \qquad\qquad (4.1.2)$$

where the arrows indicate downward fluxes and the subscripts indicate where the flux was measured. The $\downarrow SW_{top}$ flux was computed knowing the latitude, local time, date, and the solar constant. The diurnal variation of the total atmospheric transmittance is shown in Figure 4.3 for both the calculations and the observations. The agreement between the dust laden IRADSOL calculations and the observations is remarkably good during the middle part of the day (0800-1600L). The agreement is even more astounding when it is considered that the IRADSOL dust parameterization (see Appendix A) was based on fractional absorptance within a layer and was not designed to give accurate upward and downward fluxes at a particular level. The maximum error that occurs between 0800 and 1600L is about 2.7%--well
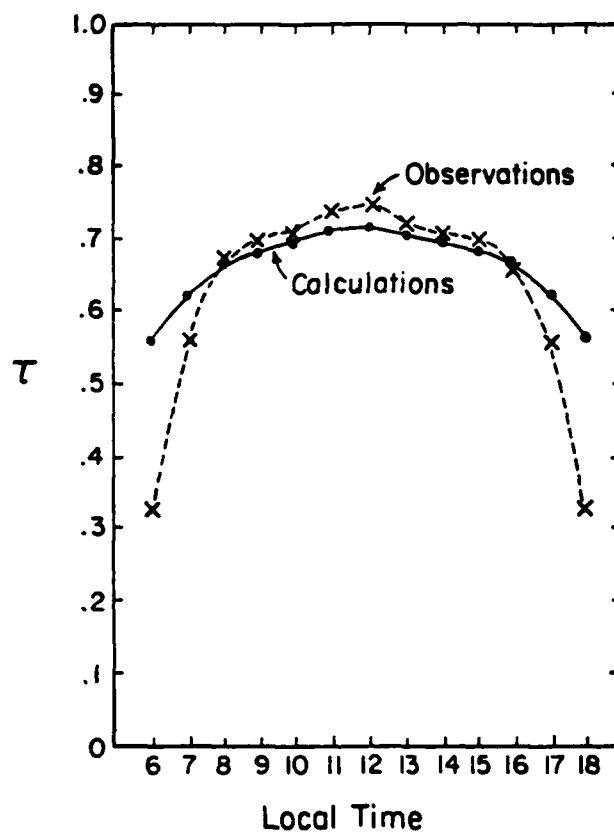
Figure 4.3 Total shortwave atmospheric transmittance as a
function of local time from observations in the Saudi
Arabian desert and calculations from the broadband radiative
transfer routine IRADSOL.

within acceptable range. However, at the extremes, the agreement between the observations and the calculations is not so good. This might have been anticipated since at the larger zenith angles, the scattering by the dust would be enhanced by the longer path lengths. Therefore, lower total atmospheric transmittances should be expected than would be calculated by IRADSOL using simple absorption and Rayleigh scattering. At 0700 and 1700L, the difference is about 12% and at 0600 and 1800L, the difference is about 70%. Therefore, the shortwave net radiation values at the surface from dust laden IRADSOL calculations were used intact between 0800 and 1600L. The shortwave net radiation values at 0600, 0700, 1700, and 1800L were adjusted so as to make the total atmospheric transmittance values agree with the observations. The resulting values of total net radiation (longwave + shortwave) at the surface in the case of dust laden air are shown in Figure 4.2 (dashed curve). The total impact of the dust was to reduce the net radiation at the surface at all hours with the greatest reduction caused by the midday absorption of the incident shortwave radiation.

As for ocean areas, the sensible heat transfer from the ocean surface to the atmosphere is generally considered to be very small. Figure 4.4a (from Sellers, 1965) illustrates the annual variation of the surface energy balance over the Northern Arabian Sea. While there is a slight variation in the sensible heat component, the maximum variation is less than 20 langleys day^{-1} (~ 10 W m^{-2}). This is in good agreement with the magnitude of the sensible heat transfer from the Northern Arabian Sea reported in The Meteorological Atlas of the Indian Ocean Expedition, Volume 1. The results from that
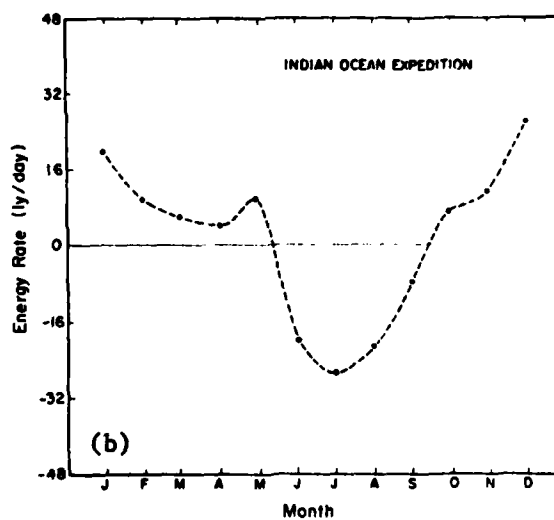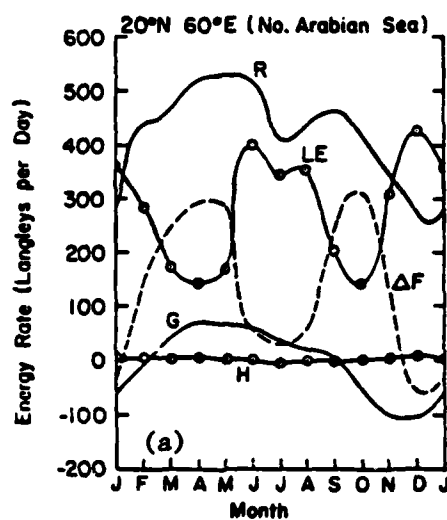
Figure 4.4   Annual variation of the components of the surface energy budget for the Arabian Sea from Sellers, 1965 (a). Annual variation of the sensible heat component for the Arabian Sea from the Indian Ocean Expedition (b).

experiment are plotted in Figure 4.4b. Since these two sources indicate a maximum sensible heat transfer of about 14 W m^{-2}, and since this is very small compared to the radiative cooling of the lower troposphere discussed in Chapter 3, the initial assumption in this study was that there is no sensible heat transfer from the ocean to the atmosphere.

2.0 Vertical Distribution of the Sensible Heating

In order to determine how the sensible heat transferred from the desert surface to the atmosphere should be distributed vertically, a rather classic analysis of the diurnal growth of the mixed layer was undertaken. This analysis follows very closely the analysis first performed by Lilly (1968) for a simplified dry "cloud" layer. While Lilly chose to use the z coordinate in the vertical, this application is better suited to the p coordinate in the vertical.

The analysis begins with a horizontally homogeneous atmosphere characterized by a mixed layer extending from the surface P_o to some level identified by pressure $\bar{P}$. The potential temperature profile in this mixed layer is uniform but varies with time. It is identified as $\theta_o(t)$. Above the mixed layer, the potential temperature increases as p decreases as would be expected for a stable atmosphere. The potential temperature profile above the mixed layer is a function of p but is not a function of t, i.e. $\frac{\partial \theta_U(p)}{\partial p} < 0$. The surface potential temperature is given by $\theta_S(t)$ and it is allowed to vary with time. The atmosphere is subjected to a large scale subsidence field which varies with p and is identified by $\omega(p)$. It is further assumed that the atmosphere above the mixed

layer is non-turbulent. Figure 4.5a illustrates these initial assumptions.

For this case, the thermodynamic equation in the adiabatic mixed layer can be combined with the continuity equation to yield the flux form given by

$$\frac{\partial \theta_o}{\partial t} + \frac{\partial(\theta_o u)}{\partial x} + \frac{\partial(\theta_o v)}{\partial y} + \frac{\partial(\theta_o \omega)}{\partial p} = 0 \ . \qquad (4.2.1)$$

It is assumed the variables given by θ_o, u, v, and ω can be expressed in terms of a mean quantity and a perturbation quantity as

$$\begin{aligned}
\theta_o &= \bar{\theta}_o + \theta_o' \\
u &= \bar{u} + u' \\
v &= \bar{v} + v' \\
\omega &= \bar{\omega} + \omega'
\end{aligned} \qquad (4.2.2)$$

where the mean quantities are horizontally homogeneous. Substituting (4.2.2) into (4.2.1) and averaging horizontally yields the thermodynamic equation for the mixed layer as follows:

$$\frac{\partial \theta_o(t)}{\partial t} = -\frac{\partial}{\partial p} (\overline{\omega' \theta'}) \ . \qquad (4.2.3)$$

The surface sensible heat flux is defined by the bulk aerodynamic relation as
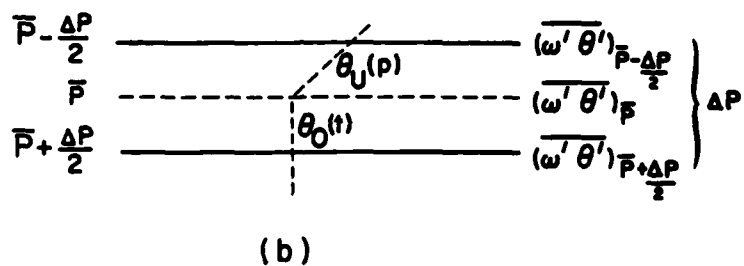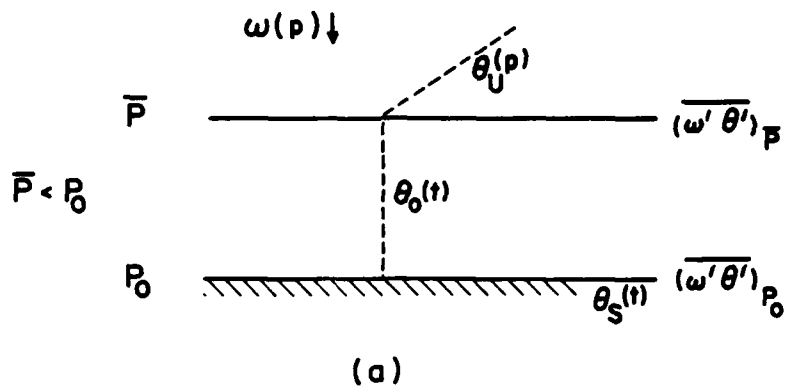
Figure 4.5   Illustration of the initial conditions assumed
in the 1-dimensional mixed layer growth model (a).
Illustration of conditions at the top of the mixed layer (b).

$$(\overline{\omega'\theta'})_{P_o} = C_T' \; V_{P_o} \; (\theta_S(t) - \theta_o(t)) \tag{4.2.4}$$

where C_T' is a modified heat transfer coefficient given by $- \rho_{P_o} \, g \, C_T$, V_{P_o} is the surface wind speed, and $(\theta_S(t) - \theta_o(t))$ is the potential temperature difference between the surface and the mixed layer. Since $\theta_o(t)$ is not a function of p, 4.2.3 implies that $(\overline{\omega'\theta'})$ must be a linear function of p in order that $\dfrac{\partial \theta_o(t)}{\partial t}$ be non-zero. Therefore,

$$(\overline{\omega'\theta'}) = \frac{(\overline{\omega'\theta'})_{\overline{P}} - (\overline{\omega'\theta'})_{P_o}}{\overline{P} - P_o} \; (p - P_o) + (\overline{\omega'\theta'})_{P_o} \; . \tag{4.2.5}$$

Substituting into 4.2.3 obtains

$$\frac{\partial \theta_o(t)}{\partial t} = \frac{(\overline{\omega'\theta'})_{P_o} - (\overline{\omega'\theta'})_{\overline{P}}}{\overline{P} - P_o} \; . \tag{4.2.6}$$

Next, an expression is obtained for the time rate of change of $\overline{P}$ (the pressure at the top of the mixed layer). To do so, consider a layer of thickness Δp centered on $\overline{P}$ as illustrated in Figure 4.5b. Assuming the vertical advection and turbulent heat flux are of comparable magnitudes, the thermodynamic equation for this layer can be written

$$\frac{\partial \theta}{\partial t} + \omega_{\overline{P}} \; \frac{\partial \theta}{\partial p} + \frac{\partial}{\partial p} (\overline{\omega'\theta'}) = 0. \tag{4.2.7}$$

Integrating this equation over the depth of the layer yields

$$\int_{\bar{P} - \frac{\Delta p}{2}}^{\bar{P} + \frac{\Delta p}{2}} \frac{\partial \theta}{\partial t} \, dp = -\int_{\bar{P} - \frac{\Delta p}{2}}^{\bar{P} + \frac{\Delta p}{2}} \omega_{\bar{P}} \frac{\partial \theta}{\partial p} \, dp$$

$$-\int_{\bar{P} - \frac{\Delta p}{2}}^{\bar{P} + \frac{\Delta p}{2}} \frac{\partial}{\partial p} (\overline{\omega' \theta'}) \, dp \qquad (4.2.8)$$

or, since the layer above $\bar{P}$ is non-turbulent

$$\int_{\bar{P} - \frac{\Delta p}{2}}^{\bar{P} + \frac{\Delta p}{2}} \frac{\partial \theta}{\partial t} \, dp = \omega_{\bar{P}} \left[\theta_U(\bar{P}) - \theta_0(t) \right] - (\overline{\omega' \theta'})_{\bar{P} + \frac{\Delta p}{2}} \qquad (4.2.9)$$

where $\theta_U(\bar{P} - \frac{\Delta p}{2})$ has been given by $\theta_U(\bar{P})$.

Using Leibnitz's rule (Hildebrand, 1962), the left hand side can be expressed as

$$\int_{\bar{P} - \frac{\Delta p}{2}}^{\bar{P} + \frac{\Delta p}{2}} \frac{\partial \theta}{\partial t} \, dp = \frac{\partial}{\partial t} \int_{\bar{P} - \frac{\Delta p}{2}}^{\bar{P} + \frac{\Delta p}{2}} \theta \, dp$$

$$- \{\theta(\bar{P} + \frac{\Delta p}{2}) \frac{\partial p}{\partial t})_{\bar{P} + \frac{\Delta p}{2}} - \theta(\bar{P} - \frac{\Delta p}{2}) \frac{\partial p}{\partial t})_{\bar{P} - \frac{\Delta p}{2}}\} . \qquad (4.2.10)$$

In the limit as $\Delta p \to 0$, $\frac{\partial p}{\partial t})_{\bar{P} + \frac{\Delta p}{2}} = \frac{\partial p}{\partial t})_{\bar{P} - \frac{\Delta p}{2}} = \frac{\partial \bar{P}}{\partial t}$ and the first

integral on the right hand side of 4.2.10 is approximately zero. Then

$$\int_{\bar{P} - \frac{\Delta p}{2}}^{\bar{P} + \frac{\Delta p}{2}} \frac{\partial \theta}{\partial t} \, dp = -\frac{\partial \bar{P}}{\partial t} \left[\theta_o(t) - \theta_U(\bar{P}) \right] \qquad (4.2.11)$$

and upon substituting into 4.2.9 above, the expression for $\frac{\partial \bar{P}}{\partial t}$ becomes

$$\left(\frac{\partial \bar{P}}{\partial t} - \omega_{\bar{P}} \right) \left(\theta_U(\bar{P}) - \theta_o(t) \right) + (\overline{\omega'\theta'})_{\bar{P}} = 0 \qquad (4.2.12)$$

where $(\overline{\omega'\theta'})_{\bar{P} + \frac{\Delta p}{2}}$ has been expressed as $(\overline{\omega'\theta'})_{\bar{P}}$.

Equations 4.2.4, 4.2.6, and 4.2.12 involve the unknowns $\bar{P}$, $\theta_o(t)$, $(\overline{\omega'\theta'})_{\bar{P}}$ and $(\overline{\omega'\theta'})_{P_o}$. In order to close the system, a relationship is required for $(\overline{\omega'\theta'})_{\bar{P}}$. At the boundary between the turbulent mixed layer and the non-turbulent atmosphere above, some energy exchange occurs. Energy is transported up from the mixed layer and energy is entrained into the mixed layer from above. The amount of energy carried up from the mixed layer is dependent on how much of the energy supplied at the surface is dissipated before a parcel reaches the top of the mixed layer. Then, the assumption is that the energy entrained from above the mixed layer is equal to the energy transported up from the mixed layer. That is,

$$(\overline{\omega'\theta'})_{\bar{P}} = -C_F (\overline{\omega'\theta'})_{P_o} \qquad (4.2.13)$$

where C_F is the entrainment parameter. Lilly (1968) treated the two extreme cases $C_F = 0.0$ and $C_F = 1.0$ as the minimum and maximum entrainment cases. More recently, Tennekes and Driedonks (1981) and Driedonks (1982) have suggested that for convective entrainment conditions, a value of $C_F = 0.2$ gives results which

best match observations. Therefore, $C_F = 0.2$ has been used in equation 4.2.13 as the closure condition.

In summary, the equations used to model the growth of the mixed layer are given by

$$(\overline{\omega'\theta'})_{P_O} = -\rho_{P_O} g C_T V_{P_O} \left(\theta_S(t) - \theta_O(t) \right)$$

$$(\overline{\omega'\theta'})_{\bar{P}} = -C_F (\overline{\omega'\theta'})_{P_O}$$

(4.2.14)

$$\frac{\partial \theta_O(t)}{\partial t} = \left[\frac{(\overline{\omega'\theta'})_{P_O} - (\overline{\omega'\theta'})_{\bar{P}}}{\bar{P} - P_O} \right]$$

$$\left(\frac{\partial \bar{P}}{\partial t} - \omega_{\bar{P}} \right) \left(\theta_U(\bar{P}) - \theta_O(t) \right) = -(\overline{\omega'\theta'})_{\bar{P}}$$

where C_T, C_F, V_{P_O}, $\theta_S(t)$, $\theta_U(p)$, and $\omega(p)$ are specified. The constants C_T, C_F and V_{P_O} have been given the generally accepted values of $C_T = 0.0015$, $C_F = 0.2$, and $V_{P_O} = 10$ m/s.

The diurnal variation of the surface potential temperature was determined from the Sharouwrah surface station data (Smith et al., 1981a). It was found that two linear functions were sufficient to describe the surface potential temperature trace. The first function described the rise in surface potential temperature from the early morning minimum of 295K to the afternoon maximum of about 330K. The second function described the decrease in surface potential temperature from the afternoon maximum to the early morning minimum. The potential temperature profile above the mixed layer was determined by examining the dropwindsonde data collected during the Pre-Onset

phase of Summer MONEX. An average free atmosphere potential temperature profile was determined for drops made over the Saudi Arabian desert on 12 May 79 and 14 May 79. This mean profile for $\theta_U(p)$ indicated that $\dfrac{\partial \theta_U(p)}{\partial p} = -0.06$ K mb^{-1}. The $\omega(p)$ profile was assumed to increase linearly in p from 0 at the surface to a maximum value of 25 mb day^{-1} at 800 mb. Then, the profile decreased linearly from the 800 mb maximum to 0 at 100 mb. This profile was obtained by examining composite ω profiles reported by McBride and Gray (1978) for background and clear areas in the tropical western Atlantic. While geographically this region is quite distant from Saudi Arabia, in terms of the large scale circulations, both should be within the subsiding branch of the Hadley cell and therefore both should be characterized by large scale subsidence. Using the shape of the McBride and Gray ω profiles for background regions, and using a reasonable value for the maximum subsidence at 800 mb, the $\omega(p)$ profile was determined. With these assumptions, the model was completely described. The numerical steps in using the model are as follows:

1. Compute $(\overline{\omega'\theta'})_{P_o}$ at time $t = t^*$.

2. Compute $(\overline{\omega'\theta'})_{\overline{P}}$ at time $t = t^*$.

3. Use these results to compute $\dfrac{\partial \theta_o(t)}{\partial t}$ and $\dfrac{\partial \overline{P}}{\partial t}$ at time $t = t^*$.

4. Step forward in time to obtain $\theta_o(t' = t^* + \Delta t)$ and $\overline{P}(t' = t^* + \Delta t)$.

5. Return to step 1 with $t = t'$.

In practical terms, the results from the application of this model can be described very generally. As the surface potential temperature increases, the energy supplied to the atmosphere by the surface allows for warming of the mixed layer and growth of the depth of the mixed layer. As the mixed layer grows, a discontinuity in potential temperature is established at the top of the mixed layer. The potential temperature within the mixed layer remains several degrees cooler than the potential temperature in the non-turbulent free atmosphere above the mixed layer. This process continues until such time when the surface potential temperature on its diurnal trace falls below that of the air in the mixed layer. At that time, the energy source at the surface is cut off and the surface actually becomes an energy sink. The result is that the potential temperature of the air in the mixed layer begins to decrease and the depth of the mixed layer begins to decrease. This is taken to be the end of the growth of the mixed layer for that day.

The first experiment conducted with this model allowed an initial (0600L) mixed layer depth of 5 mb ($\bar{P} \approx 995$ mb) with the mixed layer potential temperature equal to the surface potential temperature (295K). The potential temperature profile above the mixed layer was chosen so that when extended downward to the surface, the potential temperature would be 295K. This is illustrated in Figure 4.6. The potential temperature profile at the end of day 1 is also shown in Figure 4.6. In one day, the mixed layer grew through a depth of nearly 250 mb and warmed by about 13K. The growth of the mixed layer as a function of time for this first day is shown in Figure 4.7. In order to perform a second day of integration on the mixed layer growth
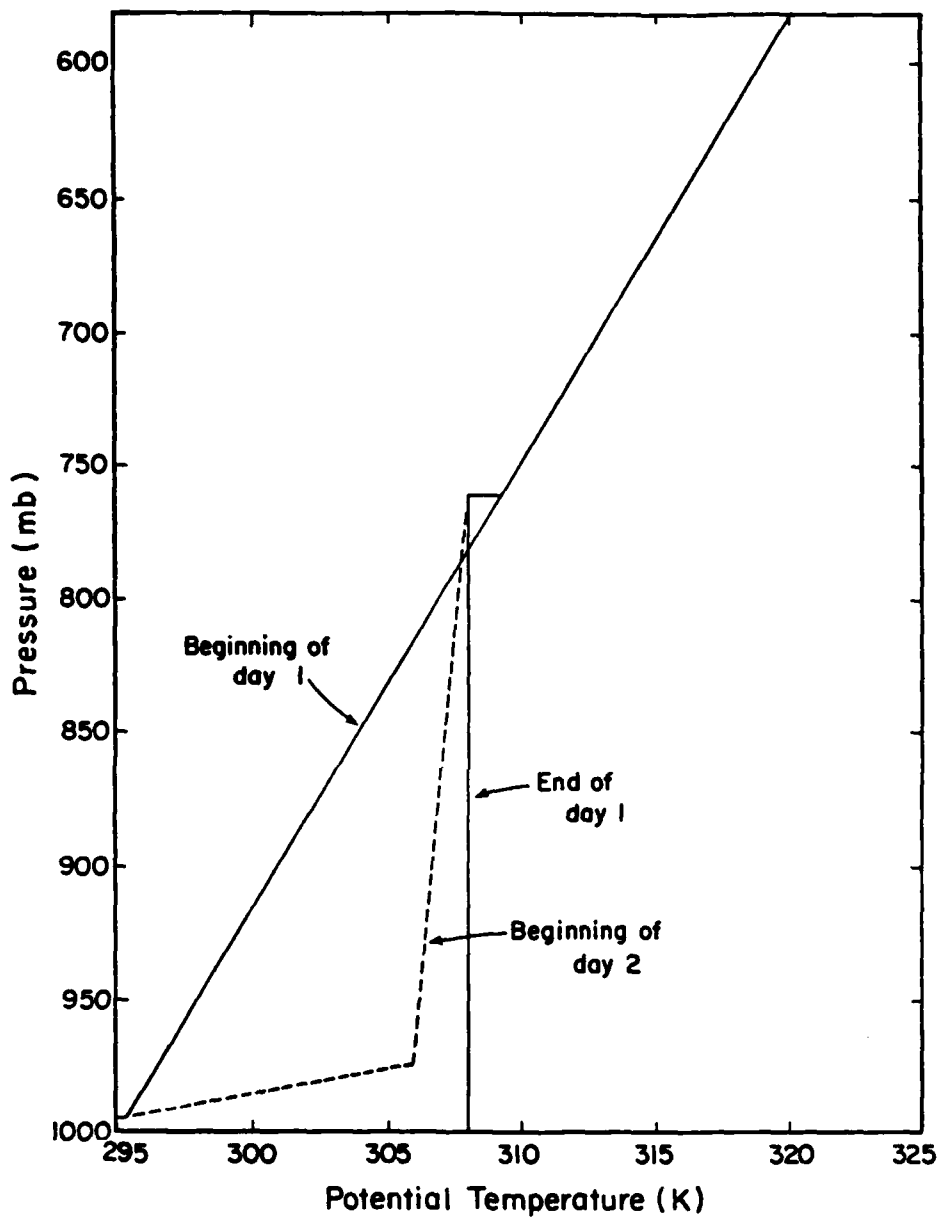
Figure 4.6 Potential temperature profile at the beginning of day 1, end of day 1, and beginning of day 2 for the experiments conducted with the mixed layer growth model.
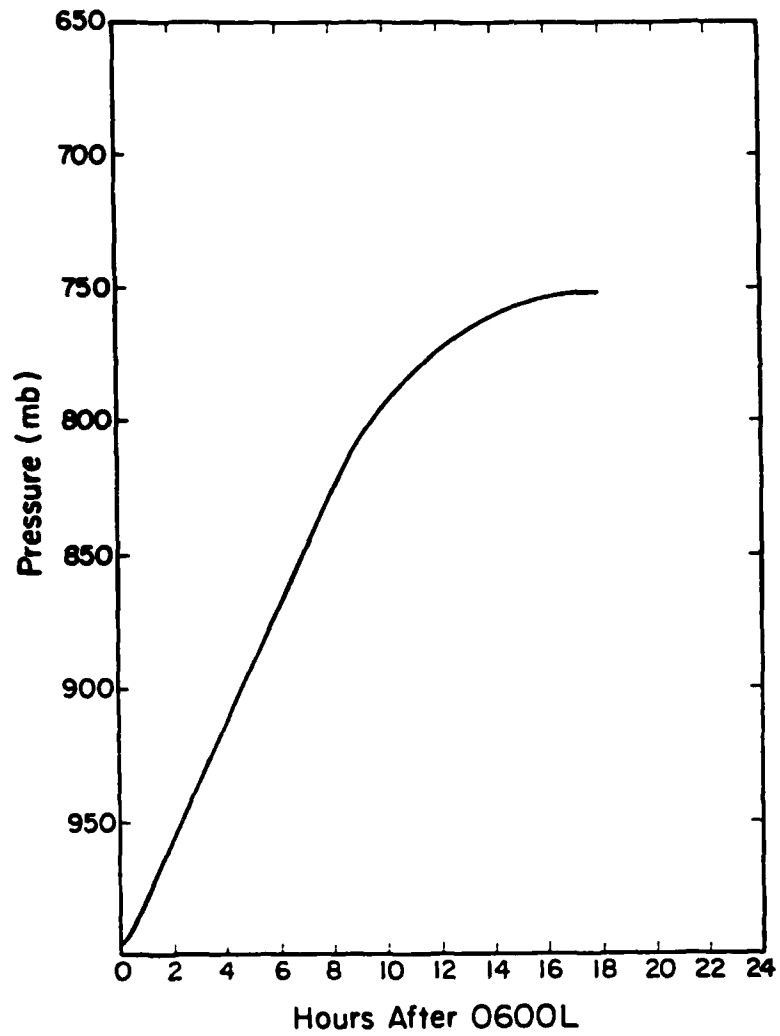
Figure 4.7 Pressure at the top of the mixed layer as a
function of time for day 1 of the mixed layer growth
experiments.

model, it was necessary to make some assumption about the nocturnal evolution of the mixed layer. The most common conceptual model of the mixed layer is that a shallow layer with very high stability forms near the surface. Above this surface layer, the remnant mixed layer from the previous day becomes slightly stable ($\frac{\partial \theta}{\partial p} < 0$) rather than neutral ($\frac{\partial \theta}{\partial p} = 0$). Such an evolution from the neutral case at the end of day 1 to the common early morning case at the beginning of day 2 is illustrated by the dashed line in Figure 4.6. Four experiments were performed based on this type of nocturnal adjustment in the mixed layer.

In two of the experiments, the depth of the strongly stable layer near the surface was fixed at 25 mb, and in the remaining two experiments, the depth of the strongly stable layer was 50 mb. For each stable layer depth, two diffferent θ profiles were allowed in the remnant mixed layer between the top of the strongly stable surface layer and the top of the mixed layer at the end of the previous day's growth. In both cases, the 0600L potential temperature at the top of the stable layer was fixed at a value given by the 0600L potential temperature at the surface plus a fraction of the difference between the potential temperature of the mixed layer at the end of the previous day's growth and the 0600L potential temperature at the surface. That is,

$$\theta_{SL} = \theta_S + f (\theta_{\bar{p}} - \theta_S) \tag{4.2.15}$$

where θ_{SL} is the potential temperature at the top of the stable layer, θ_S is the surface potential temperature, $\theta_{\bar{p}}$ is the potential temperature of the mixed layer at the end of the previous day's growth, and f is the variable fraction. The two cases

for the potential temperature profile in the remnant mixed layer were determined by allowing $f = 0.85$ and $f = 0.75$. The 0600L surface potential temperature was assumed to be 295K at the beginning of each day in accordance with the observations from the Sharouwrah surface station. The four cases for the potential temperature at the top of the stable layer were then determined by the following relations:

$$\text{Case 1} \quad \theta \text{ (975 mb)} = 295K + 0.85 \, (\theta_{\overline{p}} - 295)$$

$$\text{Case 2} \quad \theta \text{ (975 mb)} = 295K + 0.75 \, (\theta_{\overline{p}} - 295)$$

$$(4.2.16)$$

$$\text{Case 3} \quad \theta \text{ (950 mb)} = 295K + 0.85 \, (\theta_{\overline{p}} - 295)$$

$$\text{Case 4} \quad \theta \text{ (950 mb)} = 295K + 0.75 \, (\theta_{\overline{p}} - 295) \, .$$

The four cases for the initiation of the day 2 growth are shown in Figure 4.8. It is apparent that the surface layer is more stable in the shallow stable layer cases (cases 1, 2) than in the deeper stable layer cases (cases 3, 4). Likewise, the remnant mixed layer is more stable in the cases where $f = 0.75$ (cases 2, 4) than where $f = 0.85$ (cases 1, 3).

For each case, the experiment was conducted until the mixed layer growth for a given day exceeded the previous day's growth by less than 5 mb. This was assumed to be the steady state. In all cases, the mixed layer growth on day 7 was 5 mb or less. The initial potential temperature profiles on day 7 for each case are shown in Figure 4.9. In all cases, the maximum depth through which the mixed layer grew was between 300 and 350 mb. Also shown in Figure 4.9 is an average potential temperature profile from three dropwindsonde observations

51
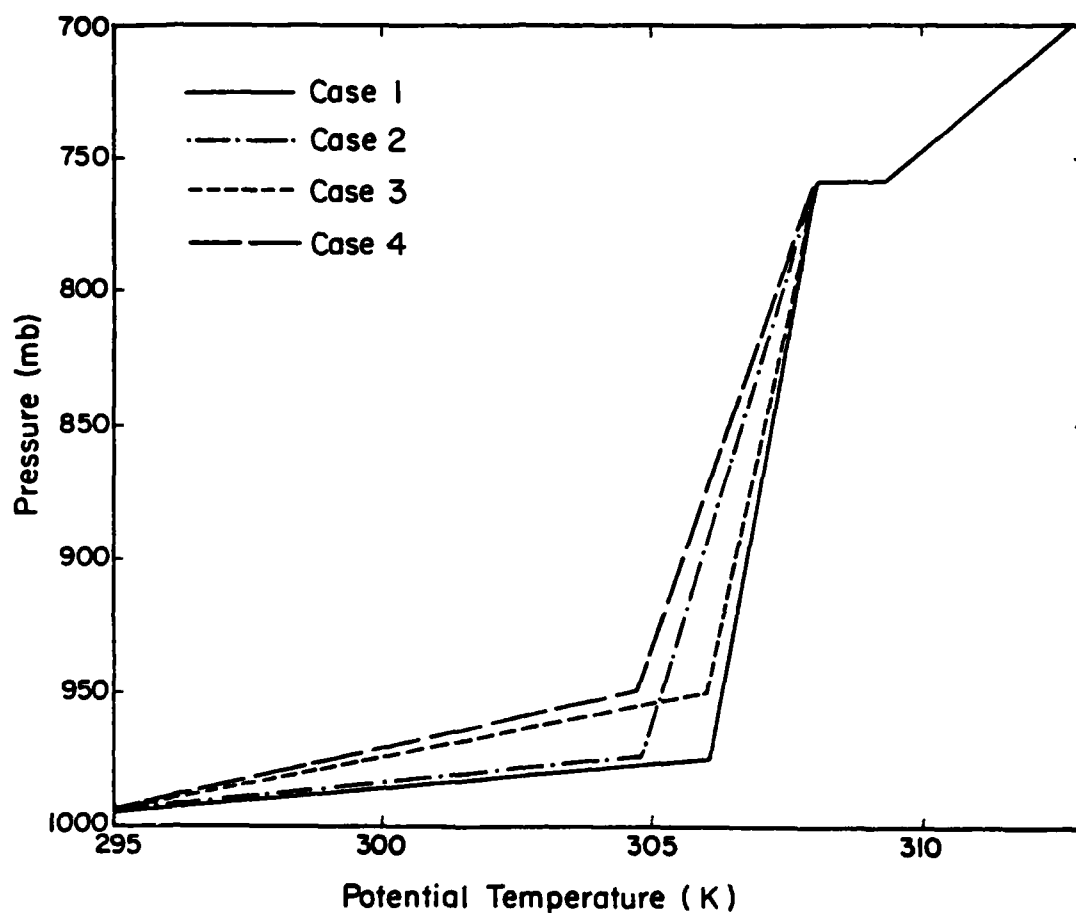
Figure 4.8 Assumed potential temperature profiles at the
beginning of day 2 for the cases 1-4 (see text) mixed layer
growth experiments.
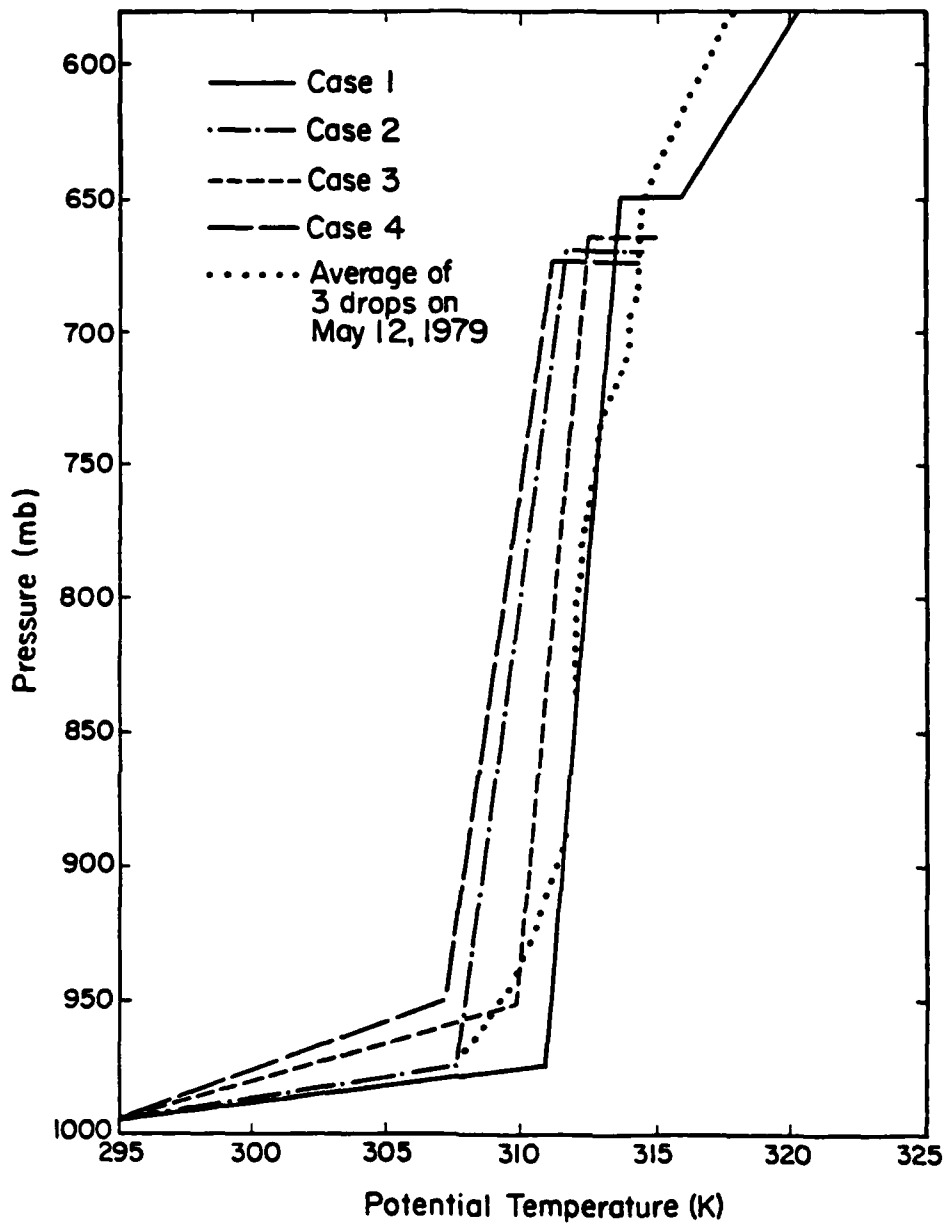
Figure 4.9 Resulting potential temperature profiles at
the beginning of day 7 for the cases 1-4 (see text)
mixed layer growth experiments and an average of three
dropwindsonde profiles on May 12, 1979.

made on 12 May 79. These drops were made from an early morning flight of the Convair 990 over the desert. It is apparent that the case 1 profile best fits the data from the dropwindsondes. Since the steady state case 1 early morning profile is in good agreement with the available observations, it is reasonable to assume that the diurnal growth of the mixed layer can be approximated by the results of the case 1 experiment.

The diurnal growth of the mixed layer for case 1 is shown in Figure 4.10 for days 1, 4 and 7 of the experiment. Table 4.1 gives the pressure at the top of the mixed layer and the potential temperature in the mixed layer at the end of each day of the case 1 experiment. The growth on day 1 is very large compared to the growth on the other days. The reason for the decrease in growth is that beginning with day 2, a very stable layer exists near the surface. Much of the energy available from the surface is required to overcome the stability of this surface layer and therefore, less energy is available to force the mixed layer top upward. On successive days, as the temperature of the mixed layer increases, the stability of the surface layer increases because the depth of the surface layer is fixed at 25 mb.

The case 1 day 7 mixed layer growth profile has been used to distribute the sensible heat vertically. The vertical distribution of the sensible heat is based on knowing the amount of energy available from the surface at a particular time, and the depth of the mixed layer at that time. The available energy was determined by the net radiation at the surface as explained earlier. The mixed layer depth was available from the results of this 1-dimensional model. Since the
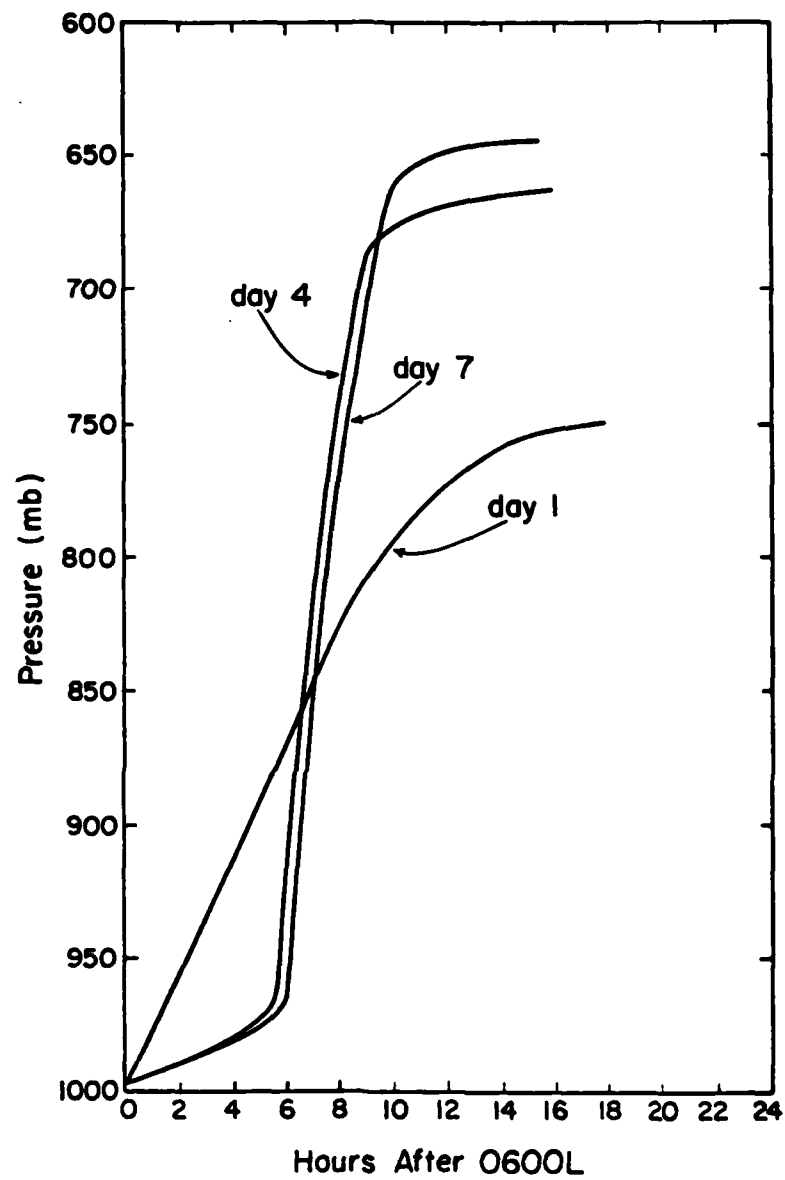
Figure 4.10 Pressure at the top of the mixed layer as a function of time for days 1, 4, and 7 of the case 1 (see text) mixed layer growth experiments.

TABLE 4.1

Pressure at the top of the mixed layer and the potential temperature
within the mixed layer at the end of each day for the case 1
experiment (see text)

	$\theta_o(K)$	$\bar{P}$ (mb)
DAY 1	308.05	760
DAY 2	310.67	710
DAY 3	311.97	685
DAY 4	312.72	670
DAY 5	313.17	660
DAY 6	313.44	655
DAY 7	313.61	651

2-dimensional model is designed with discreet layers in the vertical, the distribution scheme applies the sensible heat in discreet layers. The available sensible energy is distributed evenly through all discreet layers through which the mixed layer has grown at a particular time. For example, if the available energy is to be distributed through two complete model layers and half of a third layer, then the amount of energy applied to the third layer is half as much as is applied to the two complete layers. Exactly the same amount of energy is applied to each of the two complete layers through which the mixed layer has grown. This distribution is accomplished at each time step in the 2-dimensional numerical model from 0600L until the net radiation at the surface becomes negative. When the net radiation at the surface is negative, then the sensible heat is removed only from the lowest layer of the atmosphere. This process simulates the establishment of the strongly stable surface layer.

3.0 Horizontal Structure of the Sensible Heating

The horizontal structure of the sensible heating component is the same as that for the radiative heating component. Once the radiative and sensible components are determined at a particular time for each of the 15 atmospheric layers, the two components are summed to yield a total thermal forcing for each layer at that time. This is done for both the desert and the ocean cases. Then, the horizontal structure determination described in Section 2 of Chapter 3 is applied. The forcing terms $\dot{Q}$ then represent the sum of the radiative and sensible heating components and therefore are the total thermal forcing.

An example of this horizontal structure of the total thermal forcing is provided in Figure 4.11 for the clear air case at 1200L. It should be noted that in the layers away from the surface, the contrast between the desert and the ocean is very slight. Most of the horizontal gradients between the desert and the ocean regions occur in the lower layers.
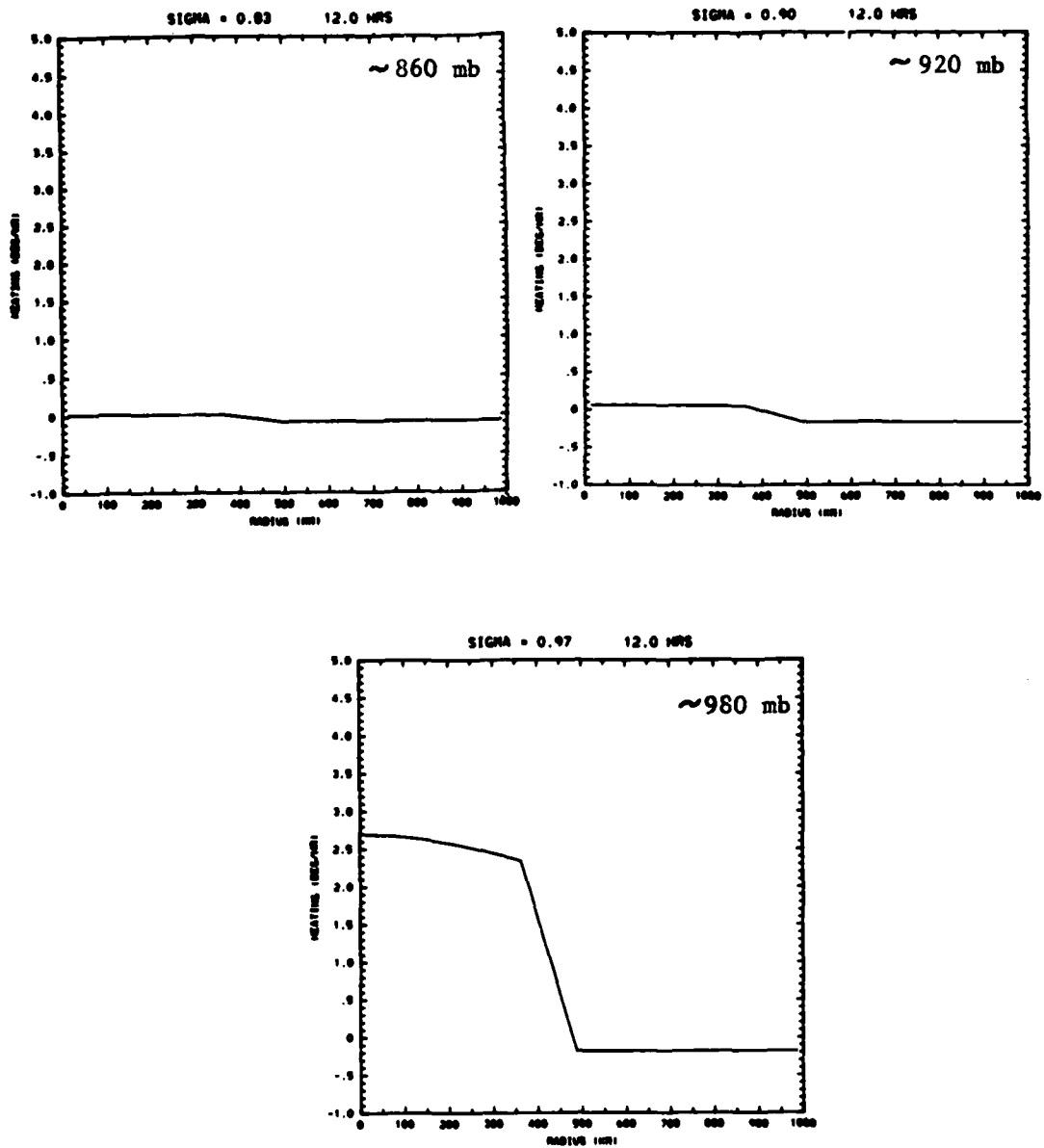
Figure 4.11 Total (radiative + sensible) heating as a function of radius in the model domain for three different levels at 1200L.

V. 2-DIMENSIONAL PRIMITIVE EQUATION MODEL

The initial experiments to determine the atmospheric circulation which would be induced by the contrast between atmospheric conditions over the Saudi Arabian desert and the adjacent Arabian Sea were undertaken with the use of a 2-dimensional, axisymmetric, primitive equation numerical model. The model was originally developed to study tropical cyclones (Hack and Schubert, 1976). However, with some minor modifications, the model was readily adapted to the study of the "heat low" circulation. A brief description of the model design and some results of the numerical experiments are given in this chapter.

1.0 The Numerical Model

The equations used in the numerical experiments described in this chapter consist of the flux form of the primitive equations for a dry atmosphere written in axisymmetric horizontal cylindrical (r, λ) coordinates and the vertical sigma (σ) coordinate. A brief description of the model equations is presented in this section. A more detailed description can be found in Appendix B, and a complete description is provided in Hack and Schubert, 1976.

The vertical σ coordinate is defined as

$$\sigma = \frac{P - P_T}{P_S - P_T} = \frac{P - P_T}{\pi} \qquad (5.1.1)$$

where P_T is the fixed pressure at the top of the atmosphere and

P_S is the surface pressure which is allowed to vary in both space and time. The sigma coordinate is a generalized pressure coordinate in which the top boundary of the model atmosphere ($P = P_T$) and the bottom boundary of the model atmosphere ($P = P_S$) always have the respective σ values 0 and 1. Therefore, the top and bottom boundary conditions, namely that air parcels do not cross the boundaries, can be written as

$$\frac{d\sigma}{dt} = \dot{\sigma} = 0 \quad \text{at} \quad \sigma = 0, 1. \tag{5.1.2}$$

The complete set of prognostic and diagnostic equations which comprise the numerical model can be written in flux form as follows:

(Radial Momentum)
$$\frac{\partial(\pi r u)}{\partial t} = -\frac{\partial(\pi r u \dot{\sigma})}{\partial \sigma} - \frac{\partial}{\partial r}\left(\pi r u^2\right) + \pi r v \left(f + \frac{v}{r}\right)$$
$$- \pi r \left(\frac{\partial \phi}{\partial r} + \sigma\alpha \frac{\partial \pi}{\partial r}\right) + \pi r F_u \tag{5.1.3}$$

(Tangential Momentum)
$$\frac{\partial(\pi r v)}{\partial t} = -\frac{\partial(\pi r v \dot{\sigma})}{\partial \sigma} - \frac{\partial}{\partial r}\left(\pi r u v\right)$$
$$- \pi r u \left(f + \frac{v}{r}\right) + \pi r F_v \tag{5.1.4}$$

(Hydrostatic)
$$\frac{\partial \phi}{\partial \sigma} = -\pi\alpha \tag{5.1.5}$$

(Surface Pressure Tendency)
$$\frac{\partial(\pi r)}{\partial t} = -\frac{\partial}{\partial r}\int_0^1 (\pi r u) \, d\sigma' \tag{5.1.6}$$

(Modified Continuity) $\quad \pi r \dot{\sigma} = - \sigma \dfrac{\partial(\pi r)}{\partial t} - \dfrac{\partial}{\partial r} \displaystyle\int_0^\sigma (\pi r u)\, d\sigma'$ (5.1.7)

(Thermodynamic) $\quad \dfrac{\partial(\pi r T)}{\partial t} = - \dfrac{\partial(\pi r T u)}{\partial r} - (P/P_0)^{R/C_p} \dfrac{\partial}{\partial \sigma} (\pi r \dot{\sigma} \theta)$

$$+ \dfrac{\pi r \alpha \sigma}{C_p} \left(\dfrac{\partial}{\partial t} + u \dfrac{\partial}{\partial r} \right) \pi + \dfrac{\pi r}{C_p} \dot{Q} + \pi r F_T \qquad (5.1.8)$$

(Poissons's Equation) $\quad \theta = T \left(P_0/P \right)^{R/C_p}$ (5.1.9)

(Equation of State) $\quad p\alpha = RT$ (5.1.10)

(Definition of Sigma) $\quad \sigma = \dfrac{P - P_T}{P_S - P_T} = \dfrac{P - P_T}{\pi}$ (5.1.11)

In equations 5.1.3 - 5.1.11, u is the radial component of wind, v the tangential component of wind, $\dot{\sigma}$ the time rate of change of the vertical coordinate, ϕ the geopotential, T the temperature, θ the potential temperature, α the specific volume, f the Coriolis parameter (constant on an f plane), p the pressure, P_0 the reference pressure (1000 mb), R the gas constant for dry air, C_p the specific heat capacity for dry air, $\dot{Q}$ the energy source per unit mass per unit time, F_u, F_v, and F_T the momentum and thermodynamic sources/sinks and π as in 5.1.1. The continuous form of these equations is replaced by finite difference forms in the vertical and horizontal. Knowing initial states for u, v, T, and π at each discreet level in the vertical and at each horizontal increment, this system of equations is used to predict the u, v, T,

and π fields at some future time. The initial time step in the model is accomplished with the Matsuno (1966b) simulated backward difference method. Thereafter, the leapfrog scheme with an Asselin (1972) filter is used with a 20 second time step.

2.0 Physical Description of the Model

In this application of the numerical model, the atmosphere was divided into 15 layers from the surface ($\sim$ 1010 mb) to the top of the troposphere ($\sim$ 110 mb). Table 5.1 gives the approximate pressure and corresponding σ value for the center of each layer. Also given is the approximate height of the center of each layer above the surface. As for the radial distribution, the model was designed with 40 increments in the horizontal. Geographically, the distance from the center of the Saudi Arabian desert to the shore of the Arabian Sea is about 500 km. In order for this to account for half the radial distance of the model, the horizontal increment was set to 25 kilometers. The horizontal specification of the model then represents desert conditions from the center of the model out to 500 km and oceanic conditions from 500 km to the outer boundary at 1000 km.

3.0 Specification of the Forcing Terms

In the formulation of this model, there are no momentum sources specified. The forcing terms given by F_u and F_v in equations 5.1.3 and 5.1.4 represent momentum sinks. These terms represent the diffusion of momentum through sub-grid scale eddy processes in both the horizontal and vertical directions. In this model, these processes are represented by terms which are written

TABLE 5.1

Value of σ, pressure, and approximate height of the midpoint of each of the 15 vertical layers in the 2-dimensional model.

Layer Number	σ	Pressure (mb)	Height (km)
1	.033	140	14.80
2	.100	200	12.50
3	.167	260	10.70
4	.233	320	9.30
5	.300	380	8.00
6	.367	440	6.90
7	.433	500	5.90
8	.500	560	5.00
9	.567	620	4.20
10	.633	680	3.40
11	.700	740	2.70
12	.767	800	2.10
13	.833	860	1.40
14	.900	920	0.80
15	.967	980	0.27

$$F_u = \frac{1}{\pi r} \left[\frac{\partial}{\partial r} \left(\pi r K_H \frac{\partial u}{\partial r} \right) - \frac{\pi u K_H}{r} \right] + \frac{g}{\pi} \frac{\partial}{\partial \sigma} \tau u \qquad (5.3.1)$$

$$F_v = \frac{1}{\pi r} \left[\frac{\partial}{\partial r} \left(\pi r K_H \frac{\partial v}{\partial r} \right) - \frac{\pi v K_H}{r} \right] + \frac{g}{\pi} \frac{\partial}{\partial \sigma} \tau v \qquad (5.3.2)$$

where the first term in each expression represents the horizontal diffusion process and the second term represents the vertical diffusion process. The horizontal eddy diffusion coefficient K_H is defined in terms of a linear and a nonlinear part as

$$K_H = K_{H_o} + \ell_H^2 |D| \qquad (5.3.3)$$

where the horizontal mixing length ℓ_H is given as $.2\Delta r$ and $|D|$ is the magnitude of the total deformation field defined as

$$|D| = r \left[\left(\frac{\partial}{\partial r} \left(\frac{u}{r} \right) \right)^2 + \left(\frac{\partial}{\partial r} \left(\frac{v}{r} \right) \right)^2 \right]^{1/2} \quad . \qquad (5.3.4)$$

In the numerical model, the linear portion of the eddy diffusion coefficient, K_{H_o}, was given a numerical value depending on where the diffusion was being applied. Within the mixed layer over the desert region of the model domain, K_{H_o} was given the value 50000 $m^2 s^{-1}$. Outside this desert mixed layer, a value of 5000 $m^2 s^{-1}$ was used on the assumption that the dispersion processes are much more important within the mixed layer than elsewhere in the model domain. The analysis technique which was used to determine a reasonable value for K_{H_o} within the mixed layer is presented in Appendix C. It should be

pointed out that during the course of conducting the experiments with this model, the horizontal dispersion terms in the momentum equations were found to be quite small. Therefore, it was assumed that the horizontal dispersion process was not an important process. Sensitivity analyses were performed in which K_{H_o} was varied from 5000 m^2s^{-1} to 70000 m^2s^{-1} with nearly no perceptible change in the results.

The second term in equations 5.3.1 and 5.3.2 represents the vertical diffusion of momentum by sub-grid scale convective eddies. The vertical stress terms are defined by

$$\tau_u = \frac{-K_v g \rho^2}{\pi} \frac{\partial u}{\partial \sigma} \qquad (5.3.5)$$

and

$$\tau_v = \frac{-K_v g \rho^2}{\pi} \frac{\partial v}{\partial \sigma} \qquad (5.3.6)$$

where the vertical eddy diffusion coefficient is defined by

$$K_v = \ell_v^2 \frac{g\rho}{\pi} \left|\frac{\partial \vec{v}}{\partial \sigma}\right| . \qquad (5.3.7)$$

In these expressions, ρ is the atmospheric density, $\vec{V}$ is the 2-dimensional vector velocity, and ℓ_v is the vertical mixing length. A brief review of the literature (Busch et al., 1976; Kurihara and Tuleya, 1974; Hack and Schubert, 1980) indicated values between 400 m^2 and about 250000 m^2 have been used for ℓ_v^2. Two values of ℓ_v^2 have been chosen depending on whether or not the stress is being

calculated within the well mixed layer over the desert or outside this well mixed layer in the free atmosphere. Within the well mixed layer, ℓ_v^2 has been given the value 25000 m² and outside this layer, a value of 2500 m² was assigned to ℓ_v^2. The assumption, as in the case of K_{H_o} for horizontal dispersion above, is that within the mixed layer over the desert, turbulent convective processes are significantly more important than elsewhere in the model domain. As in the case of K_{H_o} above, sensitivity tests using a range of ℓ_v^2 from 2500 m² to about 50000 m² indicated the results were relatively insensitive to this parameter.

In the thermodynamic equation (5.1.8), the term identified by F_T represents the horizontal diffusion of heat. It is given in this model by

$$F_T = \frac{1}{\pi r} \frac{\partial}{\partial r} \left[\pi r K_H \frac{\partial T}{\partial r} \right] \tag{5.3.8}$$

where K_H is given by 5.3.3. The same horizontal eddy diffusion coefficient is used in the case of thermodynamic energy as in the case of momentum. In the vertical, a dry convective adjustment process is invoked if the potential temperature profile becomes unstable. That is, when $\frac{\partial \theta}{\partial \sigma} > 0$, then it is assumed that the atmosphere will adjust through dry convection and that an adiabatic lapse rate will be established.

The final forcing term for the model is the term identified by $\dot{Q}$ in the thermodynamic equation. It is through this term that the thermal forcing is accomplished. There are two components which comprise the thermal forcing. The first component is the radiative

heating of the atmosphere and the second component is the sensible heating of the atmosphere. The specification of these two components is covered in great detail in Chapters 3 and 4 and will not be repeated here.

4.0 Results of Numerical Experiments

Several experiments were conducted using the 2-dimensional axisymmetric, primitive equation model described above. Each experiment consisted of altering the thermal forcing for the model. All experiments were run for a period of 96 hours from the same initial state. The initial state was one of rest with a uniform surface pressure of 1010 mb over the whole domain. The initial temperature field was uniform in the horizontal and given by the temperature field over the ocean in the vertical. The initial state for each experiment was one with no horizontal gradients except in the thermal forcing. The results of the experiments are presented and discussed in this section.

4.1 Radiative Forcing Only vs. Radiative + Desert Sensible Forcing

In order to examine the relative importance of the radiative and sensible components of the thermal forcing, a comparison was made between the circulation induced by a thermal forcing field which consisted only of a radiative component and the circulation induced by a thermal forcing field which included a radiative and sensible component. In the first case, only the clear air radiative heating profiles shown in Figure 3.1 were used to force the model. In the second case, these same clear air radiative heating profiles were combined with the sensible heating component over the desert to obtain

the total thermal forcing for the model. The horizontal and vertical distributions of the desert sensible heating are discussed in Chapter 4. A comparison of the induced circulations for these two cases shows the dominant component of the thermal forcing is the surface sensible heating. The radiative component is a small perturbation to the sensible component.

Shown in Figure 5.1 is the surface pressure trace at a radius of 37.5 km from the center of the model domain for the case of radiative forcing only and for the case of radiative + sensible forcing. In both cases, the surface pressure shows a gradual decrease through about 48 hours. Thereafter, the "heat low" pressure begins a steady diurnal oscillation. In the case of radiative forcing only, the pressure oscillates between about 1009.50 mb at the diurnal maximum near 2200L and about 1009.00 at the diurnal minimum near 1300L. The daily average surface pressure in this case is about 1009.25 mb. For the case of radiative + sensible forcing, the induced surface pressure trace at 37.5 km oscillates between the diurnal maximum of about 1007.10 mb near 0700L and the diurnal minimum of about 1004.20 mb near 1600L. The diurnal mean surface pressure is about 1005.90 mb. It is interesting to note that the times of the minimum surface pressure in the "heat low" in both these cases correspond well with the times of maximum heating. The radiative component of heating (Figure 3.1) peaks between 1200 and 1300L and the diurnal minimum in surface pressure occurs near 1300L. When the sensible component is added, the vertical distribution of the sensible heat is such that the surface flux is distributed through the maximum depth near 1600L -- precisely when the surface pressure minimizes.
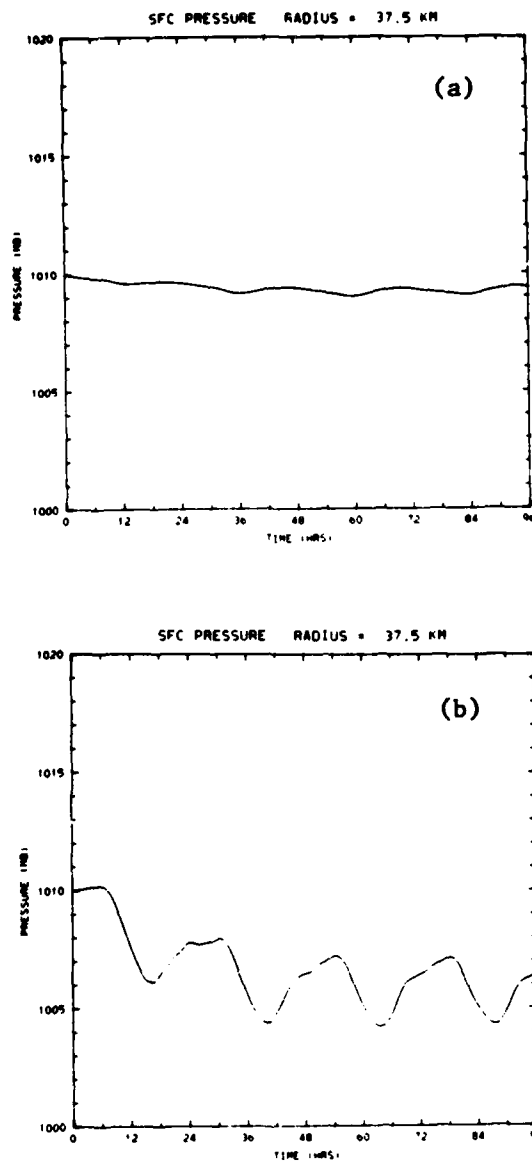
Figure 5.1   Surface pressure trace at a radius of 37.5 km for the case of radiative forcing only (a) and radiative + desert sensible forcing (b) in clear air.

Shown in Figures 5.2 and 5.3 are the radial distribution of surface pressure (a), and the vertical cross-sections of the tangential (b) and radial (c) wind components and vertical motion (d) for both cases. Figure 5.2 contains the results from the case with radiative forcing only and in Figure 5.3 are the results from the radiative + sensible forcing case. These results are the instantaneous fields at the time of minimum "heat low" surface pressure -- 61 hours (1300L) for the radiative forcing only case and 64 hours (1600L) for the radiative + sensible forcing case. The left half of each diagram (0 to 500 km) represents the region modelled by the desert characteristics and the right half (500 to 1000 km) represents the oceanic region. In both cases, a surface low pressure center is apparent near the center of the domain where the thermal forcing is a maximum. Both cases are characterized by a low level cyclonic circulation with radial inflow from the ocean to the desert. In the middle troposphere, both cases exhibit an anticyclonic circulation with radial outflow from the desert to the ocean. Both cases show a deep layer of upward vertical motion over the desert with compensating subsidence over the ocean.

Figures 5.1, 5.2, and 5.3 clearly show the importance of the sensible heating component in the development of the surface "heat low". By including the effects of the sensible heat off the desert surface, a much more intense "heat low" was produced than in the experiment with radiative forcing only. The average daily surface pressure is about 3.35 mb lower with the inclusion of the desert sensible heat. In addition, the surface pressure gradient at the time of minimum surface pressure over the desert between the "heat low" and

SFC PRESSURE 61.0 HRS

(a)

TANGENTIAL WIND 61.0 HRS (M/S)

(b)

RADIAL WIND 61.0 HRS (M/S)

(c)

OMEGA 61.0 HRS (MB/DAY)

(d)

CONTOUR INTERVAL
(b) - 1.0 M/s
(c) - 0.5 M/s
(d) - 50 MB/DAY
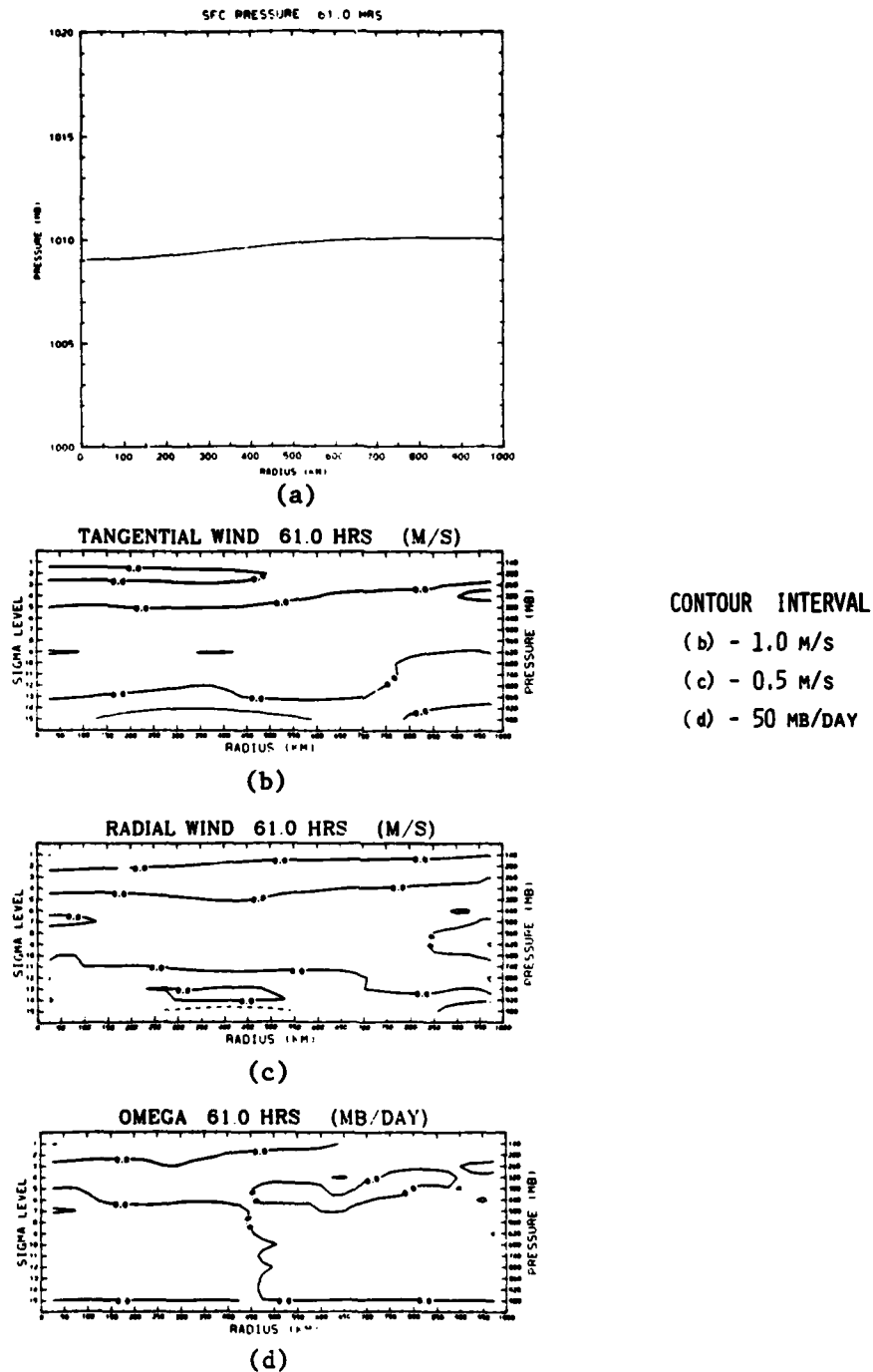
Figure 5.2 Radial distribution of surface pressure (a) and
vertical cross-sections of tangential wind (b), radial wind (c),
and vertical motion (d) at 61 hours for the case of radiative
forcing only in clear air.

SFC PRESSURE 64.0 HRS

(a)

TANGENTIAL WIND 64.0 HRS (M/S)

(b)

CONTOUR INTERVAL

(b) - 1.0 M/s

(c) - 0.5 M/s

(d) - 50 MB/DAY

RADIAL WIND 64.0 HRS (M/S)

(c)

OMEGA 64 0 HRS (MB/DAY)

(d)
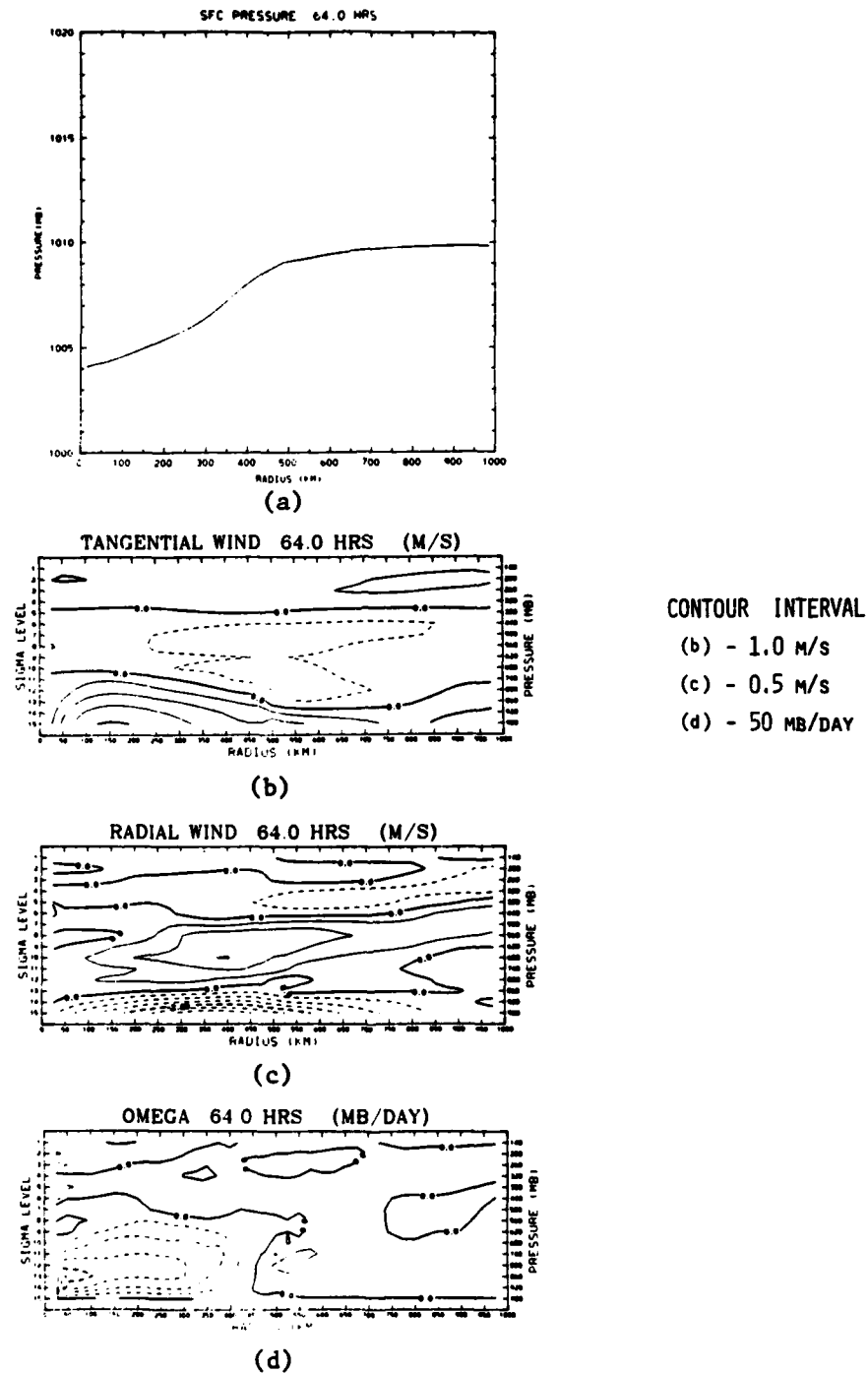
Figure 5.3 Radial distribution of surface pressure (a) and
vertical cross-sections of tangential wind (b), radial wind (c),
and vertical motion (d) at 64 hours for the case of radiative
+ desert sensible forcing in clear air.

the ocean increased from 0.9 mb for radiative forcing only to 5.6 mb when sensible heat was included. A 5.6 mb horizontal pressure gradient is not unreasonable when compared to the July mean surface pressure gradient reported by van de Boogaard (1977). He shows a pressure gradient of about 6-7 mb from the center of the "heat low" to the surrounding ocean. However, the absolute pressures produced by the model are slightly higher than van de Boogaard reports. His data indicate a mean surface pressure in the "heat low" of about 1000 mb in July. Part of the descrepancy may be that the July mean surface pressure is indicative of a "heat low" circulation which is more well developed than the one which was observed and modelled in May. In any event, the surface pressure gradient is more indicative of the intensity of the low than is the absolute magnitude of the surface pressure. The diurnal range of the surface pressure in the "heat low" produced with both radiative and sensible heating -- from 1007.10 to 1004.20 mb -- is smaller than the diurnal range of about 5 mb observed on 10 May 79 for the desert station at Sharouwrah as reported by Blake et al. (1983). However, the time of minimum surface pressure in the model results (1600L) corresponds very well with the observations from Sharouwrah, and the time of the diurnal maximum (0700L) is very near the range of 0800-1100L observed at Sharouwrah on that date.

While the tangential and radial wind fields and the vertical motion fields for both cases have the same general character, some differences are apparent. The circulation in the case with desert sensible heat flux included is considerably stronger than in the case forced only by radiative heating. The maximum near surface wind speeds in the radiative heating case are only on the order of 1.5 m/s

while for the case with radiative and sensible heating, the wind speeds are closer to 5 m/s. The vertical profile of the vertical motion fields at a radius of 200 km over the desert are shown in Figure 5.4. The vertical motion field for the case of radiative forcing only is very weak with a maximum upward vertical motion of about 25 mb/day near 700 mb. However, in the case of radiative + sensible heating, the maximum upward vertical motion occurs near 800 mb and has a magnitude of about 175 mb/day (~2 cm/s). Both cases show that the layer of upward vertical motion extends upward from the surface to ~ 500 mb. The other main difference between the two cases is in the depth of the cyclonic circulation in the lower levels. When the desert sensible heat is included, the cyclonic circulation near the center of the "heat low" extends about 160 mb higher into the troposphere than in the case of radiative heating only. For the case of radiative + desert sensible heating, the low level radial inflow extends from the surface up to 860 mb while the cyclonic circulation in the tangential wind field reaches up to about 670 mb. Above this low level cyclone, the middle troposphere is characterized by an anticyclonic circulation with radial outflow extending from 860 mb to about 380 mb.

This comparison between the circulation included by clear air radiative heating only and the circulation caused by a combination of clear air radiative and desert sensible heating shows that it is the surface sensible heat flux which dominates the "heat low" circulation. While the radiative heating alone is capable of producing a surface "heat low", the circulation is much weaker than the observations support. The large surface sensible heat flux is required to give a
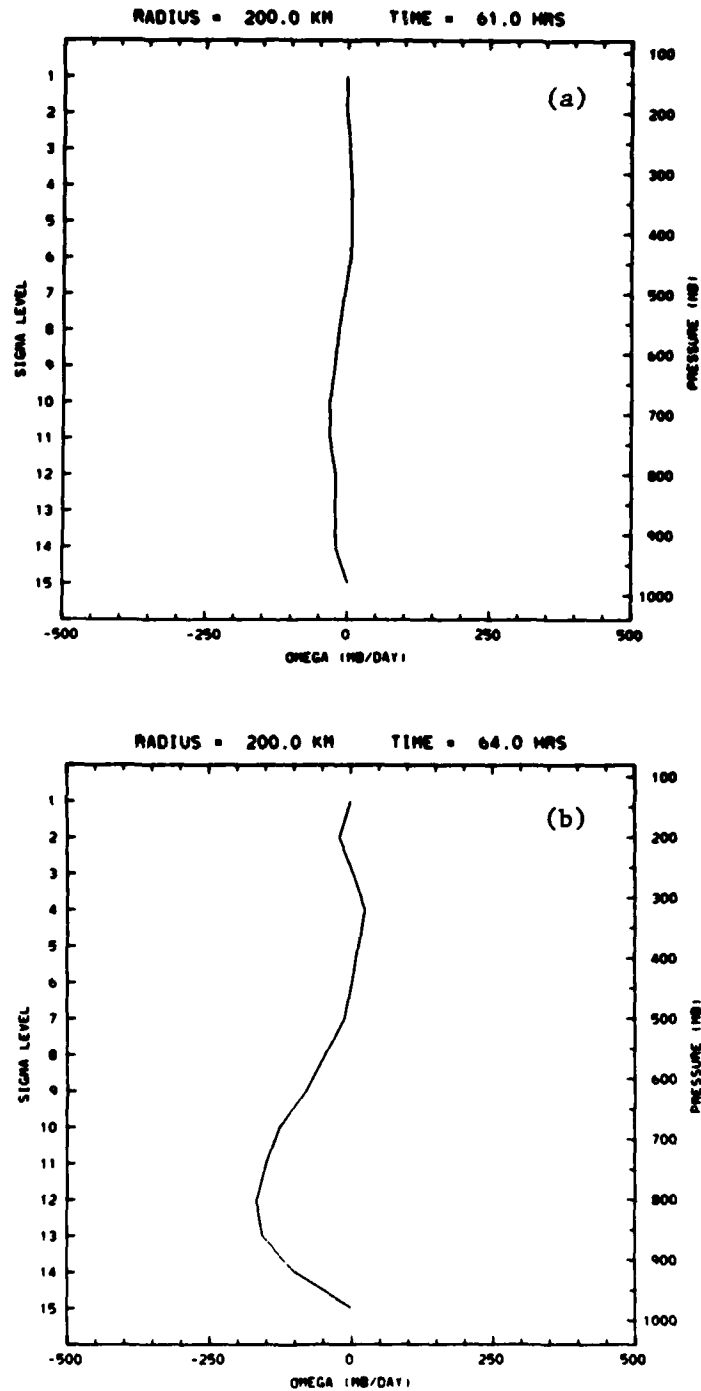
Figure 5.4 Vertical profile of vertical motion at a radius
of 200 km for the case of radiative forcing only at 61 hours
(a) and for the case of radiative + desert sensible forcing
at 64 hours (b) in clear air.

realistic "heat low" circulation. In fact, the circulation produced by clear air radiative heating only is so weak that it can be considered a small perturbation on the flow pattern produced by clear air radiative + desert sensible heating.

4.2 Inclusion of Oceanic Sensible Heat

While the combined effects of the clear air radiative heating and desert surface sensible heat flux were capable of producing a "heat low" circulation with reasonable horizontal pressure gradients and diurnal pressure variations, the temporal variation in the low level temperature field revealed a problem. Figure 5.5 showns the trace of temperature for the lowest layer in the model ($\sigma = 0.97$, p ~ 980 mb) over the desert (37.5 km) and over the ocean (987.5 km). Over the desert, the temperature trace indicates a strong diurnal oscillation which parallels the diurnal input of surface sensible heat. Over the ocean, where there is no surface sensible heat component, the weak diurnal oscillation is caused solely by the diurnal character of the radiative heating. The disturbing characteristic of both curves is the downward trend in temperature. Over the ocean, this trend is not so surprising since there is only subsidence warming and horizontal advection to balance the strong radiative cooling in the lowest layer and neither of these mechanisms is strong enough to balance this cooling. Over the desert, however, one might think that the large diurnal input of sensible heat would balance the radiative cooling in the lowest layer. The reason that the trend is still downward is that the air which is advected into the "heat low" from the ocean is cooled so much radiatively that the sensible heat from the desert surface is
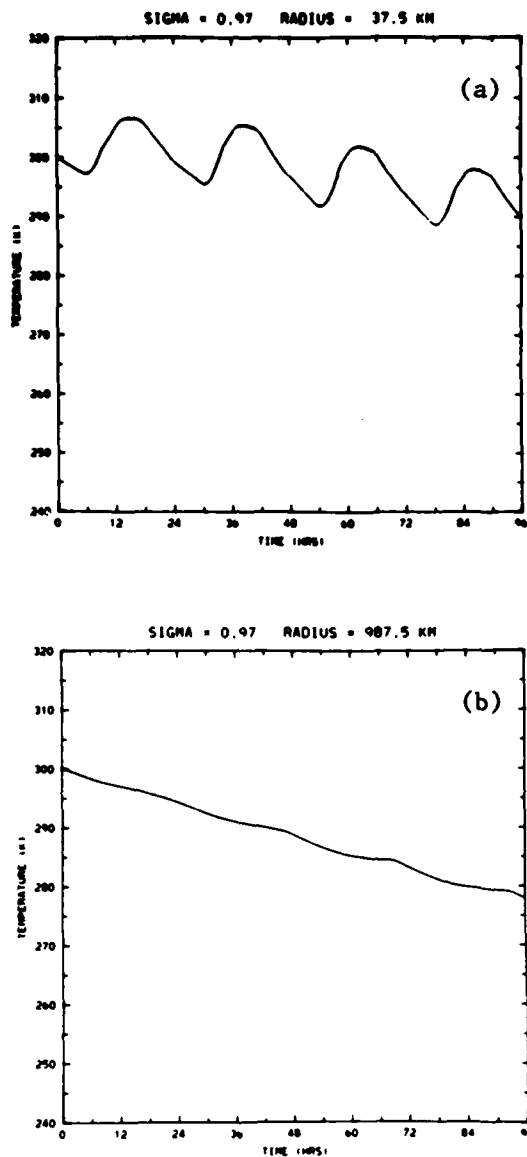
Figure 5.5 Temperature trace in the lowest model layer
($\sigma = 0.97$; p ~ 980 mb) at a radius of 37.5 km (a) and
987.5 km (b) for the case of radiative + desert sensible
forcing in clear air.
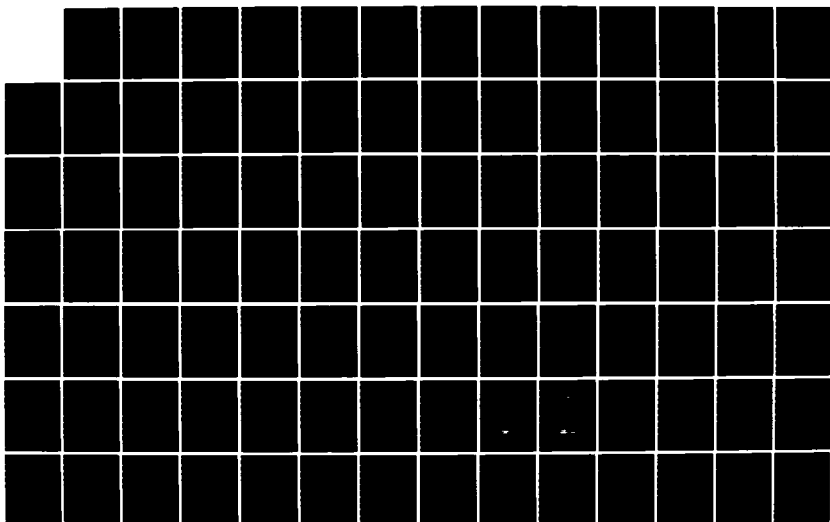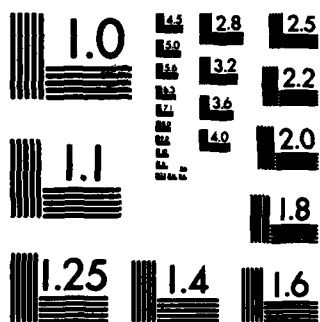
MICROCOPY RESOLUTION TEST CHART

NATIONAL BUREAU OF STANDARDS-1963-A

unable to overcome the cooling and the net effect is long term cooling even over the desert.

This trend in temperature violates our concept of the long term behavior of the atmosphere over the ocean and over the desert. The most likely reason for this trend in the model results is the lack of large scale influences on the limited 2-dimensional model domain. In the real atmosphere, no lateral boundaries exist. Therefore any long term cooling in a localized region would cause an influx of heat from a surrounding region. It is precisely this type of large scale horizontal advection which cannot be accurately included in a simple 2-dimensional regional model. Possible sources of heat external to the model domain are the desert regions which stretch westward across North Africa and the Somali Jet which brings warm tropical air from low latitudes along the coast of east Africa on a southwest to northeast track across the Arabian Sea. The possible impact of the Sahara Desert on the local circulation is examined in Chapter 6. However, in this simplified 2-dimensional, axisymmetric domain, it is not possible to include such external influences explicitly. Nevertheless, since the low level radiative cooling over the ocean was causing this long term downward trend in temperature, an attempt was made to stabilize the temperature field over the ocean in the 2-dimensional model.

One possible method of stabilizing the temperature field is to introduce a heat source in the lowest layers over the ocean. The energy balance at the surface of the ocean can be written

$$R_o = S_o + H_o + LH_o + ST_o \qquad (5.4.1)$$

where R_o is the net radiation at the surface of the ocean, S_o is the sensible heat flux from the ocean to the atmosphere, H_o is the horizontal transport within the ocean, LH_o is the latent heat flux from the ocean to the atmosphere, and ST_o represents the storage of energy in the ocean. From the longwave and shortwave radiative transfer routines IRADLON and IRADSOL, it was possible to determine the net radiation term in the energy balance equation to be about 300 W m^{-2}. The horizontal transport for the Indian Ocean (of which the Arabian Sea is a part) was estimated from data given in Sellers (1965) as about 2 W m^{-2}. Data from the Indian Ocean Expedition (Meteorological Atlas, 1972) were used to determine the magnitude of the latent heat flux to be about 152 W m^{-2}. These values imply that the sum of the sensible heat flux and storage terms in the balance equation must equal 146 W m^{-2}. Most sources put the sensible heat flux from the ocean to the atmosphere at values near zero. However, in most cases, the sensible heat flux is a computed quantity based on the temperature of the ocean surface and the atmosphere just above the ocean surface. If the temperature difference between the atmosphere and ocean is very small, the sensible heat flux will be computed to be very small. It might be argued, however, that the temperature of the air and the ocean surface are nearly equal because sensible heat is being supplied to the atmosphere by a semi-infinite heat reservoir in the ocean.

Assuming the ocean could be a sensible heat source, it was necessary to determine how much oceanic sensible heat would be

required to balance the strong radiative cooling of the atmosphere over the ocean surface. Since the atmosphere immediately above the ocean surface was observed to have a relatively well mixed layer which extended through one and one-half of the 2-dimensional model layers, the net radiative cooling in the lowest two layers over the ocean was computed to be about 6.19 K day^{-1}. In order to balance this amount of cooling, a sensible heat flux of 88 W m^{-2} would be required from the ocean to the atmosphere. That would leave 58 W m^{-2} for storage in the ocean. That magnitude of energy storage would result in a temperature change of about .02 K day^{-1} over the 50 m mixed layer of the ocean -- well within reason. Therefore, based on these assumptions, an experiment was conducted which included sensible heat over the desert and over the ocean. In this experiment, the oceanic sensible heat can be considered a crude parameterization of the large scale horizontal advection processes which cannot be included in the simplified 2-dimensional, axisymmetric domain.

The thermal forcing in this experiment was exactly the same as the thermal forcing for the case of clear air radiative and desert sensible heating described in Section 4.1 except enough sensible heating was allowed from the ocean surface to balance the strong radiational cooling in the lowest two atmospheric layers over the ocean. That is, the thermal forcing of the atmosphere in the lowest two layers over the ocean was essentially zero. The temperature traces of the lowest layer (~980 mb) at 37.5 km and 987.5 km are shown in Figure 5.6. Over the ocean, the temperature trace shows a very slight tendency toward warming. Over the desert, after a slight warming trend which persists for about 48 hours, the temperature trace

81
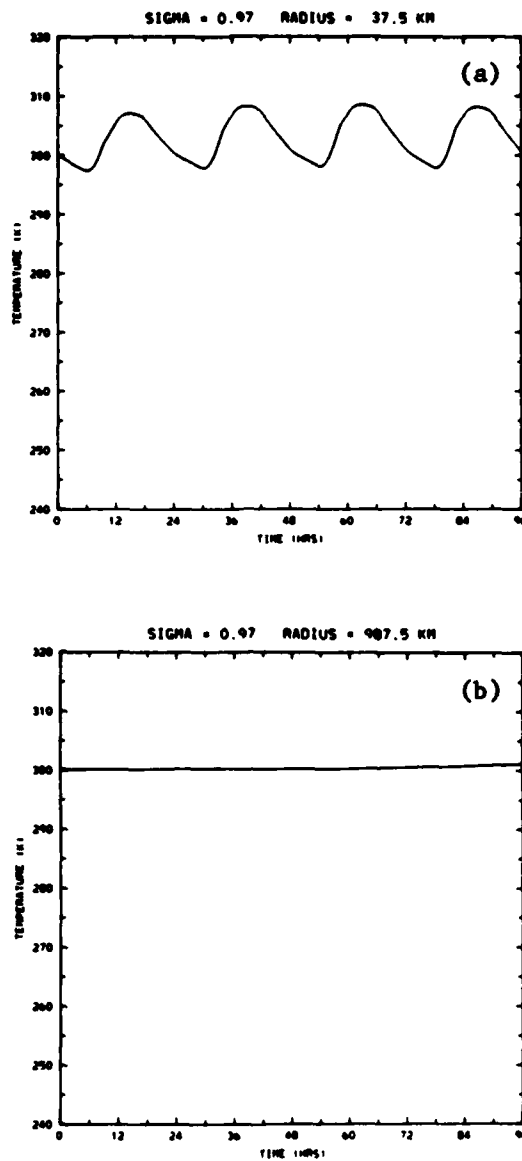
Figure 5.6   Temperature trace in the lowest model layer
(σ = 0.97; p ~ 980 mb) at a radius of 37.5 km (a) and
987.5 km (b) for the case of radiative + desert and oceanic
sensible forcing in clear air.

begins to show a steady state diurnal oscillation about a mean of ~304K with a diurnal maximum of ~308.5K near 1500L and a diurnal minimum of ~298.5K near 0600L. The inclusion of the sensible heating over the ocean is enough of a stabilizing influence to allow the temperature field to become well-behaved.

While the inclusion of the oceanic sensible heat source was able to control the long term downward trend in temperature, it also produced a weaker "heat low". The surface pressure trace near the center of the "heat low" is shown in Figure 5.7, and the radial distribution of the surface pressure (a), and vertical cross-sections of tangential (b) and radial (c) wind components, and the vertical motion (d) at the time of minimum surface pressure (64 hours, 1600L) are shown in Figure 5.8. The inclusion of the oceanic sensible heating results in a decreased horizontal heating gradient in the lower levels of the model atmosphere. Therefore, the "heat low" surface pressure stabilizes to a steady diurnal oscillation between a minimum of about 1006.00 mb and a maximum of about 1009.20 mb with a diurnal mean of about 1007.70 mb. This mean surface pressure is about 2 mb higher than in the case where no oceanic sensible heat is included (Figure 5.1). Also, at 64 hours (1600L), the horizontal pressure gradient between the "heat low" over the desert and the surrounding ocean is reduced from 5.6 mb for the case with no oceanic sensible heat (Figure 5.3a) to about 4 mb for the case where oceanic sensible heat is included (Figure 5.8a). The general character of the circulation, however, remains intact. Nevertheless, the low level cyclonic circulation (Figure 5.8b) is weaker and has less vertical and
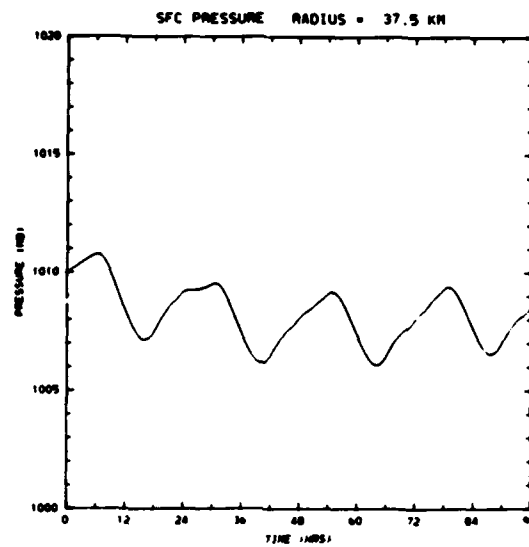
Figure 5.7   Surface pressure trace at a radius of 37.5 km for the case of radiative + desert and oceanic sensible forcing in clear air.

SFC PRESSURE 64.0 HRS

(a)

TANGENTIAL WIND 64.0 HRS   (M/S)

(b)

RADIAL WIND 64.0 HRS   (M/S)

(c)

OMEGA 64.0 HRS   (MB/DAY)

(d)

CONTOUR INTERVAL

(b) - 1.0 M/s

(c) - 0.5 M/s

(d) - 50 MB/DAY

Figure 5.8 Radial distribution of surface pressure (a) and
vertical cross-sections of tangential wind (b), radial wind
(c), and vertical motion (d) at 64 hours for the case of
radiative + desert and oceanic sensible forcing in clear air.

horizontal extent than in the case where no oceanic sensible heating is included (Figure 5.3b).

In summary, the inclusion of a sensible heat source over the oceanic portion of the 2-dimensional model domain may be thought of as a crude parameterization of large scale advective heat sources external to the region of the "heat low". The impact of this oceanic sensible heat on the induced "heat low" circulation is positive in that it provides a method of stabilizing the low level temperature fields. However, because this oceanic heat source reduces the low level horizontal heating gradients from the case where no oceanic sensible heat is included, the intensity of the induced "heat low" circulation is reduced. The general character of the overall circulation -- low level radial inflow into a low level cyclone and rising air over the desert to a middle tropospheric anticyclonic circulation with radial outflow -- is preserved.

4.3 Clear Air vs. Dust Laden Forcing

One of the more interesting experiments conducted with the 2-dimensional model was designed to determine the impact of the dust on the induced circulation. In Chapter 3 it was shown that the extensive dust layer which was observed over the Saudi Arabian desert and the adjacent Arabian Sea during May 1979 was very active in the shortwave portion of the spectrum. In fact, the presence of the dust was capable of increasing the radiative heating of the atmosphere during midday by a factor of two. Also, as was shown in Chapter 4, the dust layer reduced the net radiation at the surface and therefore reduced the amount of surface sensible heat. To examine the impact of these two influences on the induced circulation, every experiment

conducted with the clear air thermal forcing was repeated for the case of a dust laden atmosphere. While the results of only one comparison are presented in this section, in all cases the circulation induced by the dust laden thermal forcing was weaker than the circulation induced by the corresponding clear air thermal forcing.

Figure 5.9 shows the surface pressure trace at a radius of 37.5 km for the case of radiative + desert sensible heating for both the clear air and dust laden atmospheres. The pressure trace for the clear air case is identical to the trace shown in Figure 5.1 and is repeated here for ease of comparison. These surface pressure traces indicate that the primary impact of the dust is to reduce the intensity of the induced "heat low" circulation. In the dust laden case, as in the case of the clear air thermal forcing, the pressure near the center of the "heat low" reaches a diurnally oscillating steady state condition after about 48 hours. The diurnal oscillations in both cases are in phase with one another even though the minimums and maximums have different magnitudes. In the dust laden case, the diurnal minimum in surface pressure of 1005.15 mb occurs near 1600L and the diurnal maximum in surface pressure of 1007.50 occurs near 0700L. Both the diurnal minimum and maximum surface pressures in the dust laden case are about 1 mb higher than in the clear air case. This decrease in intensity of the induced "heat low" is further evidence that the sensible heat flux is the most important component of the thermal forcing. In spite of the fact that the elevated radiative heat source is sometimes twice as strong for the dust laden case than for the clear air case, the reduction in surface sensible
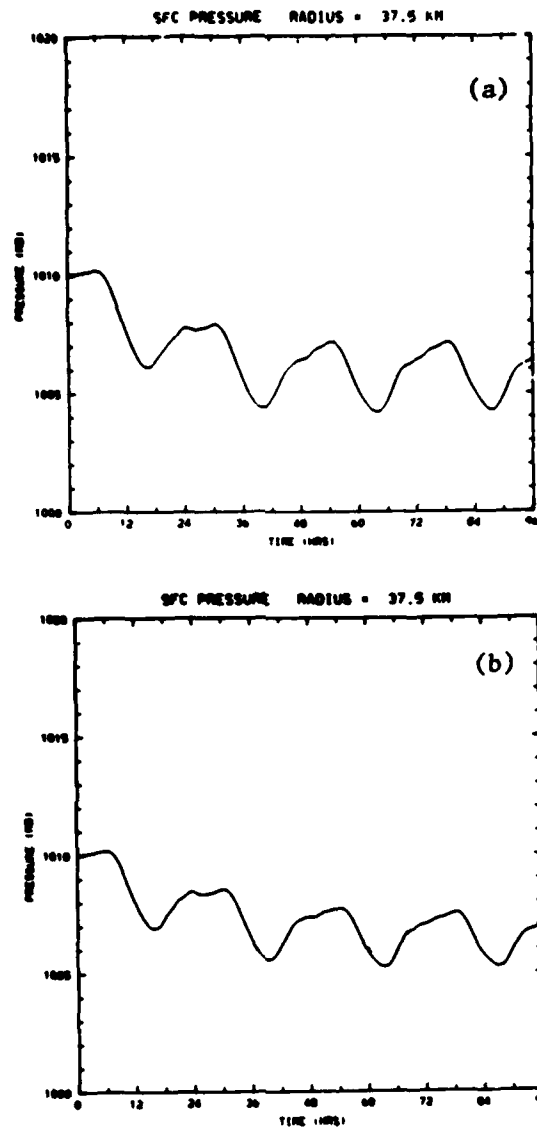
Figure 5.9 Surface pressure trace at a radius of 37.5 km for the case of radiative + desert sensible forcing in clear air (a) and in dust laden air (b).

heat in the dust laden case dominates the circulation and produces a less intense "heat low".

The decrease in intensity of the dust laden "heat low" is also apparent in the radial distribution of surface pressure (a), and vertical cross-sections of tangential (b), and radial (c) wind components, and vertical motion (d) shown in Figure 5.10. This figure should be compared with Figure 5.3 for the case of clear air radiative and desert sensible heating. Both Figures 5.10 and 5.3 are for the same elasped time into the model run -- 64 hours (1600L). Except for slightly smaller magnitudes, the fields in the dust laden case are identical to those in the clear air case. Low level inflow from the ocean to the desert into a low level cyclone produces rising motion over the desert. The rising air flows outward from the desert to the ocean in a mid-level anticyclone and then subsides over the ocean. About the only noticeable difference between the clear air and dust laden circulations is in the vertical profile of the vertical motion at a radius of 200 km shown in Figure 5.11. In the dust laden case, the peak in upward vertical motion is rather broad and flat as opposed to the clear air case where the peak is more well defined. The broader peak in the dust laden case is most probably a reflection of the impact of the dust on the radiative heating profile. The dust provides a stronger radiative heating in the layers of the atmosphere away from the surface than in the clear air case. As a result, the upward motion above about 800 mb in the dust laden case is somewhat stronger than the upward motion closer to the surface. Nevertheless, the reduction of surface sensible heat causes weaker upward vertical motion in the dust laden case than in the clear air case. Even in the

(a)

(b)

(c)

(d)

CONTOUR INTERVAL

(b) – 1.0 M/s

(c) – 0.5 M/s

(d) – 50 MB/DAY

Figure 5.10 Radial distribution of surface pressure (a), and
vertical cross-sections of tangential wind (b), radial wind (c),
and vertical motion (d) at 64 hours for the case of radiative
+ desert sensible forcing in dust laden air.

RADIUS = 200.0 KM   TIME = 64.0 HRS

(a)

RADIUS = 200.0 KM   TIME = 64.0 HRS

(b)
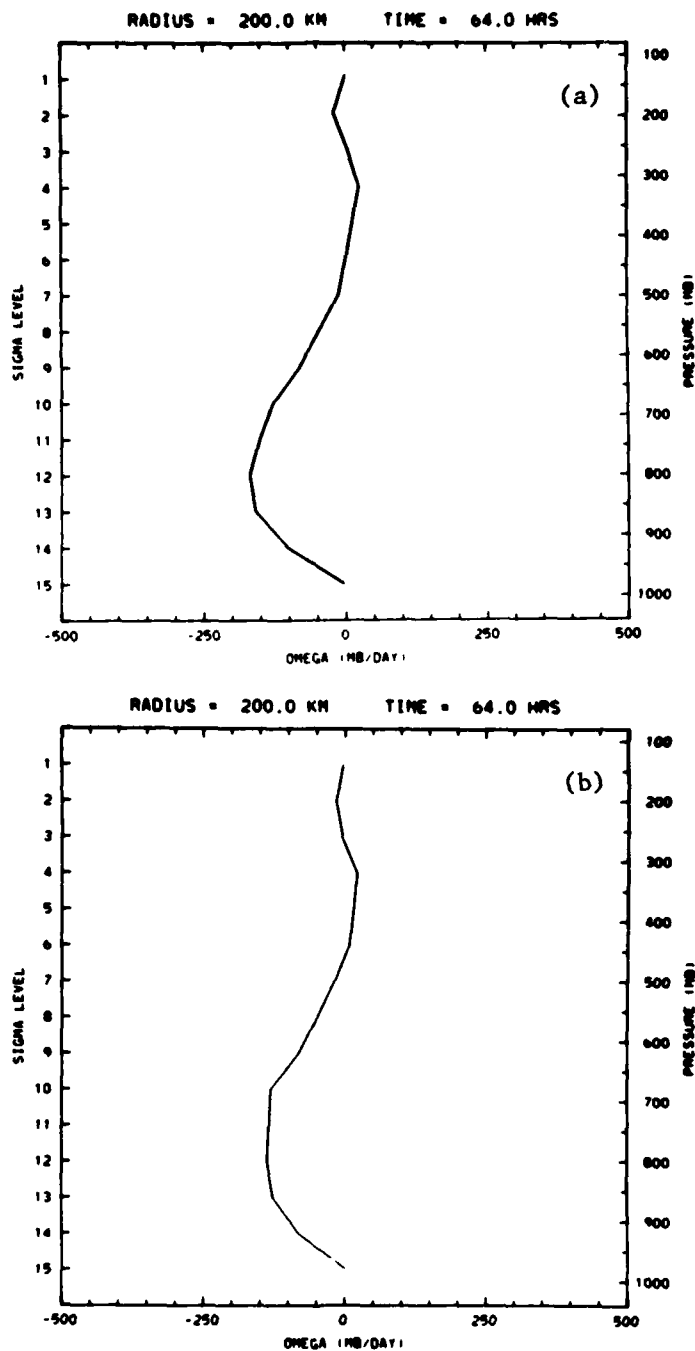
Figure 5.11   Vertical profile of vertical motion at a radius of
200 km for the case of radiative + desert sensible forcing at
64 hours for clear air (a) and dust laden air (b).

vertical distribution of the vertical motion, the effect of the dust is slight.

In summary, the impact of the dust on the induced "heat low" circulation is to produce a less intense circulation than in the case of a clear atmosphere. This reduction in intensity is a result of the smaller amount of surface sensible heat which is available in the dust laden case because of the increased absorption of shortwave radiation by the dust. The increased radiative heating during midday caused by this absorption of shortwave radiation by the dust has little impact on the induced circulation. In effect, the dust moderates the intensity of the "heat low" circulation.

4.4 Diurnal Character of the Circulation

In all the experiments conducted with a diurnally varying thermal forcing, a distinct diurnal pattern emerged in the induced circulation. This pattern was present in the cases with radiative forcing only, radiative + desert sensible forcing, radiative + desert and oceanic sensible forcing, and regardless of whether the clear air or dust laden thermal forcings were used. This diurnal character is illustrated in this section with the results from the experiment conducted using the clear air radiative + desert and oceanic sensible forcing. However, it must be remembered that this diurnal character is not unique to that experiment.

Shown in Figures 5.12-5.15 are the radial distribution of surface pressure (a), and vertical cross-sections of tangential (b), and radial (c) wind components, and vertical motion (d) at six hour increments from 52 hours (0400L) to 70 hours (2200L) during the third day of the model run. Also included in each figure is the vertical

distribution of vertical motion (e) at a radius of 200 km -- about halfway from the center of the desert to the shore of the oceanic portion of the model domain. These figures illustrate the essentials of the diurnal character of the induced circulation.

At 52 hours (0400L), the surface pressure near the center of the "heat low" is about 1008.80 mb and the horizontal pressure gradient between the desert and the ocean is about 1.2 mb. The dynamical fields show a well developed cyclone which extends from the surface to about 800 mb over the whole domain (Figure 5.12b). The maximum tangential wind is about 6.0 m/s over the desert. A mid-level anticyclone extends from 800 mb up to about 550 mb and is characterized by a maximum tangential wind speed of slightly over 3 m/s at a radius of 500 km. The radial wind field (Figure 5.12c) indicates the lower troposphere is characterized by radial outflow from the surface up to about 800 mb over the desert. Above this layer of outflow, the radial wind field exhibits a region of inflow from the ocean to the desert which extends up to about 560 mb over the desert. The maximum inflow is about 1.8 m/s at 650 mb at a radius of 300 km. The vertical motion field over the desert shows a deep layer of subsidence which extends downward to the surface from about 580 mb. Between 580 and 320 mb, weak rising motion is observed over the desert. In the vertical, the radial wind field and vertical motion field exhibit a two cell circulation. In the middle troposphere, radial inflow produces subsidence in the lower troposphere and slight upward motion above the inflow region. The lower and upper tropospheres are characterized by outflow from the desert to the

(a)

(b)

(c)

(d)

(e)

CONTOUR INTERVAL

(b) – 1.0 M/S

(c) – 0.5 M/S

(d) – 50 MB/DAY

Figure 5.12 Radial distribution of surface pressure (a), and
vertical cross sections of tangential wind (b), radial wind (c),
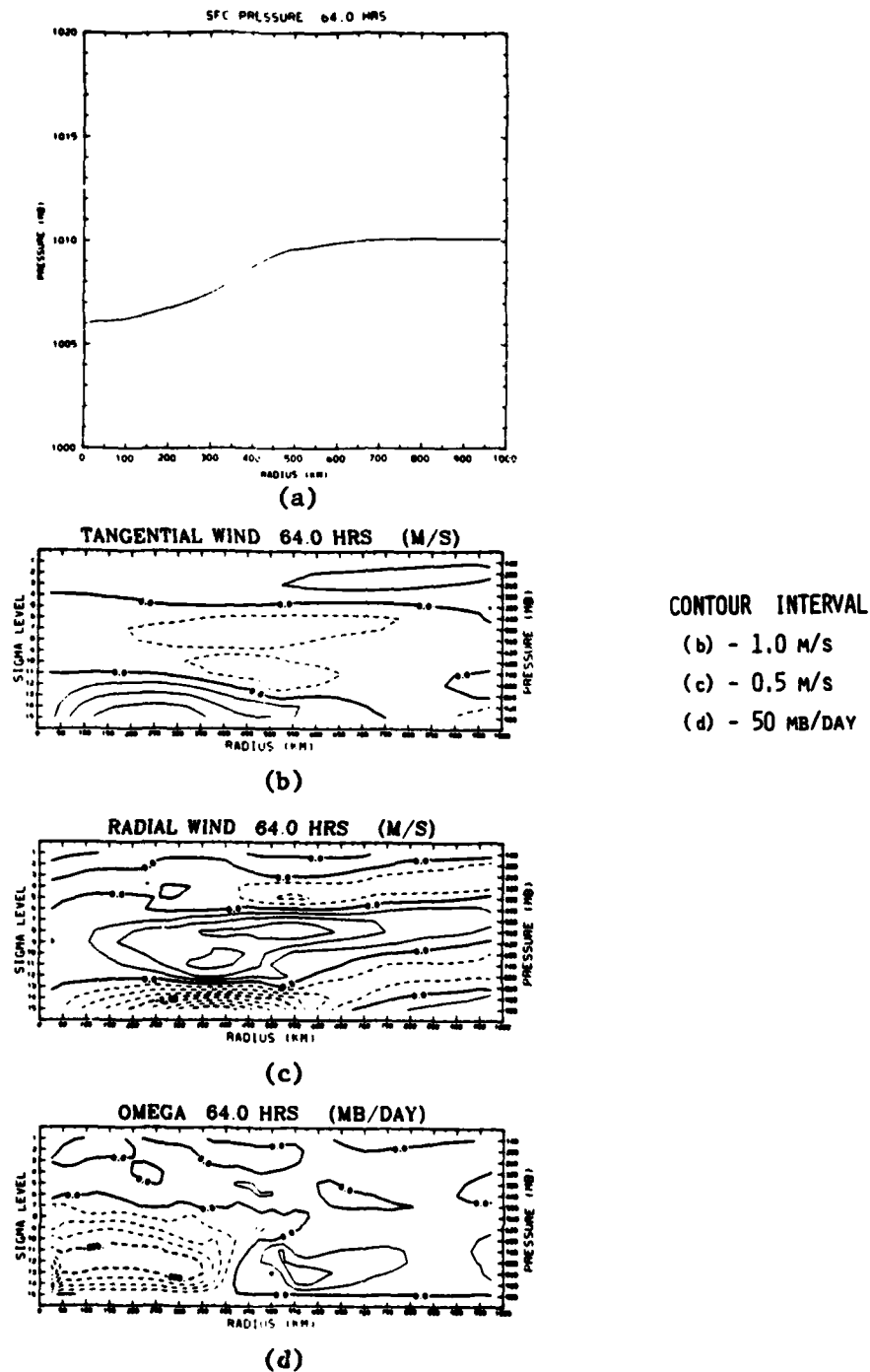and vertical motion (d), and vertical profile of vertical
motion at 200 km (e) at 52 hours for the case of radiative
+ desert and oceanic sensible forcing in clear air.

ocean. At this time in the diurnal cycle, only radiative forcing is at work.

During the next six hours, the surface pressure near the center of the "heat low" reaches its diurnal maximum of 1009.20 mb at about 55 hours (0700L). Also, after sunrise, the sensible heat component in the thermal forcing becomes active and the input of sensible heat begins to be reflected in the low level circulation over the desert. The transition from the early morning circulation shown in Figure 5.12 to a late afternoon circulation is evident by 1000L.

By 58 hours (1000L), the surface pressure has begun to fall and has decreased about 1 mb below its 0700L maximum to 1008.20 mb (Figure 5.13a). While the radial outflow in the lower levels over the desert persists (Figure 5.13c), the field is very noisy, very shallow, and very weak. The vertical motion field begins to show evidence of reversing the subsidence in the lower levels over the desert (Figures 5.13d,e). The low level radial outflow has weakened the surface cyclonic circulation and the maximum tangential wind is less than 4 m/s. This decrease in intensity of the low level cyclonic circulation is caused primarily by the action of the Coriolis term in the tangential momentum equation. The radial outflow forces a decrease in the intensity of the low level cyclone. At this hour, the impact of the surface sensible heat over the desert is still confined to the lowest layer of the atmosphere since the mixed layer growth doesn't penetrate through the surface based early morning inversion before about 1200L (see Chapter 4). This time, 1000L, represents the beginning of the transition from the early morning pattern to the intense afternoon "heat low" circulation.

SFC PRESSURE   58 0 HRS

(a)

TANGENTIAL WIND   58.0 HRS   (M/S)

(b)

CONTOUR   INTERVAL

(b) - 1.0 m/s

(c) - 0.5 m/s

(d) - 50 mb/DAY

RADIAL WIND   58.0 HRS   (M/S)

(c)

OMEGA   58.0 HRS   (MB/DAY)

RADIUS = 200.0 KM   TIME = 58.0 HRS

(d)

(e)
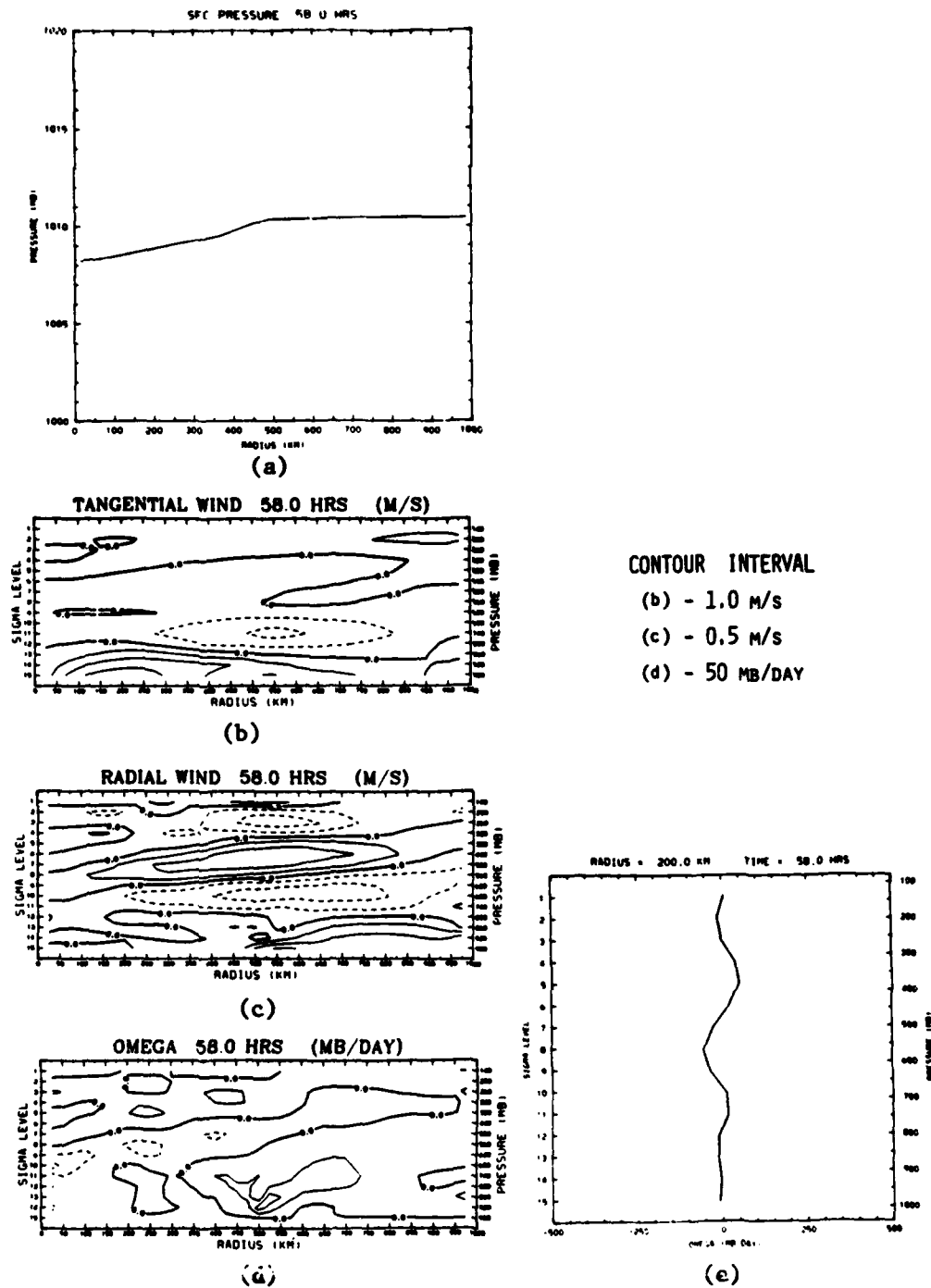
Figure 5.13   Radial distribution of surface pressure (a), and
vertical cross sections of tangential wind (b), radial wind (c),
and vertical motion (d), and vertical profile of vertical
motion at 200 km (e) at 58 hours for the case of radiative
+ desert and oceanic sensible forcing in clear air.

During the next six hours, the surface sensible heating causes a rapid growth of the mixed layer through a depth of about 350 mb (see Chapter 4). This results in a distribution of the surface sensible heat through a deep layer of the atmosphere. The impact on the circulation is to produce a well developed "heat low" over the desert.

At 64 hours (1600L), the diurnal heating pattern has nearly been completed. Within two hours (between 1700 and 1800L), the surface sensible heat flux changes from a heat source for the atmosphere to a heat sink. The surface pressure has reached its diurnal minimum of ~1006.00 mb (Figure 5.14a). The low level radial outflow from the desert to the ocean which was still present at 1000L has been replaced by radial inflow. This low level radial inflow into the surface cyclone is very intense and extends from the surface up to ~860 mb (Figure 5.14c). The weakening of the low level cyclone over the desert stops when the radial outflow becomes radial inflow. The low level cyclone at 64 hours (1600L) is strengthening and extends vertically from the surface to about 750 mb (Figure 5.14b). The vertical motion field (Figures 5.14d,e) indicates upward vertical motion from the surface to ~500 mb with a peak around 800 mb. This low level inflow and rising air over the desert is compensated by mid-level outflow between 860 and 440 mb and subsidence over the ocean. By 1600L, the classic "heat low" circulation has been established.

Between 1600L and 2200L, the surface sensible heat flux is directed downward with the atmosphere cooling rapidly in the lowest layer. The surface pressure near the center of the low begins to increase from its diurnal minimum at 1600L. Despite the shut off of

CONTOUR INTERVAL
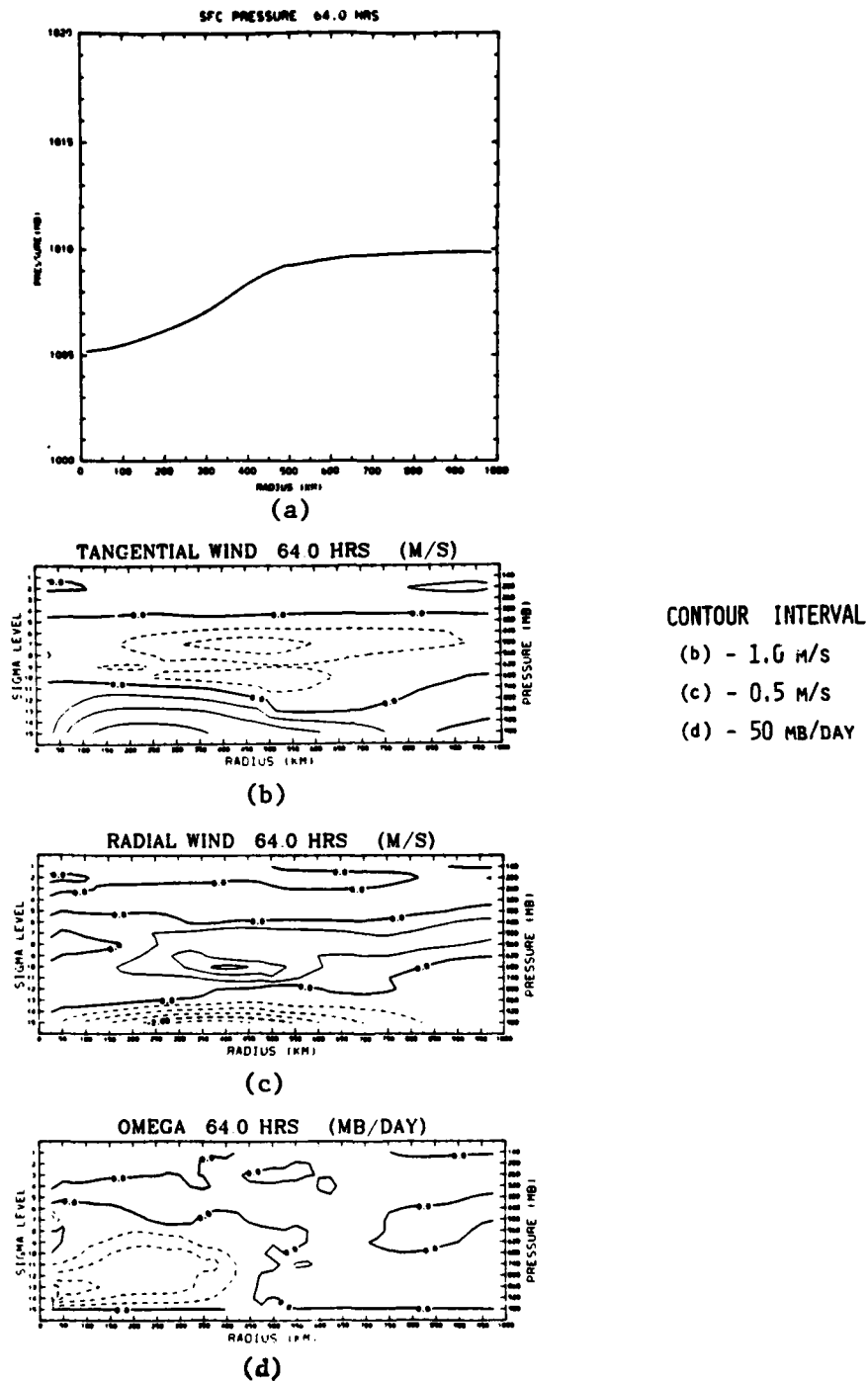
(b) – 1.0 m/s

(c) – 0.5 m/s

(d) – 50 mb/day
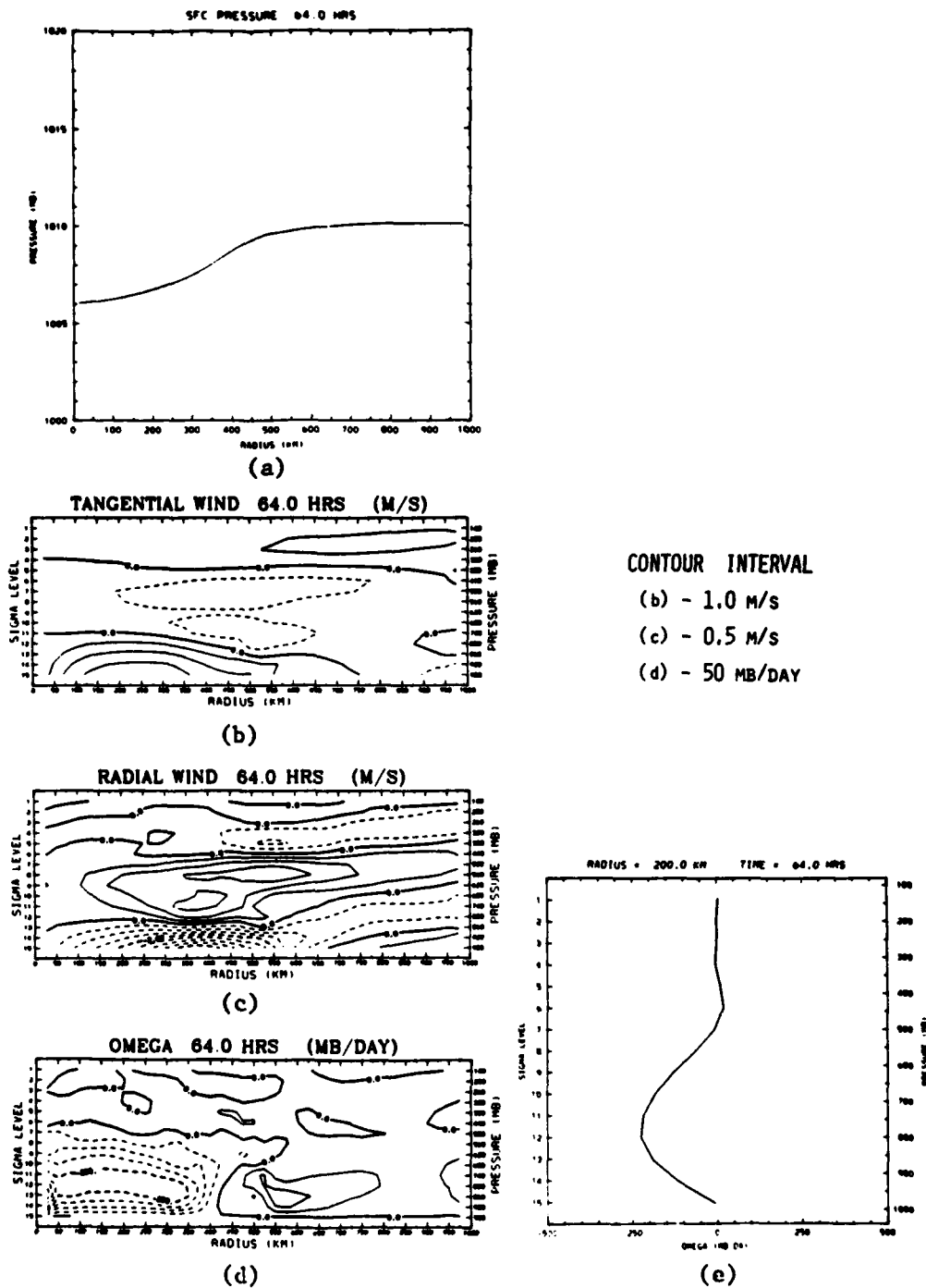
Figure 5.14 Radial distribution of surface pressure (a), and
vertical cross sections of tangential wind (b), radial wind (c),
and vertical motion (d), and vertical profile of vertical
motion at 200 km (e) at 64 hours for the case of radiative
+ desert and oceanic sensible forcing in clear air.

sensible heat over the desert, the inertia of the atmosphere continues the low level radial inflow into the low level cyclone. The corresponding vertical motion pattern shows upward vertical motion continuing over the desert.

By 70 hours (2200L), the transition to the early morning pattern has begun. The surface pressure continues to rise and has reached a value of 1007.6 mb (Figure 5.15a). The low level radial inflow is weakening and within 3-4 hours it will change direction. However, because the low level inflow from the ocean to the desert persists (Figure 5.15c), the low level cyclonic circulation continues to intensify through the action of the Coriolis term and maximum tangential wind speeds have reached ~8 m/s (Figure 5.15b). The magnitude and vertical extent of the upward vertical motion field over the desert have decreased since 1600L and the subsidence above the surface cyclone has intensified and extends down to about 740 mb. The mid-level radial outflow is confined to the region between about 860 and 560 mb (Figure 5.15c). During the next six hours, the transition to the early morning patterns exhibited in Figure 5.12 is completed.

Several observations can be made by examining these figures representing a diurnal cycle for the "heat low" circulation induced by radiative + desert and oceanic sensible heating. First, the circulation pattern in general appears to fit preconceived notions of how the circulation works. Low level inflow was expected into a low level cyclone with rising air over the desert and mid-level outflow to a region of subsidence over the ocean. Indeed, this pattern is evident in the late afternoon when the surface pressure is at a minimum in the "heat low" and the surface pressure gradient is a

SFC PRESSURE 70.0 HRS

(a)

TANGENTIAL WIND 70.0 HRS   (M/S)

(b)

CONTOUR INTERVAL

(b) - 1.0 M/s
(c) - 0.5 M/s
(d) - 50 MB/DAY

RADIAL WIND 70.0 HRS   (M/S)

(c)

RADIUS = 200.0 KM   TIME = 70.0 HRS
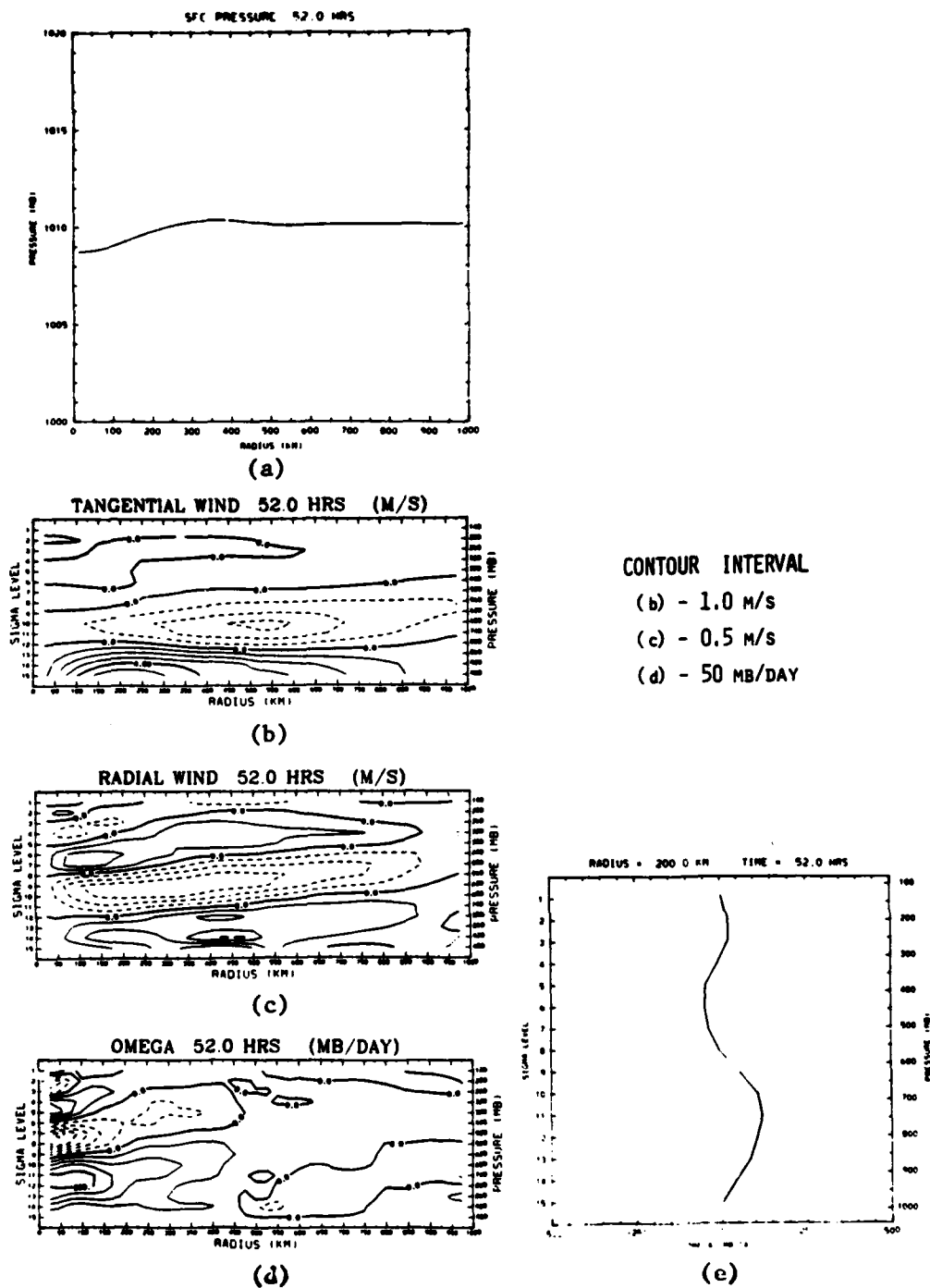
OMEGA 70.0 HRS   (MB/DAY)

(d)

(e)

Figure 5.15 Radial distribution of surface pressure (a), and
vertical cross sections of tangential wind (b), radial wind (c),
and vertical motion (d), and vertical profile of vertical
motion at 200 km (e) at 70 hours for the case of radiative
+ desert and oceanic sensible forcing in clear air.

maximum. The interesting thing about the late afternoon (64 hours; 1600L; Figure 5.14) pattern is that the cyclonic circulation extends up to nearly 750 mb and that upward vertical motion persists up to about 500 mb. The vertical extent of both these motions is much deeper than has been previously thought to be correct. Most previous estimates of the depth of the layer of upward vertical motion (Rao, 1976; Blake et al., 1983) have indicated that the "heat low" is characterized by a layer of upward vertical motion which extends only about 150 mb above the surface. Therefore, the vertical extent of the induced circulation is quite surprising. Second, the surface pressure pattern and the wind fields do not change in phase. The pressure in the "heat low" reaches its diurnal minimum at 1600L. However, the cyclonic circulation does not reach its maximum intensity until about 2200L -- a full six hours later. Both the radial inflow and upward vertical motion reach maximum intensity near 1900L. The pressure reaches its diurnal maximum at 0700L as do the radial outflow and subsidence over the desert. However, the cyclonic circulation doesn't reach its minimum intensity until about 1100L. This lag time in the cyclonic circulation indicates that there is a certain inertia in the atmosphere such that it cannot react instantaneously to changes in the imposed forcing. For example, even though the surface sensible heating is shut off by 1700L, the radial inflow and upward vertical motion continue to intensify for about two hours. Finally, the inflow begins to weaken as the surface pressure gradient weakens. However, the radial inflow doesn't reverse itself until about 0100L when it becomes outflow. Because of the persistent but weakening radial inflow from 1900-0100, the low-level cyclonic circulation continues to

intensify reaching its maximum intensity around 2200L. After 2200L, the inflow is so weak that no appreciable intensification of the cyclonic circulation occurs.

It should be emphasized again that this diurnal pattern was not unique to this experiment. While differences exist in the magnitudes of the variables, this same diurnal pattern was evident in all the experiments conducted with diurnally varying thermal forcing.

4.5 Steady vs. Time Dependent Forcing

Several experiments were conducted to examine the induced circulation when the thermal forcing was steady and did not vary in time. For these experiments, the forcing over the desert and over the ocean was set to a value representative of the net forcing during a full 24 hour diurnal cycle. For each of the 15 model layers, the net 24 hour radiative and sensible heating was determined. Then, the model was run with the forcing in each layer at each time step such that the total forcing applied over 24 hours was equal to the 24 hour total forcing determined for that layer. The horizontal structure of the forcing was left intact. In this section, the vertical structure of the net 24 hour forcing is described for both clear air and dust laden cases. Then, the induced circulation from the steady forcing experiment for the clear air radiative and desert sensible forcing case are compared to the late afternoon induced circulation from the corresponding diurnally forced case.

The vertical profiles of the net 24 hour radiative + sensible heating over the desert and the net 24 hour radiative heating over the ocean for the clear air and dust laden cases are shown in Figure 5.16. Figures 5.16a and b clearly illustrate the impact of the dust on the

(a)

(b)
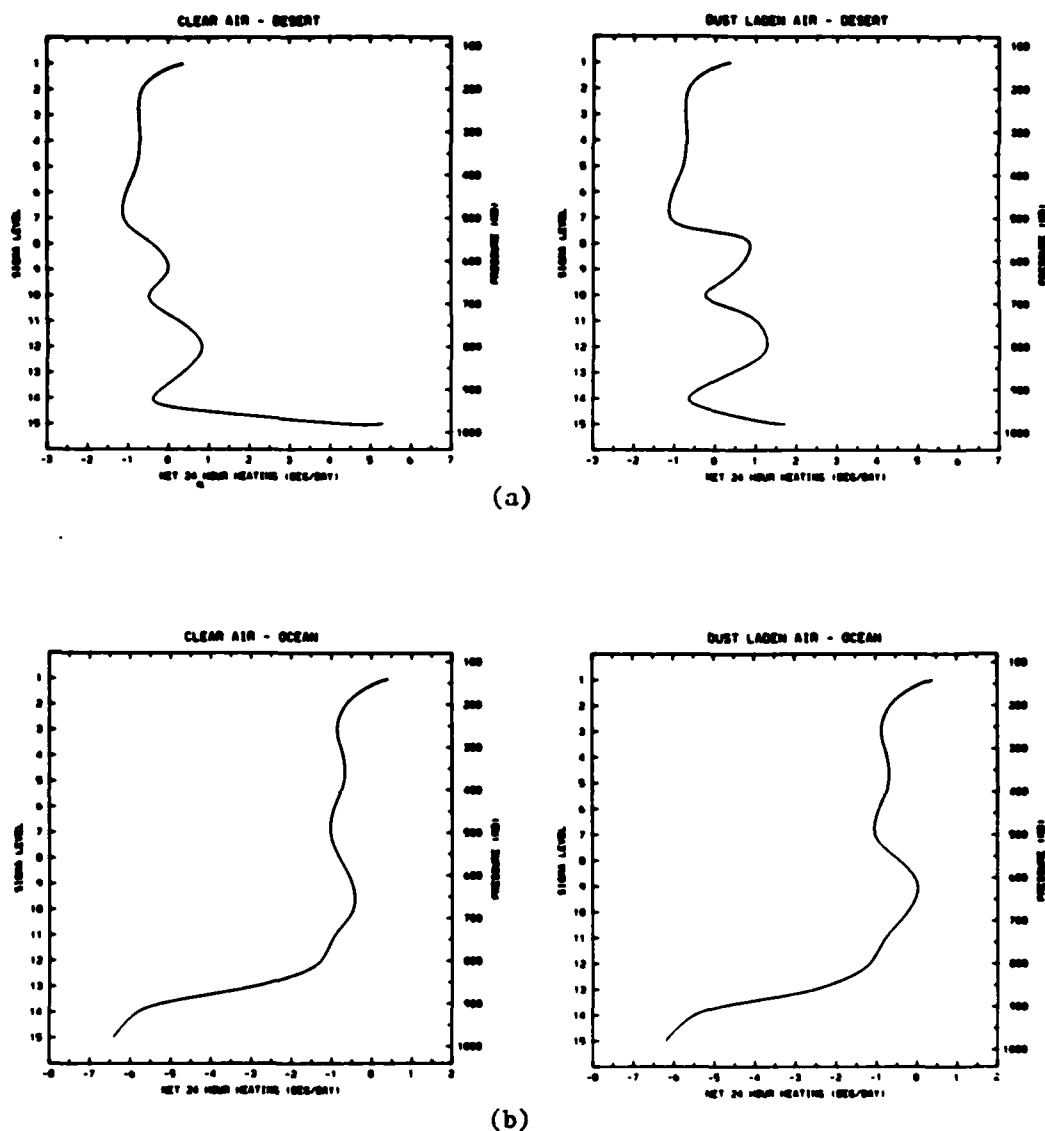
Figure 5.16   Vertical profiles of the net 24 hour radiative
+ sensible heating for clear and dust laden cases over the
the desert (a) and radiative heating for clear and dust
laden cases over the ocean (b).

heating profiles over the desert. The strong sensible heat flux into the lowest layer in the clear air case is sufficient to cause a net 24 hour heating in this layer of more than 5 K/day. However, in the dust laden case, the net 24 hour heating is only -1.7 K/day in the lowest layer. In the mid levels, between 800 mb and 560 mb, it is the radiative heating caused by the dust which makes the net 24 hour heating more intense in the dust laden case than in the clear air case. Above 500 mb, the clear air and dust laden profiles are identical. Comparing Figures 5.16a and b with the desert profiles in Figure 3.2 gives an idea of the impact of the sensible heating on the net 24 hour profiles. Because at its peak, the mixed layer only reaches up to about 650 mb, the impact of the sensible heat is confined to the region below 650 mb (σ level ~9.5). Most of the impact of the sensible heat is in the lowest model layer. Figure 4.10 shows that the mixed layer growth doesn't move through 950 mb (the top of the lowest model layer) until about six hours after sunrise. So, for the first six hours, all of the sensible heat is being applied to the lowest model layer. After this initial period, the mixed layer growth is very rapid up to about 650 mb. Because the sensible heat is being applied over a much deeper layer, the magnitude of the sensible heating in each layer is greatly reduced. The result is that the sensible heating impact is greater in the lowest layer than in the layers above. For example, in the clear air case, the net 24 hour sensible heating in the lowest layer is capable of changing a net 24 hour radiative cooling (Figure 3.2) of about 5 K/day into a net 24 hour total heating (Figure 5.16a) of about 5.3 K/day. However, in the layer just above the lowest layer, the net 24 hour radiative cooling

(Figure 3.2) of 3.1 K/day is reduced only to 0.4 K/day (Figure 5.16a).
Near the top of the mixed layer, the impact is even smaller. At
~680 mb (σ ~10), the 24 hour net radiative cooling (Figure 3.2)
of 0.65 K/day is only reduced to 0.45 K/day (Figure 5.16a). The
impact of the sensible heat in the dust laden case is less impressive
because there is less sensible heat available due to the larger
radiative absorption induced by the presence of the dust.

The results of the steady forcing experiment for the case of
clear air radiative + desert sensible heating (Figure 5.16a,c) are
shown in Figures 5.17 and 5.18. The surface pressure trace at 37.5 km
(Figure 5.17) shows a gradual decline for about 65 hours. Thereafter,
the pressure is nearly constant at ~1004.00 mb. Also shown in
Figure 5.17 is the surface pressure trace from the diurnally forced
experiment. The quasi-steady state pressure of ~1004 mb in the
steady forcing experiment is about the same as the diurnal minimum
pressure which occurred in the case of diurnal forcing. Figure 5.18
shows the instantaneous fields at 65 hours for the steady forcing
experiment. This time is shortly after the surface pressure has
stabilized. The fields in Figure 5.18 should be compared to the
fields for the diurnally forced case shown in Figure 5.3. The radial
distribution of surface pressure (Figure 5.18a) is nearly identical to
the case where the forcing was diurnal (Figure 5.3a). While the wind
fields in the steady forcing case (Figure 5.18b-d) are more noisy than
in the case with diurnal forcing (Figure 5.3b-d), the general pattern
is the same. The radial wind field (Figure 5.18c) is characterized by
low level radial inflow from the ocean to the desert which extends
from the surface up to ~890 mb and a region of mid-level outflow
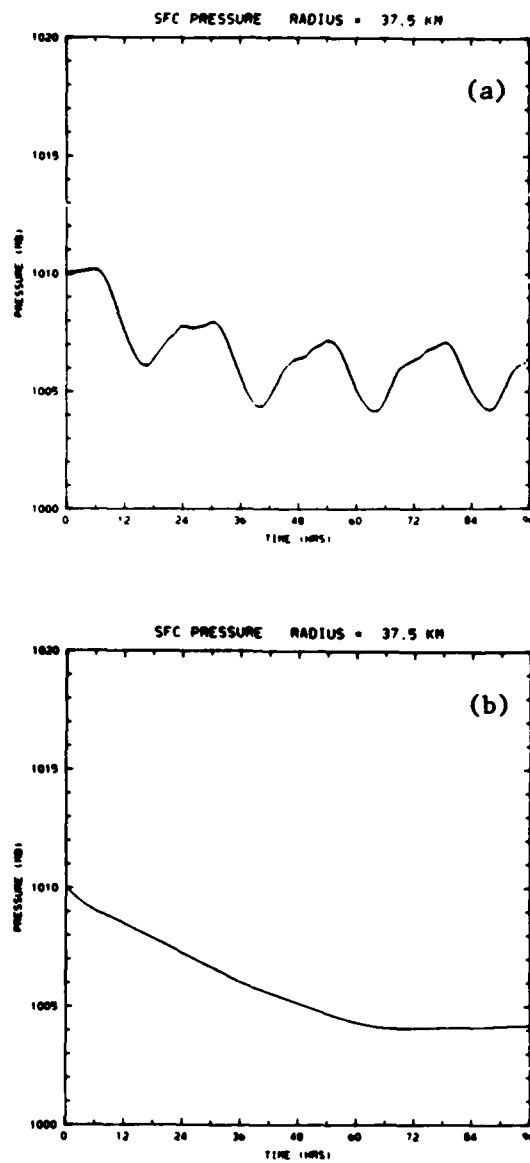
Figure 5.17 Surface pressure trace at a radius of 37.5 km
for the case of diurnal (a) and net 24 hour steady (b)
radiative + desert sensible forcing in clear air.

SF(PRESSURE

(a)

TANGENTIAL WIND   65.0 HRS   (M/S)

(b)

RADIAL WIND   65.0 HRS   (M/S)

(c)

OMEGA   65.0 HRS   (MB/DAY)

(d)

CONTOUR   INTERVAL
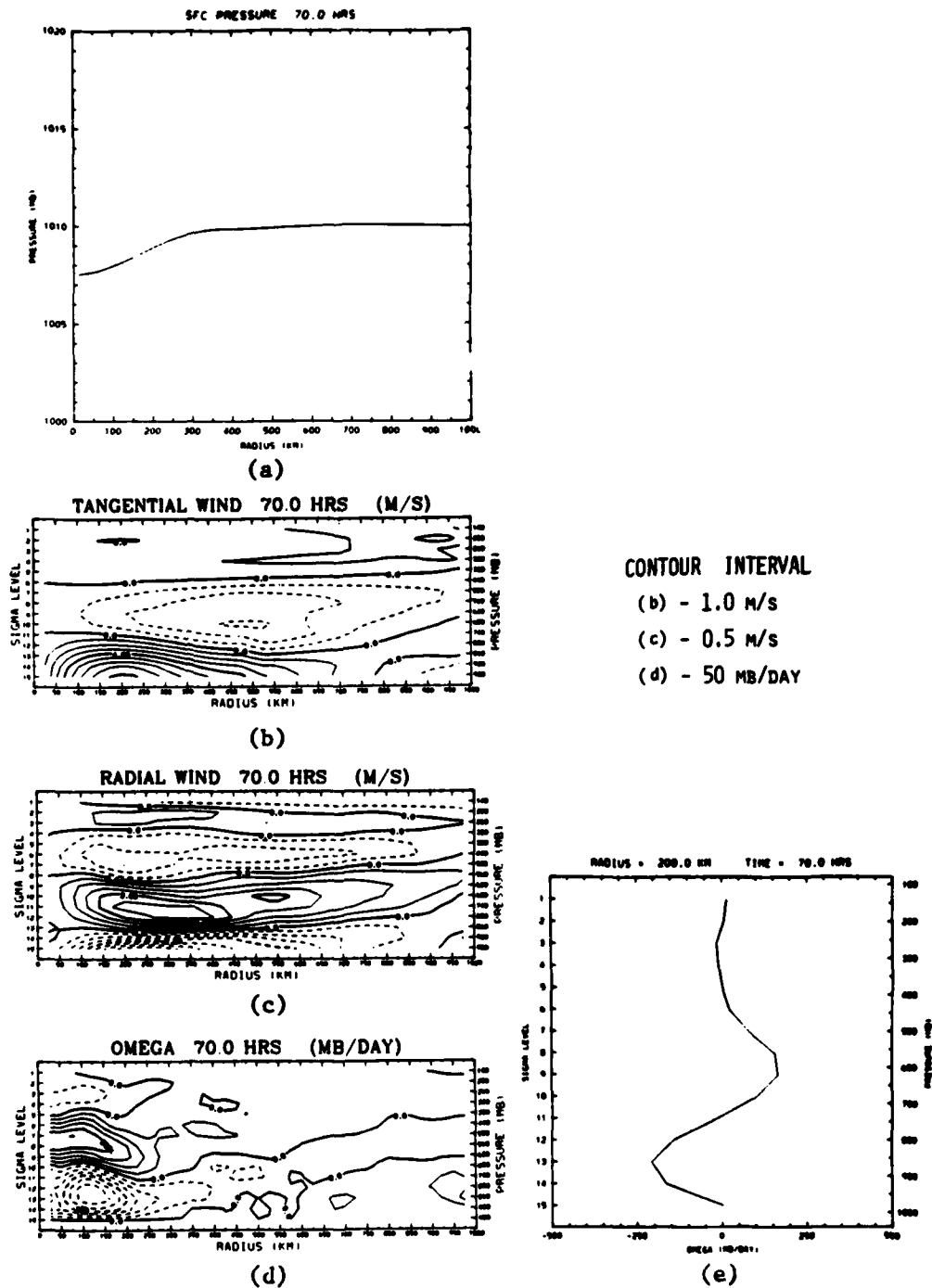
(b) - 1.0 M/S

(c) - 0.5 M/S

(d) - 50 MB/DAY

Figure 5.18   Radial distribution of surface pressure (a), and
vertical cross-sections of tangential wind (b), radial wind (c),
and vertical motion (d), at 65 hours for the case of net 24
hour steady radiative + desert sensible forcing in clear air.

from ~890 mb up to ~500 mb. The outflow is interrupted between 680 and 620 mb by a region of weak inflow which extends about half the horizontal extent of the domain. The radial wind field is accompanied by a tangential wind field (Figure 5.18b) characterized by a cyclonic circulation in the lower levels extending up to ~600 mb over the desert with a middle level anticyclone aloft. The vertical motion field (Figure 5.18d) shows rising air over the desert from the surface to about 620 mb and subsiding air over the ocean. The vertical motion field between 680 and 620 mb does indicate a region of slight downward motion near the center of the surface low which corresponds to the radial inflow occurring at those levels.

The experiment with steady forcing produced dynamical fields which were similar in form to the late afternoon dynamical fields produced in the diurnally forced experiment. However, the fields in the steady forcing case were weaker than the diurnally forced case. This is especially apparent when comparing the vertical profile of the vertical motion fields over the desert at a radius of 200 km. Figure 5.19 indicates a shallower region of appreciable upward vertical motion for the clear air steady forcing case than is shown for the diurnally forced case. Also, the peak in the upward vertical motion of ~65 mb/day is only about 33% as large as the ~180 mb/day peak in the diurnally forced case. Nevertheless, the general pattern in the results -- low level inflow in a cyclonic circulation, rising air over the desert, mid-level outflow in an anticyclonic circulation, and subsiding air over the ocean -- is common to both cases. Only the magnitudes change from one case to another.

RADIUS = 200.0 KM   TIME = 64.0 HRS

(a)

RADIUS = 200.0 KM   TIME = 65.0 HRS

(b)
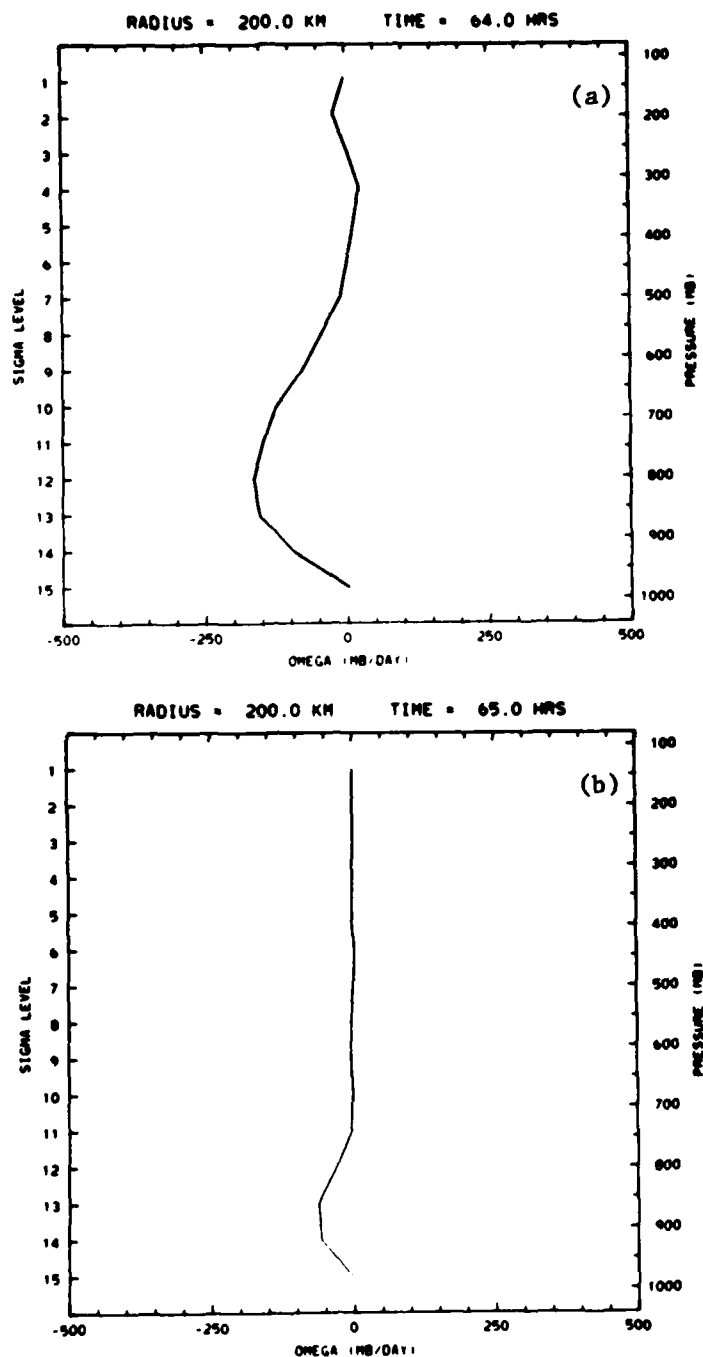
Figure 5.19 Vertical profile of vertical motion at a radius
of 200 km for the case of diurnal (a) and net 24 hour steady
(b) radiative + desert sensible forcing in clear air at 64
and 65 hours, respectively.

4.6   Impact of Varying Desert Size - 300 km and 700 km Deserts

Two experiments were conducted with the 2-dimensional axisymmetric model to determine whether or not the resulting circulation patterns were sensitive to the relative size of the model domain which was characterized as desert or ocean. In all the previous experiments, the desert characteristics were applied through half the radius of the model domain (0-500 km) and oceanic characteristics over the remainder (500-1000 km). In the two experiments discussed here, the desert characteristics were applied through 300 km radius and through 700 km radius with oceanic characteristics over the balance of the 1000 km radial domain. In both cases, the diurnally varying clear air radiative + desert sensible heating was used to force the 2-dimensional model. The results indicate that the general character of the circulation remains intact. However, the horizontal scale and the intensity of the circulation pattern does show some sensitivity to the change in size of the desert and oceanic regions in the model domain.

The surface pressure traces for the 300 km and 700 km radial extent deserts are shown in Figure 5.20. For the 300 km desert, the surface pressure trace reaches its equilibrium diurnal oscillation pattern after about 30 hours. However, the minimum surface pressure on the diurnal oscillation is only 1006.40 mb, and the maximum surface pressure is about 1009.00 mb. For the 700 km desert, the surface pressure trace doesn't reach its equilibrium diurnal oscillation for 54 hours. Thereafter, the surface pressure oscillates between a minimum of 1002.50 mb and a maximum of 1006.00 mb. A much deeper
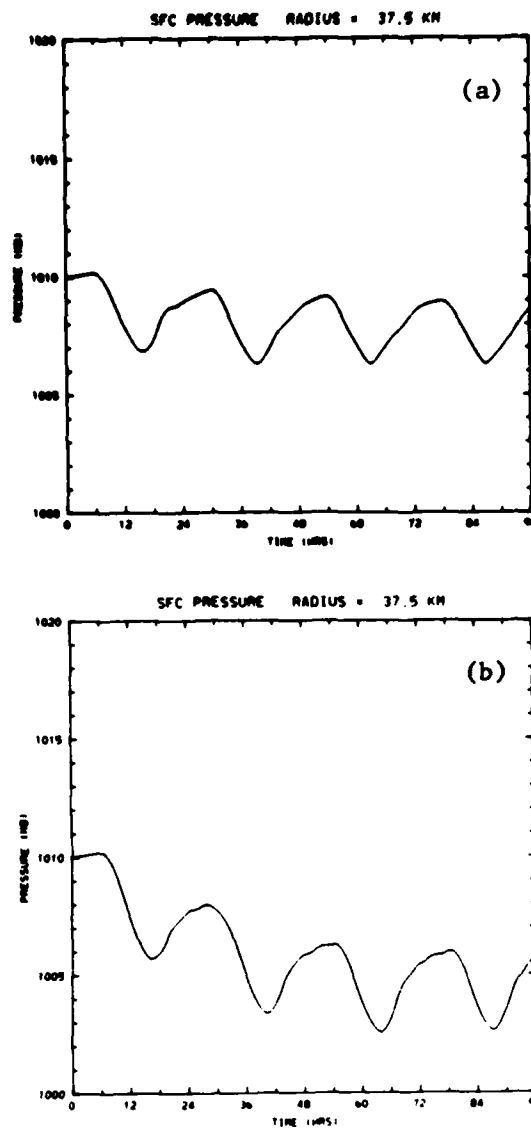
Figure 5.20 Surface pressure trace at a radius of 37.5 km
for the case of radiative + desert sensible forcing in clear
air for a 300 km (a) and a 700 km (b) desert.

"heat low" develops in the case of the 700 km desert than in the case of the 300 km desert.

Figures 5.21 and 5.22 show the radial distribution of surface pressure (a), and vertical cross-sections of tangential (b), and radial (c) wind components, and vertical motion (d) at 64 hours (1600L) for the 300 km and 700 km deserts, respectively. These figures can be compared to Figure 5.3 which depicts the same fields for the case of a 500 km desert. From these three figures, it is clear that the intensity of the late afternoon circulation is dependent on the fraction of the domain which is modelled with desert/oceanic characteristics. The 300 km desert produces the least intense circulation and the 700 km desert produces the most intense circulation. However, the general character of the circulation is unaffected by the size of the desert region. At 64 hours (1600L), all three cases are characterized by low level radial inflow in a cyclonic circulation, rising air over the desert, mid-level radial outflow in an anticyclonic circulation, and subsiding air over the ocean. It is interesting to note that the radial extent of the region of upward vertical motion closely parallels the size of the region modelled as desert. For the 300 km desert (Figure 5.21), the region of upward vertical motion extends radially to about 350 km. However, for the 500 km (Figure 5.3) and 700 km (Figure 5.22) deserts, the radial extent of the region of upward vertical motion is about 450 km and 600 km, respectively. Figures 5.21, 5.3 and 5.22 show only the instantaneous fields at 64 hours for the 300, 500, and 700 km deserts, respectively. The diurnal patterns discussed in Section 4.4 are repeated in these cases as well. The diurnal pattern exhibits a low

SFC PRESSURE 64.0 HRS

(a)

TANGENTIAL WIND 64.0 HRS (M/S)

(b)

CONTOUR INTERVAL

(b) - 1.0 m/s

(c) - 0.5 m/s

(d) - 50 mb/day

RADIAL WIND 64.0 HRS (M/S)

(c)

OMEGA 64 0 HRS (MB/DAY)

(d)
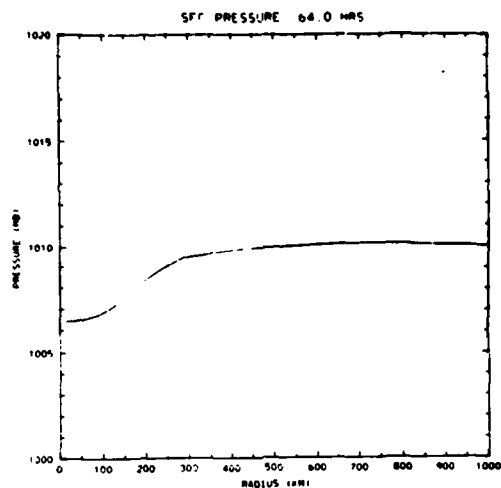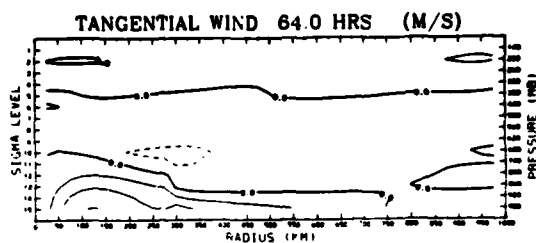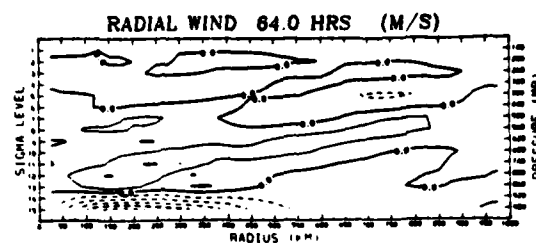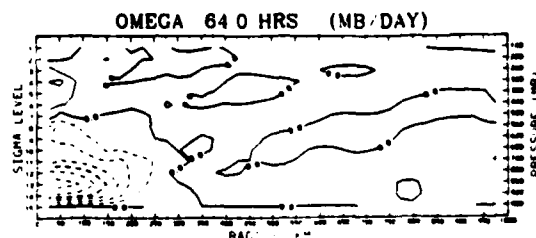
Figure 5.21 Radial distribution of surface pressure (a), and vertical cross-sections of tangential wind (b), radial wind (c), and vertical motion (d), at 64 hours for the case of radiative + desert sensible forcing in clear air for a 300 km desert.

(a)

(b)

CONTOUR INTERVAL
(b) - 1.0 m/s
(c) - 0.5 m/s
(d) - 50 mb/day

(c)

(d)
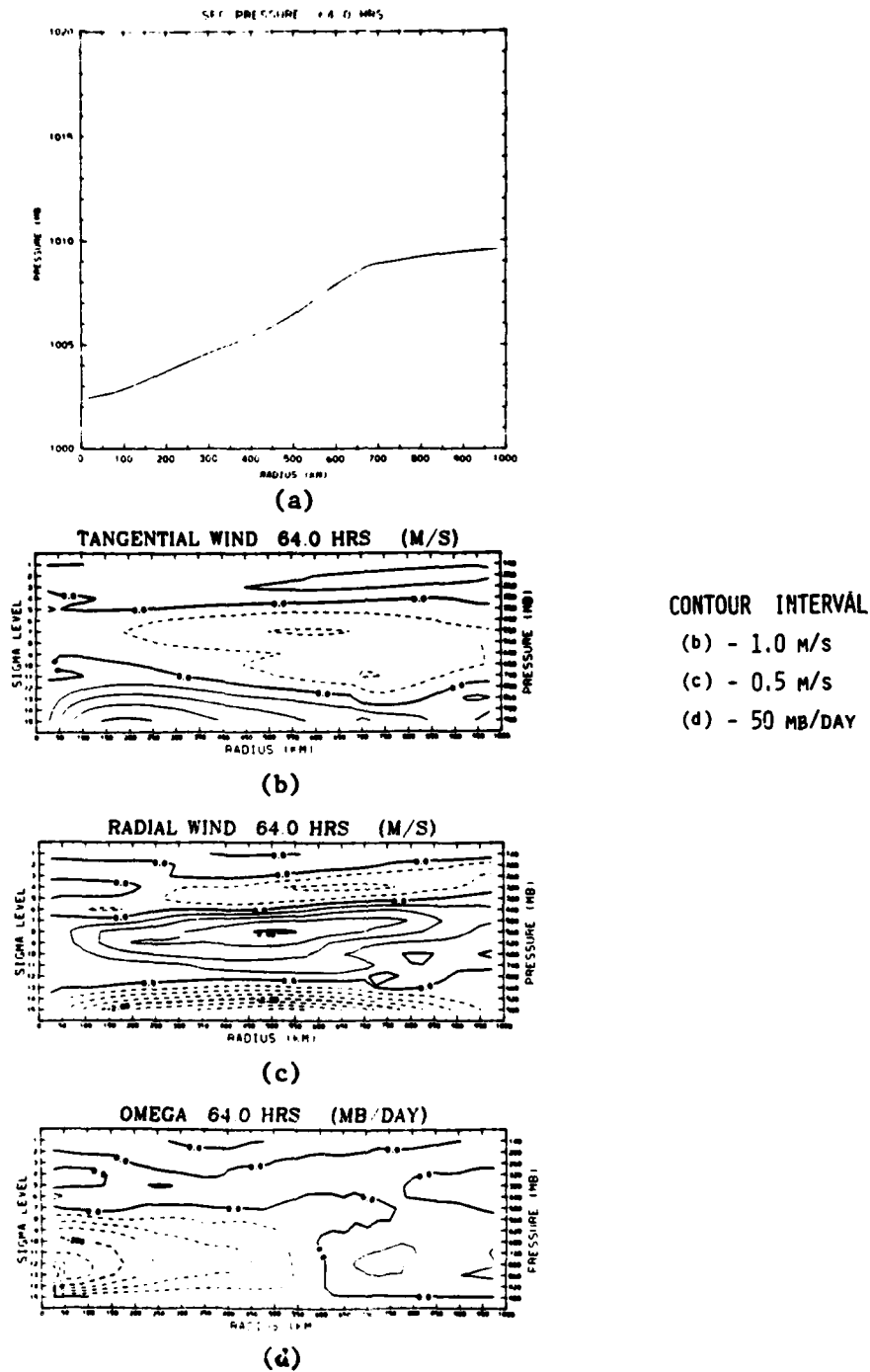
Figure 5.22 Radial distribution of surface pressure (a), and
vertical cross-sections of tangential wind (b), radial wind (c),
and vertical motion (d) at 64 hours for the case of radiative
+ desert sensible forcing in clear air for a 700 km desert.

level radial wind field which changes diurnally from inflow to outflow and outflow to inflow. While the cyclonic circulation in tangential wind persists during all hours of the day, there is a diurnal oscillation in the intensity of the circulation with the minimum intensity occurring during the late morning and the maximum intensity occurring during the period near midnight. In order to examine what impact the size of the desert region had on the timing of these circulation patterns, Table 5.2 was constructed. This table indicates for each case th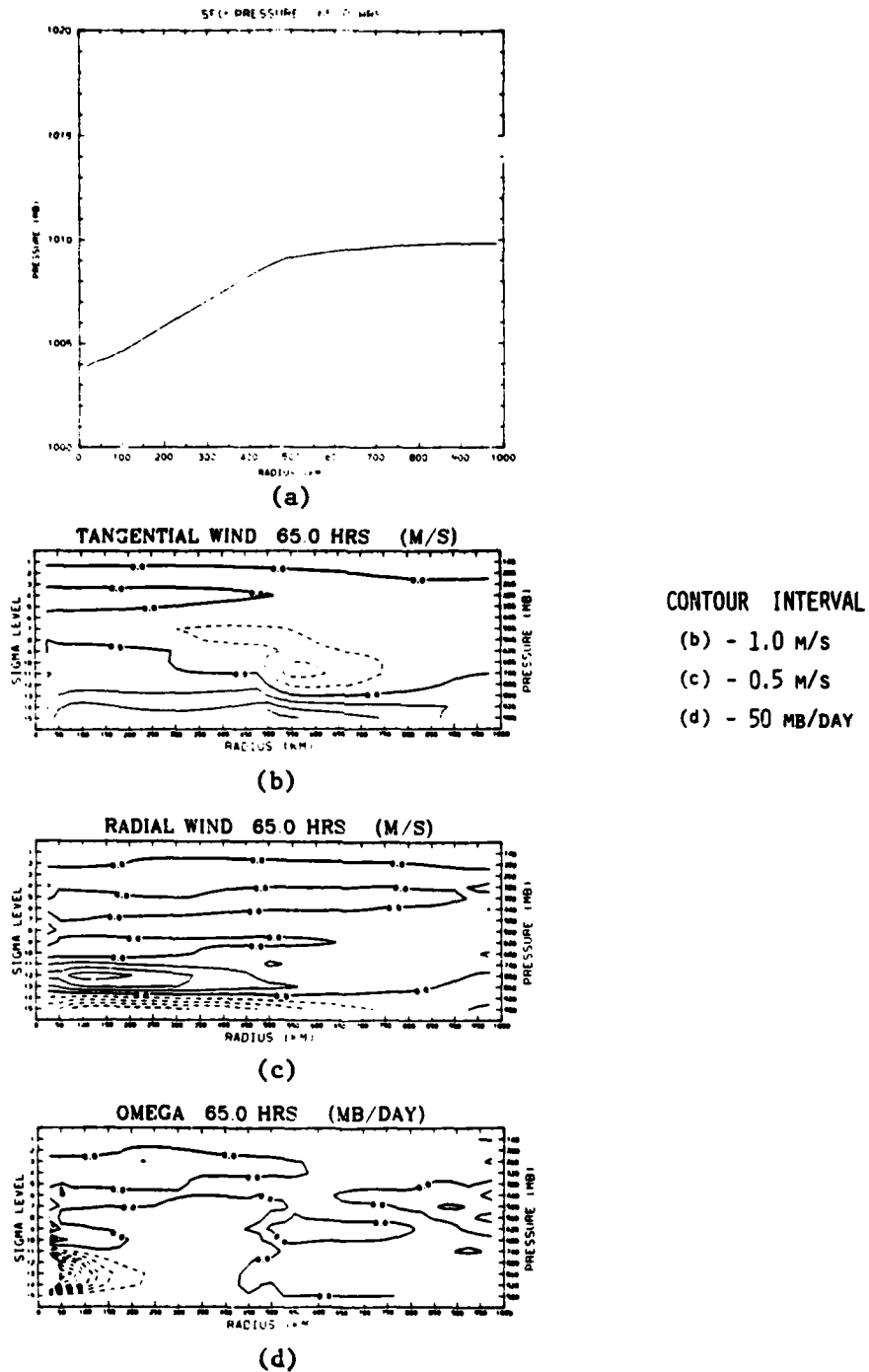e local time at which the reversals occur in the radial wind field, and the local time at which the intensity of the cyclonic circulation in the tangential wind field is a maximum and minimum. As is indicated by the table, there is some variation in the times at which these events occur depending on the size of the domain region being represented as desert. As the size of the desert increases, the reversal from radial outflow to radial inflow occurs later in the morning. Likewise, the radial inflow persists until later in the night for the case of a large desert region. In fact, in the case of the 700 km desert, the inflow persists through the entire day over the desert. However, during the hours between 0200 and 0600, the inflow is very weak and confined to the lowest layer over the desert. Just above the lowest layer, radial outflow exists during these early morning hours. In the tangential wind field, the maximum intensity occurs later in the evening for the cases of the larger deserts and the minimum intensity occurs later in the morning. These results are consistent with the radial wind field results since the radial wind contributes to the acceleration or deceleration of the tangential wind through the Coriolis term in the momentum equation.

TABLE 5.2

Local times at which reversals occur in the low level radial wind
field and local times of maximum and minimum tangential wind for the
cases of a 300, 500, and 700 km desert.

	Radial Wind Reversals Inflow-Outflow/Outflow-Inflow	Tangential Wind Intensity Maximum/Minimum
300 km Desert	0130/0630	2100/0800
500 km Desert	0230/0730	2400/1130
700 km Desert	*/Inflow weakest 0600	0100/1200

It appears that the larger desert regions cause a longer lag between the time of maximum heating and minimum surface pressure and the time of maximum intensity of the surface cyclonic circulation.

The results of these experiments indicate that while the same general pattern emerges regardless of the fraction of the model domain treated as desert or ocean, the induced circulations do show some sensitivity to the size of the desert region. In summary, the classic "heat low" circulation of low level inflow and upward motion sets up quicker in the case of a small desert region than in the case of a larger desert region. However, the circulation is more intense and more persistent in the large desert case than in the small desert case.

5.0 Summary of 2-Dimensional Experiments and Comparison with Observations

The results from all the experiments conducted with the 2-dime. iional axisymmetric primitive equation model must be interpreted very cautiously in terms of the real "heat low" circulation over the Saudi Arabian peninsula. It must be remembered that in this model, the forcing is completely determined by the horizontal gradients which were observed during a very brief series of experiments conducted in May of 1979 and June of 1981 over Saudi Arabia and the adjacent Arabian Sea. In that sense, the results should be interpreted as the circulation which would result if the only processes at work were the ones represented in this simplified 2-dimensional representation. The results include no influences from larger scale circulations which may be (and likely are) important to the local circulation over Saudi Arabia and the western Arabian Sea.

The results can best be thought of as representing a local circulation which is imposed on a large scale circulation by the strong horizontal gradients in radiative and sensible heating which exist between the desert of Saudi Arabia and the adjacent Arabian Sea. With these cautions in mind, it is then possible to draw some inferences from the results of the 2-dimensional experiments.

In all of the diurnally forced experiments, the same diurnal circulation pattern emerges. The early morning hours (~0200-0700) are characterized by low level radial outflow from the desert to the ocean and mid-level radial inflow from the ocean to the desert. The vertical motion field is one of subsidence in the low levels over the desert, and the tangential wind field is characterized by a low level cyclonic circulation which weakens during this time period. Shortly after sunrise (~0630L), the subsiding vertical motion field over the desert begins to weaken as does the low level outflow. By 1000L the strong sensible heating of the lowest level over the desert has reversed the subsidence and the vertical motion field exhibits upward vertical motion. Low level radial inflow begins from the ocean to the desert not later than 1100L with outflow from the desert to the ocean in mid-levels. It is at this time that the low level cyclonic circulation in the tangential wind field reaches its diurnal minimum intensity. The surface pressure over the desert rises during the early morning hours to its diurnal maximum between about 0630L and 0830L. The surface pressure then falls for about eight hours until it reaches its diurnal minimum near 1600L. Between the hours of 1200L and 1900L, the low level circulations intensify. The radial inflow from ocean to desert peaks at about 1900L and then begins to weaken.

In response to the radial inflow, the upward vertical motion increases in intensity until it peaks in magnitude at about 1900L. However, the depth of the layer through which upward vertical motion persists decreases after about 1600L. This is most likely a response to the shut off of the sensible heating at the desert surface. From Figure 4.2, it is apparent that between 1630 and 1730, the net radiation at the surface becomes negative. Because the sensible heating is parameterized in terms of the net radiation, the sensible heat flux becomes negative. This implies that the air near the surface begins to cool and the sensible heating which served to heat the mixed layer through the lowest 350 mb is no longer available. As a consequence, the subsidence above the layer of rising air begins to push the top of the layer downward resulting in a shallower layer of upward vertical motion. From 1900 until just after local midnight, the low level radial inflow and upward vertical motion over the desert weaken. The low level cyclonic circulation in the tangential wind field intensifies in response to the continuing but weakening radial inflow. The cyclonic circulation reaches maximum intensity near local midnight in spite of the fact that the surface pressure has been increasing since it reached its diurnal minimum at 1600L. Just after midnight, low level radial outflow begins from the desert to the ocean and the subsidence reaches down to the lowest layers of the atmosphere. The mid-level radial circulation shows inflow from the ocean to the desert and the low level cyclonic circulation in the tangential wind field begins to weaken in response to the radial outflow. The diurnal pattern is then completed.

In the experiments conducted with steady forcing equal to the net 24 hour radiative and sensible heating profiles, the steady state circulation pattern which results is similar in form to the well developed late afternoon circulation pattern from the diurnally forced case. The dynamical fields are characterized by low level and high level radial inflow from the ocean to the desert and mid-level radial outflow from the desert to the ocean. The corresponding vertical motion field shows upward vertical motion over the desert in the lower levels of the atmosphere with subsidence aloft. The tangential wind field exhibits a low level cyclonic circulation and a mid-level anticyclone in direct response to the radial wind field.

One of the original goals of this research was to try to determine what impact, if any, the elevated heat source caused by the dust which was observed in the atmosphere over Saudi Arabia and the Arabian Sea during Summer MONEX might have on the dynamics of the region. By comparing the results of the clear air experiments with the results of the dust laden experiments, it appears that the impact of the dust is reflected only in a weaker circulation. The pattern of the circulation remains unchanged from clear air to dust laden air. The primary impact of the dust is to absorb some of the shortwave radiation before it reaches the surface. Therefore, the dust reduces the net radiation at the surface and the resulting surface sensible heat flux. Since the clear air experiments produce a more intense circulation, the dust may be thought of as a moderating influence on the induced "heat low" circulation. The enhanced radiative heating above the surface by the shortwave absorption of the dust has no

appreciable impact on the overall circulation. The circulation is dominated by the surface sensible heat flux.

The dominance of the surface sensible heat flux was also shown by a comparison of the circulation induced by radiative forcing only with the circulation induced by radiative + sensible forcing. The comparison showed that the sensible heat flux from the desert surface was necessary to produce a realistic "heat low" circulation. While the desert-ocean gradient in radiative heating was capable of producing a "heat low" circulation, the circulation was much weaker than observations require. Clearly, the dominant component of the thermal forcing in producing the "heat low" circulation is the sensible heating component.

The Saudi Arabian peninsula and the adjacent Arabian Sea do not lie in a data rich portion of the world. There are relatively few observation sites for surface data and very few sites which produce regular upper air soundings. Therefore, there is no thorough data base which can be used to verify the results of this numerical effort. However, even if a thorough data base existed, it would not be reasonable to expect the results from this simple 2-dimensional representation of a very complex region to accurately reflect the "real" circulation. It is reasonable to expect only that these results represent a small scale feature which is imposed on the larger scale circulation by the land-ocean gradients which exist in this region. This modelling effort includes no influence from such things as the Hadley Cell circulation, mid-latitude system impacts, topography, the Somali Jet, or the great expanse of desert which stretches across North Africa to the west and across Iran and Pakistan

to the northeast. In spite of these shortcomings, a comparison between the model results and one data set does seem to indicate that some of the salient features of the "real" circulation pattern over Saudi Arabia and the western Arabian Sea are reflected in the model results.

Shown in Figure 5.23b, c, and d are the mean streamline and isotach analyses over the Saudi Arabian peninsula and the adjacent Arabian Sea at 12 GMT for the period 1 - 15 May 1979 at 850, 700, and 200 mb (Krishnamurti et al., 1980). These circulations were derived using data from radiosondes, rawinsondes, commercial aircraft, pilot balloons, MONEX research aircraft, ships, constant level balloons, and satellite derived cloud motion vectors. The data were analyzed daily and then averaged in time to produce these three constant pressure charts. Also, Figure 5.23a shows the surface analysis for this region on May 10, 1979 (Blake et al., 1983). While this data set is limited in that it is based on only 15 days of data in one year, it is probably representative of the circulation during May in this region. In order to compare the model results to this data set, it must be remembered that the model results are representative of the circulation produced by the 2-dimensional forcing gradients between the Arabian peninsula and the Arabian Sea. Since 12 GMT corresponds to approximately 1600L over Saudi Arabia, the model results at 1600L should be compared to the 12 GMT mean circulation.

In a general sense, the 12 GMT mean circulation indicates a low level cyclone which is characterized by radial inflow from the ocean to the desert. The surface analysis in Figure 5.23a indicates a low pressure center on the Arabian peninsula with a central pressure about
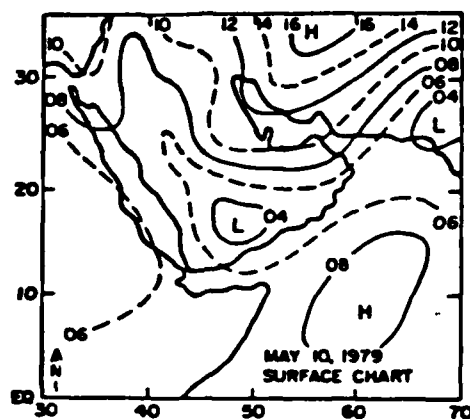
(a)

850 MB MEAN WINDS
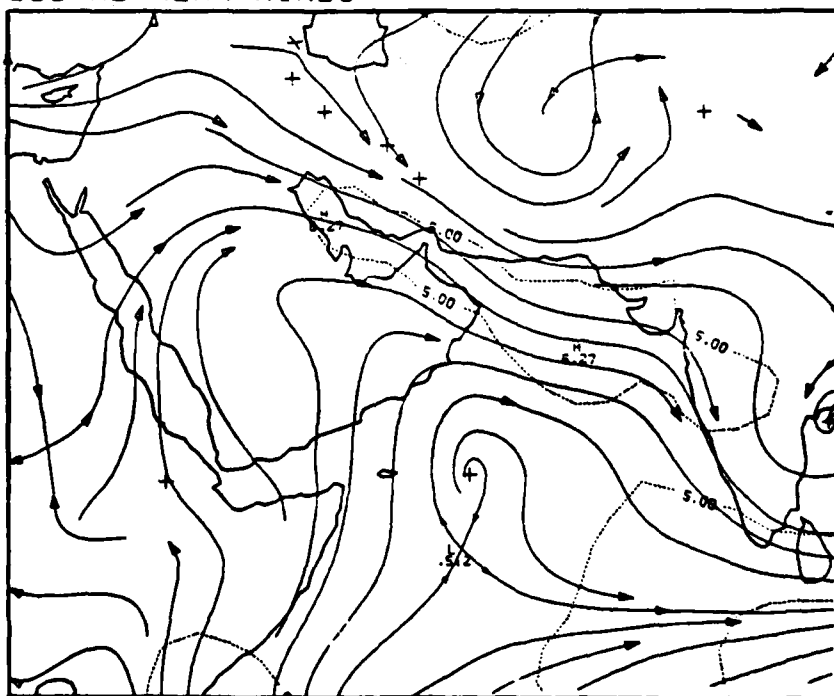
(b)

Figure 5.23 Surface pressure pattern on May 10, 1979 (a)
(from Blake et al., 1983), and 12 GMT mean streamline and
isotach analyses for 1-15 May 1979 at 850 (b), 700 (c), and
200 (d) mb (from Krishnamurti et al., 1980).

700 MB MEAN WINDS
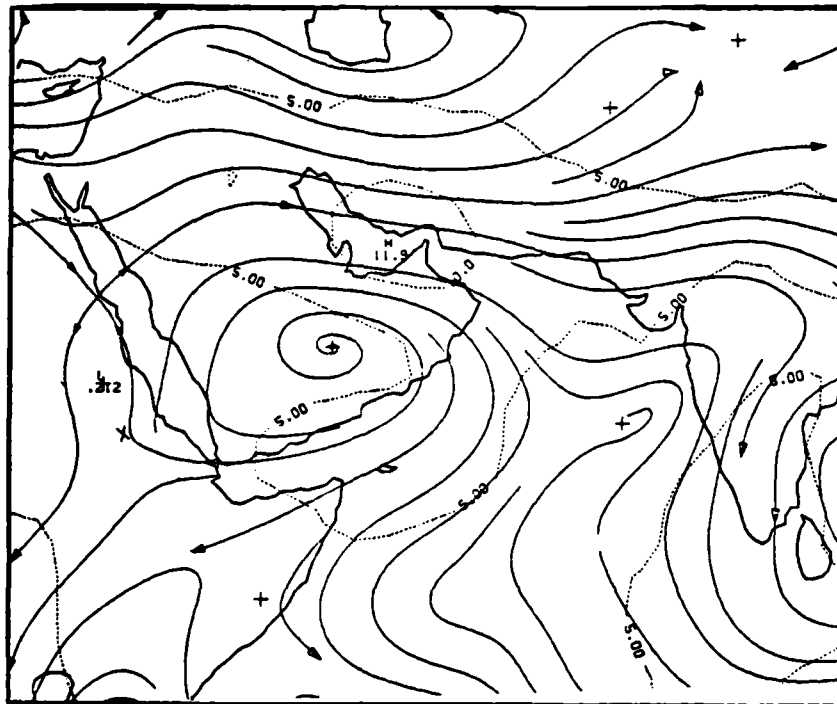
(c)

200 MB MEAN WINDS
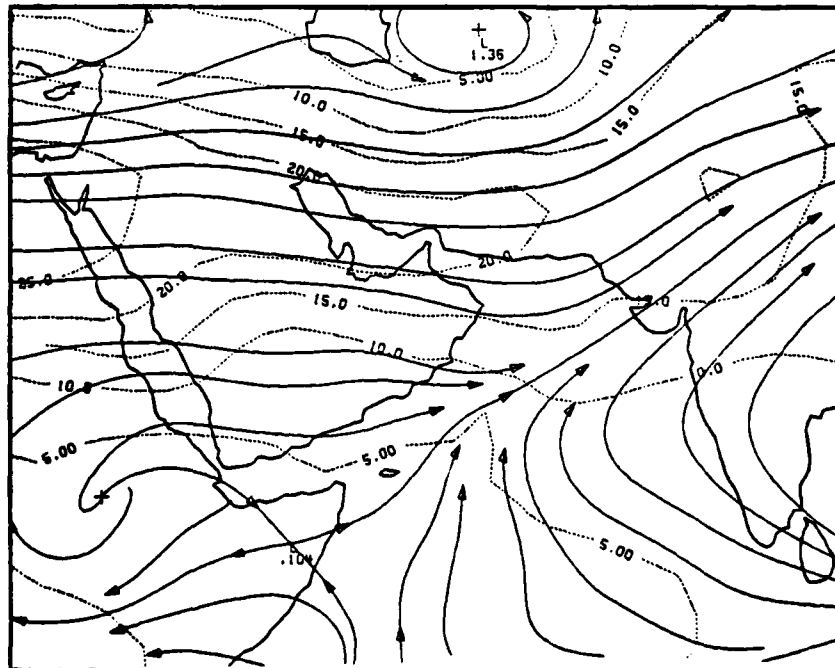
(d)

Figure 5.23   Continued.

5 mb lower than the pressure in the high pressure center over the adjacent ocean. The surface pressure pattern from the model results indicate a radial pressure gradient between 4 and 6 mb depending on which experiment is being examined. Above the surface, at 850 mb, the 12 GMT mean circulation in Figure 5.23b still contains a hint of radial inflow from the ocean to the desert. However, there is evidence that the low level cyclone is being replaced by an anticyclone at this level in the 12 GMT mean charts. The model results indicate weak inflow from the ocean to the desert at 850 mb in the radial wind field and the model maintains a weak cyclonic circulation over the desert with an anticyclone over the ocean. At 700 mb, both the 12 GMT circulation (Figure 5.23c) and the model results indicate an anticyclonic circulation established over the desert and the adjacent ocean with the radial flow field characterized by outflow from the desert to the ocean. The weak upper tropospheric circulation induced in the model results is not evident in the 12 GMT mean circulation at 200 mb. The 200 mb 12 GMT mean circulation bears more resemblance to the mid-latitude westerlies than to a circulation which is strongly influenced by a lower tropospheric "heat low". It is not possible for the 2-dimensional model to accurately reflect an influence such as mid-latitude systems because of the limitations in its very nature.

In summary, the results from the simple 2-dimensional model representation of this region do seem to reflect the nature of the middle and lower tropospheric circulation evident in the 12 GMT mean fields for early May 1979. The model produces a low level cyclonic circulation with a greater vertical extent than is evident in the 12

GMT mean charts and it fails to accurately reflect the upper tropospheric westerlies found in the 12 GMT mean charts. These two short comings are most likely related. It might be surmized that the upper tropospheric influence in this region from sources external to the model domain could serve to produce large scale convergence aloft and therefore large scale subsidence over the entire model domain which cannot be reflected in the 2-dimensional axisymmetric model results. Such a pattern would ultimately limit the vertical extent of the upward vertical motion over the desert to a shallower layer than the model results indicate. The mid-level outflow would be forced to occur lower in the atmosphere than the model results suggest. This would confine the region of radial inflow from ocean to desert to a shallower layer and therefore result in a shallower cyclonic circulation in the tangential wind field. Such a scenario in the upper levels would essentially serve as a lid on the lower tropospheric circulation which is not included in the 2-dimensional model. In spite of these shortcomings, in general, the 2-dimensional model does produce results which agree fairly well with the 12 GMT mean circulation -- at least during the late afternoon when the "heat low" is well developed.

Since the mean charts are not available for the early morning case, the quality of the diurnal pattern for the flow fields cannot be immediately verified. However, it might be guessed that external influences would be even more important during the nighttime hours because the primary energy source for the low level cyclonic circulation -- namely, the surface sensible heat flux -- is not active.

VI. 3-DIMENSIONAL BETA PLANE SPECTRAL MODEL

After the experiments with the 2-dimensional primitive equation model were completed, it was apparent that influences external to the limited model domain could be important to the "heat low" circulation. In the first step toward trying to understand the larger scale circulations, an attempt was made to model the large scale circulation which would be induced by the elongated desert region which stretches westward from Saudi Arabia across North Africa. To do this, a linearized equatorial beta plane model forced by a specified heating was employed. In this chapter, the formulation of the model and the results from the model experiments are described.

1.0 Model Description

The governing equations written in horizontal cartesian coordinates and the log-pressure vertical coordinate are as follows:

(Eastward Momentum) $\quad \dfrac{\partial u}{\partial t} + u \dfrac{\partial u}{\partial x} + v \dfrac{\partial u}{\partial y} + w \dfrac{\partial u}{\partial z} - \beta y v + \dfrac{\partial \phi}{\partial x} = 0 \quad$ (6.1.1)

(Northward Momentum) $\quad \dfrac{\partial v}{\partial t} + u \dfrac{\partial v}{\partial x} + v \dfrac{\partial v}{\partial y} + w \dfrac{\partial v}{\partial z} + \beta y u + \dfrac{\partial \phi}{\partial y} = 0 \quad$ (6.1.2)

(Hydrostatic) $\quad\quad\quad\quad\quad \dfrac{\partial \phi}{\partial z} - RT = 0 \quad\quad\quad\quad\quad\quad$ (6.1.3)

(Continuity) $\quad\quad\quad\quad \dfrac{\partial u}{\partial x} + \dfrac{\partial v}{\partial y} + \dfrac{\partial w}{\partial z} - w = 0 \quad\quad\quad$ (6.1.4)

(Thermodynamic) $\quad \dfrac{\partial T}{\partial t} + u \dfrac{\partial T}{\partial x} + v \dfrac{\partial T}{\partial y} + \left(\dfrac{\partial T}{\partial z} + \kappa T\right) w = \dfrac{\dot{Q}}{C_p} \quad$ (6.1.5)

where u is the eastward component of velocity, v is the northward component of velocity, w is the vertical log-pressure velocity, x and

y are the eastward and northward horizontal cartesian coordinates, z

is the log-pressure vertical coordinate defined by z = $\ln(P_o/P)$,

ϕ is the geopotential, T is the temperature, β is the northward

gradient of the Coriolis parameter $(\beta = \frac{\partial f}{\partial y})$, R is the gas constant

for dry air, C_p is the specific heat capacity for dry air, κ is

defined as R/C_p, and $\dot{Q}$ is the specified heat source

term. No momentum sources or sinks have been included. This system

can be linearized about a basic state of rest by defining

$$u = u'(x,y,z,t)$$

$$v = v'(x,y,z,t)$$

$$w = w'(x,y,z,t)$$

$$\phi = \bar{\phi}(z) + \phi'(x,y,z,t)$$

$$T = \bar{T}(z) + T'(x,y,z,t)$$

$$\dot{Q} = \dot{Q}'(x,y,z,t)$$

(6.1.6)

where the primed quantities are functions of (x,y,z,t) and

$\bar{\phi}(z)$ and $\bar{T}(z)$ are the basic state geopotential and

temperature distributions and are functions of z only. The linearized

system is

(Eastward Momentum) $\quad \frac{\partial u'}{\partial t} - \beta y v' + \frac{\partial \phi'}{\partial x} = 0$ (6.1.7)

(Northward Momentum) $\quad \frac{\partial v'}{\partial t} + \beta y u' + \frac{\partial \phi'}{\partial y} = 0$ (6.1.8)

(Hydrostatic) $\quad \frac{\partial \phi'}{\partial z} - RT' = 0$ (6.1.9)

(Continuity) $\quad \frac{\partial u'}{\partial x} + \frac{\partial v'}{\partial y} + \frac{\partial w'}{\partial z} - w' = 0$ (6.1.10)

(Thermodynamic) $\quad \frac{\partial T'}{\partial t} + \Gamma w' = \frac{\dot{Q}'}{C_p}$ (6.1.11)

where $\Gamma = \frac{\partial \bar{T}}{\partial z} + \kappa \bar{T}$ is the basic state static stability and is a function of the vertical coordinate z only. Eliminating T' and w' in (6.1.11) using (6.1.9) and (6.1.10), and dropping the primes as a matter of convenience yields the system (6.1.7 - 6.1.11) reduced to the following:

$$\frac{\partial u}{\partial t} - \beta yv + \frac{\partial \phi}{\partial x} = 0 \tag{6.1.12}$$

$$\frac{\partial v}{\partial t} + \beta yu + \frac{\partial \phi}{\partial y} = 0 \tag{6.1.13}$$

$$\frac{\partial}{\partial t} \{e^z \frac{\partial}{\partial z} (\frac{e^{-z}}{R\Gamma} \frac{\partial \phi}{\partial z})\} - (\frac{\partial u}{\partial x} + \frac{\partial v}{\partial y}) = e^z \frac{\partial}{\partial z} (\frac{e^{-z}\dot{Q}}{\Gamma C_p}) \tag{6.1.14}$$

The boundary condition applied at the upper boundary of the model atmosphere is that the vertical log-pressure velocity (w) be zero. At the lower surface, the actual vertical velocity must be zero. These two conditions are given by

$$\frac{\partial}{\partial t} (\frac{\partial \phi}{\partial z}) = \frac{R\dot{Q}}{C_p} \qquad \text{at } z = Z_T \tag{6.1.15}$$

$$\frac{\partial}{\partial t} (\frac{\partial \phi}{\partial z} - \frac{\Gamma \phi}{\bar{T}}) = \frac{R\dot{Q}}{C_p} \qquad \text{at } z = 0 \tag{6.1.16}$$

Following Silva Dias et al. (1983), this system is solved using transforms in all three spatial coordinates. In the vertical, an inner product of any two functions of z is defined as

$$< u,v > = \frac{1}{1 - e^{-Z_T}} \int_0^{Z_T} u(z) \, v(z) \, e^{-z} \, dz \tag{6.1.17}$$

Then, a vertical transform is defined such that

$$g_n(x,y,t) = \langle g, \Psi_n \rangle = \frac{1}{1 - e^{-Z_T}} \int_0^{Z_T} g(x,y,z,t) \, \Psi_n(z) \, e^{-z} \, dz \qquad (6.1.18)$$

where g_n represents a transformed variable and g represents the variable in physical space. The kernal $\Psi_n(z)$ is chosen so as to transform the first term of (6.1.14) in a convenient manner. If $\Psi_n(z)$ is forced to be the solution of the finite Stürm-Liouville problem given by

$$\frac{\partial}{\partial z} \left(\frac{e^{-z}}{R\Gamma} \frac{\partial \Psi_n}{\partial z} \right) + \frac{e^{-z} \Psi_n}{gh_n} = 0 \qquad (6.1.19)$$

with boundary conditions

$$\frac{\partial \Psi_n}{\partial z} = 0 \qquad \qquad \text{at } z = Z_T$$

$$\frac{\partial \Psi_n}{\partial z} - \frac{\Gamma}{\bar{T}} \Psi_n = 0 \qquad \text{at } z = 0 \qquad (6.1.20)$$

then it can be shown that the transform of the first term of (6.1.14) is given by

$$\frac{\partial}{\partial t} \left(\frac{1}{1 - e^{-Z_T}} \int_0^{Z_T} \{ e^z \frac{\partial}{\partial z} (\frac{e^{-z}}{R\Gamma} \frac{\partial \phi}{\partial z}) \} \, e^{-z} \, \Psi_n \, dz \right) =$$

$$- \frac{1}{gh_n} \frac{\partial \phi_n}{\partial t} + \frac{1}{1 - e^{-Z_T}} \left(\frac{e^{-z} \Psi_n}{R\Gamma} (\frac{R\dot{Q}}{C_p}) \right) \Big|_0^{Z_T} \qquad (6.1.21)$$

where the $\Big|_0^{Z_T}$ means the term evaluated at $z=Z_T$ minus the term evaluated at $z=0$. There exists an infinite set of eigenfunctions and eigenvalues to the Stürm-Liouville problem with the properties:

a) The eigenvalues gh_n are real and ordered;

b) The eigenfunctions Ψ_n are orthonormal in the inner product; and

c) The eigenfunctions Ψ_n form a complete set.

Therefore, because of property c, any function of z can be written

$$g(x,y,z,t) = \sum_{n=0}^{\infty} g_n(x,y,t) \ \Psi_n(z) \qquad (6.1.22)$$

which is the inverse of the vertical transform given by (6.1.18). The eigenfunctions and eigenvalues of the Stürm-Liouville problem can be determined numerically by specifying the basic state temperature profile $\overline{T}(z)$ (Fulton, 1982; Fulton and Schubert, 1984).

Assuming the heating function $\dot{Q}$ can be expressed as the product of a vertical, a horizontal, and a temporal part, it can be written

$$\dot{Q}(x,y,z,t) = V(z) \ H(x,y) \ T(t) \quad . \qquad (6.1.23)$$

Only the vertically dependent part of the heating participates in the vertical transform. Transforming the entire system given by (6.1.12) - (6.1.14) in the vertical yields

$$\frac{\partial u_n}{\partial t} - \beta y v_n + \frac{\partial \phi_n}{\partial x} = 0 \qquad (6.1.24)$$

$$\frac{\partial v_n}{\partial t} + \beta y u_n + \frac{\partial \phi_n}{\partial y} = 0 \qquad (6.1.25)$$

$$\frac{\partial \phi_n}{\partial t} + g h_n \left(\frac{\partial u_n}{\partial x} + \frac{\partial v_n}{\partial y} \right) =$$

$$g h_n \left(\frac{1}{1 - e^{-Z_T}} \left(\frac{e^{-z} \Psi_n V}{\Gamma C_p} \right) \Big|_0^{Z_T} \right.$$

$$- \left. \left(e^z \frac{\partial}{\partial z} \left(\frac{e^{-z} V}{\Gamma C_p} \right) \right)_n \right) H(x,y) \, T(t) \qquad (6.1.26)$$

where $\left(e^z \frac{\partial}{\partial z} \left(\frac{e^{-z} V}{\Gamma C_p} \right) \right)_n$ represents the vertical transform of the quantity
within parentheses. Therefore, the terms within brackets in (6.1.26)
are simply a spectral coefficient. If $V(z)$ has units $J \ kg^{-1} s^{-1}$,
then the spectral coefficient will have units of s^{-1}. By defining
a quantity V_n as

$$V_n = \left(\frac{1}{1 - e^{-Z_T}} \left(\frac{e^{-z} \Psi_n V}{\Gamma C_p} \right) \Big|_0^{Z_T} - \left(e^z \frac{\partial}{\partial z} \left(\frac{e^{-z} V}{\Gamma C_p} \right) \right)_n \right) \qquad (6.1.27)$$

(6.1.26) can be written

$$\frac{\partial \phi_n}{\partial t} + g h_n \left(\frac{\partial u_n}{\partial x} + \frac{\partial v_n}{\partial y} \right) = g h_n \, V_n \, H(x,y) \, T(t) \qquad (6.1.28)$$

where V_n is a spectral coefficient with units of inverse time, and
$H(x,y)$ and $T(t)$ are nondimensional. The system (6.1.24), (6.1.25),
and (6.1.28) has the same form as the shallow water equations with a

pure gravity wave speed given by $\sqrt{gh_n}$. A set of these equations exists for each vertical mode n.

For this application of the model, eigenfunctions and eigenvalues are computed for 19 vertical modes. Each eigenfunction is evaluated at 15 levels in the vertical corresponding to the 15 layers in the 2-dimensional primitive equation model (see Chapter 5). The basic state temperature profile used to evaluate Γ in (6.1.19) is obtained from dropwindsonde data taken over the Saudi Arabian desert (see Chapter 2). From the analyses in Chapters 3 and 4 of the radiative and sensible components of the total thermal forcing over the desert, $V(z)$--the vertical structure of the heating--is known. Therefore, knowing Γ and $V(z)$ in physical space, it is possible to compute the spectral coefficient V_n for each vertical mode n.

Next, each set of equations is non-dimensionalized by defining length and time scales by $L = \left[(gh_n)^{1/2}/\beta\right]^{1/2}$ and $T = \left[1/((gh_n)^{1/2}\beta)\right]^{1/2}$. Then, nondimensional variables are defined as

$$x^* = x/L \qquad u^* = u\,T/L$$
$$y^* = y/L \qquad v^* = v\,T/L \qquad\qquad (6.1.29)$$
$$t^* = t/T \qquad \phi^* = \phi\,T^2/L^2$$

where the superscript * implies a nondimensional variable. Using these definitions and dropping the superscripts, the system of equations can be written

$$\frac{\partial u_n}{\partial t} - y\, v_n + \frac{\partial \phi_n}{\partial x} = 0 \qquad (6.1.30)$$

$$\frac{\partial v_n}{\partial t} + y\, u_n + \frac{\partial \phi_n}{\partial y} = 0 \qquad (6.1.31)$$

$$\frac{\partial \phi_n}{\partial t} + \left(\frac{\partial u_n}{\partial x} + \frac{\partial v_n}{\partial y}\right) = V_n\, H(x,y)\, T(t) \qquad (6.1.32)$$

where it must be remembered that all variables represent nondimensional perturbations from the basic state and that a set of these nondimensional equations exists for each vertical mode n. Because a set of equations exists for each vertical mode n, each step of the process which follows must be repeated for each vertical mode.

In order to perform the horizontal transforms on this system, it is necessary to specify the horizontal dependence of the heat source $H(x,y)$. To represent the elongated desert region of North Africa and Saudi Arabia, a Guassian shape given by

$$H(x,y) = \exp\left\{ - \left(\frac{x}{a_x}\right)^2 - \left(\frac{y-y_o}{a_y}\right)^2 \right\} \qquad (6.1.33)$$

has been chosen where a_x and a_y are the nondimensional e-folding radii in the east-west and north-south directions respectively, and y_o is the nondimensional distance from the equator at which the heat source is located. With this specification of the horizontal structure of the heat source, the horizontal transforms can be performed.

In the east-west direction, a Fourier transform and inverse transform pair are defined as

$$\hat{g}(k,y,t) = \frac{1}{\sqrt{2\pi}}\int_{-\infty}^{\infty} g(x,y,t)\, e^{-ikx}\, dx \qquad (6.1.34)$$

$$g(x,y,t) = \frac{1}{\sqrt{2\pi}}\int_{-\infty}^{\infty} \hat{g}(k,y,t)\, e^{ikx}\, dk \qquad (6.1.35)$$

where k represents the wave number in the east-west direction and the $\hat{}$ symbol represents the transformed variable. Now, the east-west transform of the right hand side of (6.1.32) as can be written

$$\frac{1}{\sqrt{2\pi}}\int_{-\infty}^{\infty} V_n \exp\left\{-\left(\frac{x}{a_x}\right)^2 - \left(\frac{y-y_0}{a_y}\right)^2\right\} T(t)\, e^{-ikx}\, dx =$$

$$V_n \exp\left\{-\left(\frac{y-y_0}{a_y}\right)^2\right\} \frac{T(t)}{\sqrt{2\pi}}\int_{-\infty}^{\infty} e^{-\left(\frac{x}{a_x}\right)^2} e^{-ikx}\, dx \quad . \qquad (6.1.36)$$

Since $e^{-ikx} = \cos(kx) - i\sin(kx)$ and since $\sin(kx)$ is an even function, 6.1.36 becomes

$$\frac{1}{\sqrt{2\pi}}\int_{-\infty}^{\infty} V_n \exp\left\{-\left(\frac{x}{a_x}\right)^2 - \left(\frac{y-y_0}{a_y}\right)^2\right\} T(t)\, e^{-ikx}\, dx =$$

$$V_n \exp\left\{-\left(\frac{y-y_0}{a_y}\right)^2\right\} \frac{a_x}{\sqrt{2}} \exp\left(-\frac{k^2 a_x^2}{4}\right) T(t) \qquad (6.1.37)$$

where the fact that the integral from $-\infty$ to ∞ of an odd function is given by twice the integral from 0 to ∞ has been used. Applying the east-west transform given by (6.1.34) to (6.1.30) - (6.1.32) and using (6.1.37), the set becomes

$$\frac{\partial \hat{u}_n}{\partial t} - y \, \hat{v}_n + ik\hat{\phi}_n = 0 \qquad (6.1.38)$$

$$\frac{\partial \hat{v}_n}{\partial t} + y \, \hat{u}_n + \frac{\partial \hat{\phi}_n}{\partial y} = 0 \qquad (6.1.39)$$

$$\frac{\partial \hat{\phi}_n}{\partial t} + ik \, \hat{u}_n + \frac{\partial \hat{v}_n}{\partial y} = V_n \exp\left\{-\left(\frac{y-y_0}{a_y}\right)^2\right\} *$$

$$* \frac{a_x}{\sqrt{2}} \exp\left\{\frac{-k^2 a_x^2}{4}\right\} T(t). \qquad (6.1.40)$$

These three equations can be written in compact vector notation as

$$\frac{\partial \hat{W}_n}{\partial t} + \hat{L} \, \hat{W}_n = \hat{\tilde{W}}_n \qquad (6.1.41)$$

where

$$\hat{W}_n(k,y,t) = \begin{bmatrix} \hat{u}_n \\ \hat{v}_n \\ \hat{\phi}_n \end{bmatrix} , \qquad (6.1.42)$$

and

$$\hat{L} = \begin{bmatrix} 0 & -y & ik \\ y & 0 & \frac{\partial}{\partial y} \\ ik & \frac{\partial}{\partial y} & 0 \end{bmatrix} , \qquad (6.1.43)$$

and

$$\hat{\tilde{W}}_n(k,y,t) = \begin{bmatrix} 0 \\ 0 \\ V_n \dfrac{a_x}{\sqrt{2}} \, T(t) \, \exp\left\{-\left(\dfrac{k^2 a_x^2}{4}\right) - \left(\dfrac{y-y_0}{a_y}\right)^2\right\} \end{bmatrix} \qquad (6.1.44)$$

A generalized Hermite transform is used in the north-south direction. First, an inner product for any two complex three component vectors $\vec{f}$ and $\vec{g}$ is defined as

$$(\vec{f},\vec{g}) = \int_{-\infty}^{\infty} (f_1 \hat{g}_1^* + f_2 \hat{g}_2^* + f_3 \hat{g}_3^*) \, dy \qquad (6.1.45)$$

where the superscript $\hat{*}$ represents the complex conjugate. Then, a north-south transform and inverse transform pair can be defined as

$$W_{m,r}^n(k,t) = \left(\hat{\tilde{W}}_n(k,y,t), K_{m,r}(k,y)\right) \qquad (6.1.46)$$

$$\hat{\tilde{W}}_n(k,y,t) = \sum_{m,r} W_{m,r}^n(k,t) \, K_{m,r}(k,y) \qquad (6.1.47)$$

where $K_{m,r}(k,y)$ is a complex, three component vector kernal which satisfies

$$\hat{L} \, K_{m,r}(k,y) + i \, \nu_{m,r} \, K_{m,r}(k,y) = 0. \qquad (6.1.48)$$

Because the operator $\hat{L}$ is skew-Hermitian on the inner product (6.1.45), it can be shown that

$$(\hat{L}\,\vec{f},\vec{g}) = (\vec{f}, -\hat{L}\vec{g})\ . \tag{6.1.49}$$

The eigenvalues $(\nu_{m,r})$ and the eigenfunctions $(K_{m,r}(k,y))$ of 6.1.48 were first discussed by Matsuno (1966). The normalized eigenfunctions can be written :

For $m \geq 0$ and $k \neq 0$ when $r=0$:

$$K_{m,r}(k,y) = \begin{bmatrix} \frac{1}{2}(\nu_{m,r}-k)\ H_{m+1}(y)\ +\ m(\nu_{m,r}+k)\ H_{m-1}(y) \\[2ex] i(\nu_{m,r}^2 - k^2)\ H_m(y) \\[2ex] \frac{1}{2}(\nu_{m,r}-k)\ H_{m+1}(y)\ -\ m(\nu_{m,r}+k)\ H_{m-1}(y) \end{bmatrix} \frac{e^{-\frac{y^2}{2}}}{\sqrt{E_{m,r}\ (k)}}$$

$$\tag{6.1.50a}$$

For $m \geq 0$ and $k = r = 0$:

$$K_{m,r}(k,y) = \begin{bmatrix} -\frac{1}{2}H_{m+1}\ +\ (m+1)\ H_{m-1} \\[2ex] 0 \\[2ex] -\frac{1}{2}H_{m+1}\ -\ (m+1)\ H_{m-1} \end{bmatrix} \frac{e^{-\frac{y^2}{2}}}{\sqrt{E_{m,0}\ (0)}}$$

$$\tag{6.1.50b}$$

For $m = -1$:

$$K_{m,r}(k,y) = \begin{bmatrix} 1 \\[1ex] 0 \\[1ex] 1 \end{bmatrix} \frac{e^{-\frac{y^2}{2}}}{(2\sqrt{\pi})^{1/2}}$$

$$\tag{6.1.50c}$$

where the eigenvalues $\nu_{m,r}$ are given by the following:

For m > 0 :

$$\nu^2_{m,r} - k^2 + \frac{k}{\nu_{m,r}} = 2m + 1 \qquad r = \begin{bmatrix} 0 \\ 1 \\ 2 \end{bmatrix} \begin{matrix} \text{Rossby} \\ \text{West Gravity} \\ \text{East Gravity} \end{matrix}$$

(6.1.51a)

For m = 0 :

$$\nu_{m,r} = \begin{bmatrix} -\frac{k}{2} + [\ (\frac{k}{2})^2 + 1\ ]^{1/2} \\ -\frac{k}{2} - [\ (\frac{k}{2})^2 + 1\ ]^{1/2} \end{bmatrix} \qquad \begin{matrix} r = \begin{bmatrix} 0 \\ 1 \end{bmatrix} \begin{matrix} \text{Mixed Rossby-} \\ \text{Gravity} \end{matrix} \\ r = 2 \quad \text{East Gravity} \end{matrix}$$

where r=0 for $k \geq 2^{-\frac{1}{2}}$ and r=1 for $k \leq 2^{-\frac{1}{2}}$ (6.1.51b)

For m = -1 :

$$\nu_{m,r} = -k \qquad\qquad r = 2 \quad \text{Kelvin} \ .$$

(6.1.51c)

In the above expressions, the normalization factor E is given by the following:

For m ≥ 0 and k ≠ 0 when r = 0 :

$$E_{m,r}(k) = 2^m\ m!\ \sqrt{\pi}\ [(m+1)\ (\nu_{m,r}-k)^2 + m(\nu_{m,r} + k)^2 + (\nu^2_{m,r} - k^2)^2]$$

(6.1.52a)

and for m ≥ 0 and k = r = 0 :

$$E_{m,0}(0) = 2^m\ (m-1)!\ \sqrt{\pi}\ (m+1)\ (2m+1)$$

(6.1.52b)

and $H_m(y)$ is the mth order Hermite polynomial evaluated at y.

Transforming the set of equations given by (6.1.41) using
(6.1.46) yields

$$\left(\frac{\partial \hat{W}_n}{\partial t}, K_{m,r}(k,y)\right) + \left(\hat{L}\hat{W}_n, K_{m,r}(k,y)\right) = \left(\hat{\tilde{W}}_n, K_{m,r}(k,y)\right). \quad (6.1.53)$$

The first term is simply the time derivative of the quantity $W^n_{m,r}(k,t)$
defined by (6.1.46). The second term, after using (6.1.49) and (6.1.48),
can be written $\left(\hat{W}_n, -i\nu_{m,r} K_{m,r}(k,y)\right)$. Finally, after taking $i\nu_{m,r}$
outside the inner product and applying (6.1.46), the second term
becomes $-i\nu_{m,r} W^n_{m,r}(k,t)$. The term on the right hand side of (6.1.53)
is more complex to evaluate. It can be written

$$\int_{-\infty}^{\infty} \left[{}^1\hat{\tilde{W}}_n(k,y,t) \; {}^1\hat{K}^*_{m,r}(k,y) + {}^2\hat{\tilde{W}}_n(k,y,t) \; {}^2\hat{K}^*_{m,r}(k,y) \right.$$

$$\left. + {}^3\hat{\tilde{W}}_n(k,y,t) \; {}^3\hat{K}^*_{m,r}(k,y) \right] dy \quad (6.1.54)$$

where the superscripts on the upper left indicate components, and the
superscript $\hat{*}$ represents the complex conjugate. It is apparent
that since $K_{m,r}(k,y)$ takes on various forms depending on the values
of m,k, and r, so will this integral. In general, the integral defined
by (6.1.54) can be written as $\hat{\tilde{W}}^n_{m,r}(k)T(t)$ where it can be shown that
$\hat{\tilde{W}}^n_{m,r}(k)$ is given as follows:

For $m \gtrless 0$ and $k \neq 0$ when $r = 0$:

$$\hat{\tilde{W}}^n_{m,r}(k) = \sqrt{2\pi} \, V_n \, \frac{a_x a_y}{(4+2a_y^2)^{\frac{1}{2}}} \, \exp\left(\frac{-y_0^2}{2+a_y^2}\right) *$$

$$* \frac{1}{\sqrt{E_{m,r}(k)}} \exp\left(\frac{-k^2 a_x^2}{4}\right) \{\tfrac{1}{2}(\nu_{m,r}-k)B_{m+1} - m(\nu_{m,r}+k)B_{m-1}\} \quad (6.1.55a)$$

For $m \geq 0$ and $k = r = 0$:

$$\hat{\tilde{W}}^n_{m,r}(k) = \sqrt{2\pi} \, V_n \, \frac{a_x a_y}{(4+2a_y^2)^{\frac{1}{2}}} \, \exp\left(\frac{-y_0^2}{2+a_y^2}\right) *$$

$$* \frac{1}{\sqrt{E_{m,0}(0)}} \{-\tfrac{1}{2} B_{m+1} - (m+1) B_{m-1}\} \quad (6.1.55b)$$

For $m = -1$ and $r = 2$:

$$\hat{\tilde{W}}^n_{m,r}(k) = \sqrt{2\pi} \, V_n \, \frac{a_x a_y}{(4+2a_y^2)^{\frac{1}{2}}} \, \exp\left(\frac{-y_0^2}{2+a_y^2}\right) *$$

$$* \frac{1}{(2\sqrt{\pi})^{\frac{1}{2}}} \exp\left(\frac{-k^2 a_x^2}{4}\right) B_0 \quad (6.1.55c)$$

with

$$B_m = \frac{(2-a_y^2)}{(2+a_y^2)} H_m\left(\frac{2y_0}{(4-a_y^4)^{\frac{1}{2}}}\right) \qquad a_y \neq \sqrt{2} \quad (6.1.56a)$$

and

$$B_m = y_0^m \qquad a_y = \sqrt{2} \quad . \quad (6.1.56b)$$

Then (6.1.53) can be written

$$\frac{dW_{m,r}^{n}(k,t)}{dt} - i \, \nu_{m,r} \, W_{m,r}^{n}(k,t) = \hat{\tilde{W}}_{m,r}^{n}(k) \, T(t). \qquad (6.1.57)$$

Once the temporal part of the heating $T(t)$ is specified, then (6.1.57) can be solved for $W_{m,r}^{n}(k,t)$. It should again be noted that a solution for $W_{m,r}^{n}(k,t)$ exists for each vertical mode n.

The total process to obtain the solution to this problem for a specified forcing is given as follows:

1. Compute the vertical structure functions $\Psi_{n}(z)$ and phase speeds gh_{n} for each vertical mode n based on a specified $\bar{T}(z)$.

2. In dimensional physical space, define the constants for the problem such as:

   a. Size of the domain over which results are desired.

   b. Locations of grid points where output is desired.

   c. E-folding radii a_{x} and a_{y}.

   d. Distance of the heat source from the equator y_{o}.

   e. Time at which the results are desired.

3. For each vertical mode n, compute the length and time scaling factors L, T.

4. Nondimensionalize all quantities in step 2 for each vertical mode n.

5. Use these nondimensional quantities to compute $W_{m,r}^{n}(k,t)$ by solving (6.1.57) for each vertical mode n.

6. Use (6.1.47) to invert the north-south transform to determine $\tilde{W}_n(k,y,t)$ at each y grid location in nondimensional space for each vertical mode n.

7. Use (6.1.35) to invert the east-west transform to determine $u_n(x,y,t)$, $v_n(x,y,t)$, $\phi_n(x,y,t)$ at each x,y grid location in nondimensional space for each vertical mode n.

8. Dimensionalize these results by multiplying u_n and v_n by $L/T = \sqrt{gh_n}$ and multiplying ϕ_n by $L^2/T^2 = gh_n$ at each x, y grid location for each vertical mode n.

9. Use (6.1.22) to invert the z transform and to obtain u, v, and ϕ at each desired level in the vertical at each x, y grid location in dimensional physical space.

If the temporal part of the forcing T(t) is specified in a reasonable manner, (6.1.57) can be solved analytically. Two choices for T(t) were used in this study. In the first case, the vertical structure of the heating V(z) was defined to be the vertical profile of the net 24 hour thermal forcing for a clear atmopshere over the desert. The vertical profile for the net 24 hour thermal forcing is shown in Figure 6.1. For this vertical heating structure, a temporal forcing component given by T(t)=1 was specified. That is, in the model it was assumed that the net 24 hour thermal forcing was applied as a constant and unchanging forcing. In this case, the solution to (6.1.57) was found to be

$$W^n_{m,r}(k,t) = \frac{\exp(i\,\nu_{m,r}t)-1}{i\,\nu_{m,r}} \,\hat{\tilde{W}}^n_{m,r}(k) \quad . \tag{6.1.58}$$
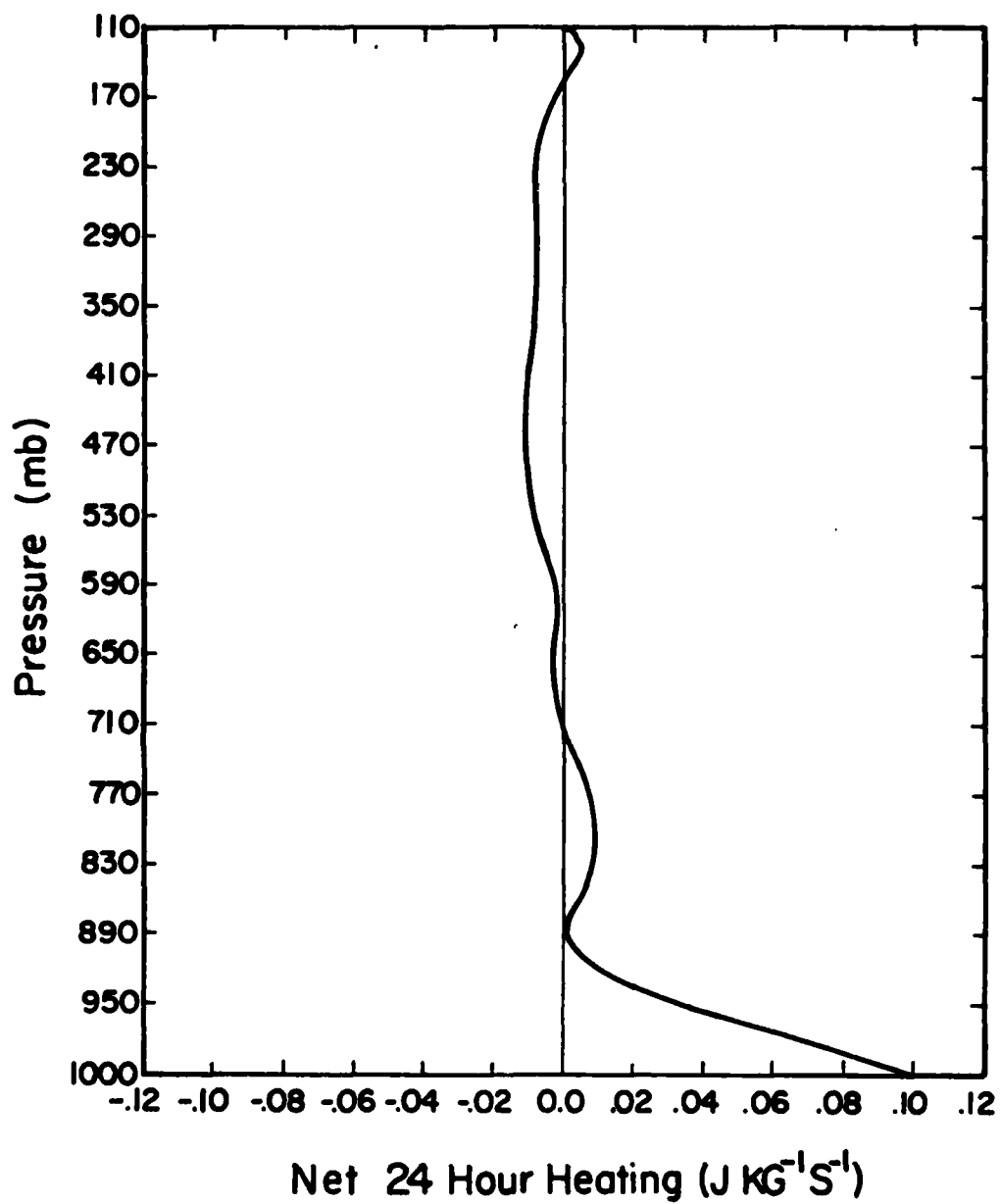
Figure 6.1 Vertical profile of the net 24 hour heating for clear air over the desert which was used as the case 1 thermal forcing for the 3-dimensional model.

For the second case, the vertical structure of the heating $V(z)$ was defined to be the vertical profile of the thermal forcing for a clear atmosphere over the desert at about 1515L. 1515L represents a mid-afternoon case over the hot desert surface when the mixed layer is nearly fully developed and the surface sensible heat flux is large. The vertical profile for the second case is shown in Figure 6.2. For the 1515L vertical heating structure, a temporal forcing component given by $T(t)=0.5 + \cos(\omega t)$ was chosen with $\omega = 7.2722 \times 10^{-5} s^{-1}$. This temporal forcing implies that the heating varies diurnally with a frequency equal to one complete cycle in 24 hours. The 0.5 offset factor in the cosine curve causes the heating to be positive for a longer period during a 24 hour cycle than it is negative. That is, there is more heating than cooling during a 24 hour cycle. The temporal forcing component is shown in Figure 6.3. For this case, the solution to (6.1.57) was found to be

$$W^n_{m,r}(k,t) = \left\{ \frac{0.5 \left(\exp(i\, \nu_{m,r} t) - 1 \right)}{i\, \nu_{m,r}} + \frac{i\, \nu_{m,r}}{\omega^2 - \nu^2_{m,r}} \exp(i\, \nu_{m,r} t) \right.$$

$$\left. + \frac{1}{\omega^2 - \nu^2_{m,r}} \left(\omega \sin(\omega t) - i\, \nu_{m,r} \cos(\omega t) \right) \right\} \hat{\tilde{W}}^n_{m,r}(k) \ . \quad (6.1.59)$$

Care must be taken in both cases when $\nu_{m,r}$ has the value 0 because $\nu_{m,r}$ appears in the denominator of the solutions and in both cases $\nu_{m,r} = 0$ results in an indeterminate form of $0/0$ for $W^n_{m,r}(k,t)$. By applying L'Hopital's Rule, the solutions can be evaluated as $\nu_{m,r} \to 0$. In case 1 $\left(T(t) = 1 \right)$,
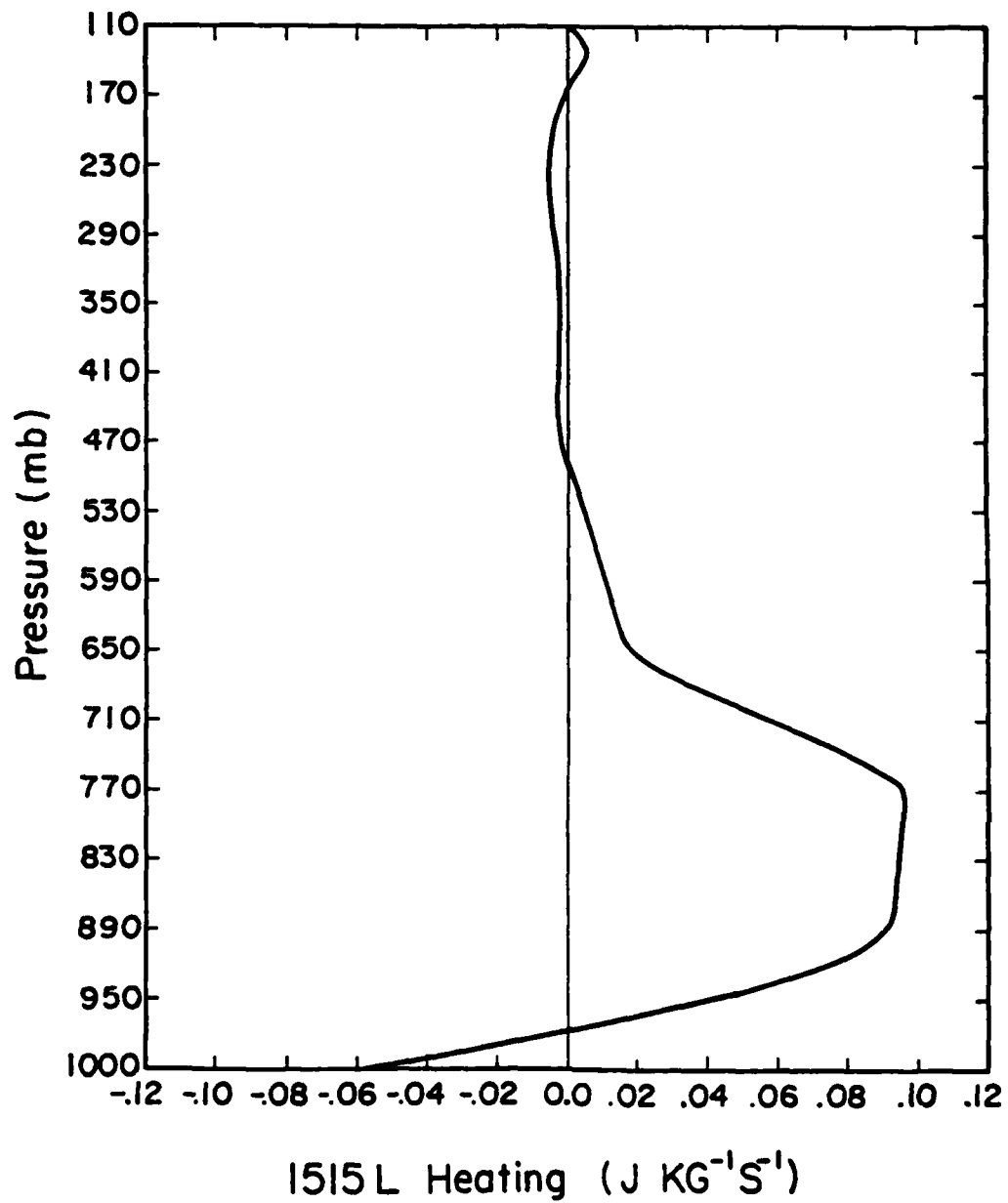
Figure 6.2 Vertical profile of the 1515L heating for clear
air over the desert which was used as the case 2 thermal
forcing for the 3-dimensional model.

2.0
1.5
1.0
0.5
0
-0.5
-1.0
-1.5
-2.0

6 12 18 24 30 36   t (hr)
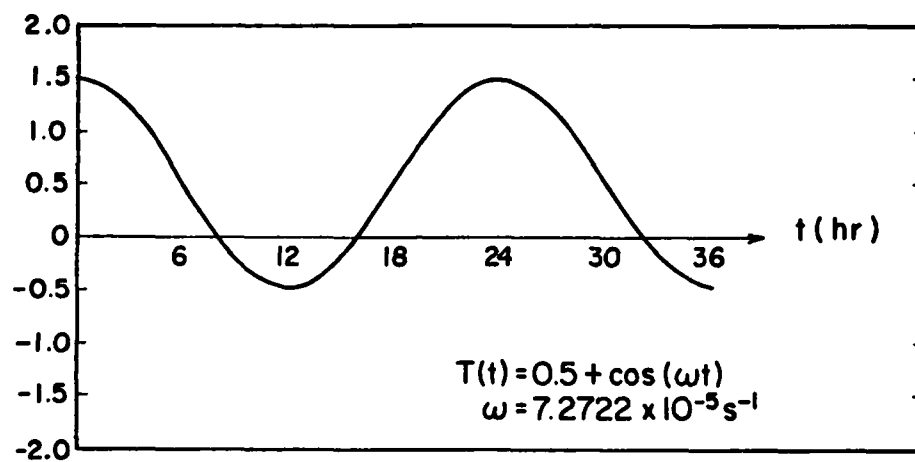
$T(t) = 0.5 + \cos(\omega t)$
$\omega = 7.2722 \times 10^{-5} s^{-1}$

Figure 6.3 Specified temporal variation of the case 2 1515L
thermal forcing for the 3-dimensional model.

$$\lim_{\substack{\nu_{m,r} \neq 0}} W^n_{m,r}(k,t) = t \, \hat{\tilde{W}}^n_{m,r}(k) \tag{6.1.60}$$

and for case 2 $\bigl(T(t)=0.5 + \cos(\omega t)\bigr)$,

$$\lim_{\substack{\nu_{m,r} \neq 0}} W^n_{m,r}(k,t) = \left[\, 0.5t + \left(\frac{\sin(\omega t)}{\omega}\right) \, \right] \hat{\tilde{W}}^n_{m,r}(k) \quad . \tag{6.1.61}$$

The results from these two cases are presented in Sections 3 and 4 below.

2.0 Specification of the Horizontal Structure H(x,y) and the Output Domain

As was stated in the previous section, the horizontal structure of the heat source was represented by a Guassian shape defined as

$$H(x,y) = \exp \left\{ \, - \left(\frac{x}{a_x}\right)^2 - \left(\frac{y-y_0}{a_y}\right)^2 \right\} \tag{6.2.1}$$

where a_x and a_y are the e-folding radii in the east-west and north-south directions respectively, and y_0 is the distance from the equator at which the heat source is located. The magnitudes of a_x, a_y, and y_0 were chosen to approximately represent the desert region of North Africa.

Shown in Figure 6.4 is a map which illustrates the region which was described as the heat source. The dashed rectangular box encompasses 1 e-folding radius in both the east-west and north-south directions. The center of the heat source is shown by an "x" in Figure 6.4. The heat source was centered at 18°N latitude which forced the parameter y_0 to have the value 2001.60 km. The
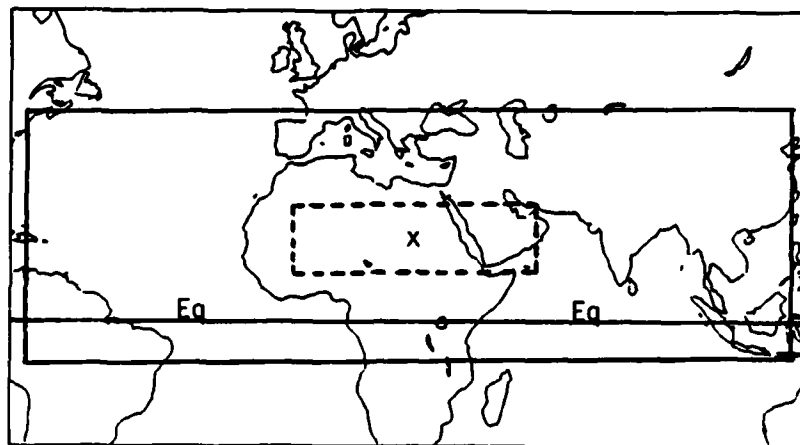
Figure 6.4   Illustration of the region which was specified
as a heat source (dashed line) and the output domain
(solid heavy line) for the experiments with the 3-dimensional
model.

e-folding radii were given the values a_x = 3172.08 km and a_y = 834.00 km, which imply a heat source that extends about $\pm 30°$ in longitude and $\pm 7.5°$ in latitude. With this specification of the horizontal structure parameters, Saudi Arabia lies on the extreme eastern edge of the heat source region. In all the experiments conducted with this model, the horizontal structure of the heat source was specified exactly as it is described here.

Also shown in Figure 6.4 is the domain over which the numerical results were computed. The solid rectangular box which extends from 70° W – 120° E and from 10° S – 45° N describes the output domain. Within this output domain, gridpoints were located every 100 km in both the north-south and east-west directions. This gridpoint spacing required 201 points in the east-west direction and 61 points in the north-south direction for a total of 12,261 gridpoints. All the results shown in the next section are for this output domain.

3.0 Model Results

The results of the experiments conducted with the 3-dimensional equatorial beta plane spectral model were disappointing at best. While it was hoped that some insight would be gained into the impact which the desert region of North Africa might have on the local Saudi Arabian circulation, the results from these numerical experiments were somewhat inconclusive. In this section, the results from the experiments for two specifications of the vertical and temporal structure of the heating are discussed. Then, the results from the two experiments are compared.

3.1 Net 24 Hour Constant Forcing

In the first experiment, the model atmosphere was forced with a heat source which was constant in time. The vertical structure of the heat source for this experiment was specified as the vertical structure of the 24 hour net radiative and sensible heating over a clear desert which was used in the experiments with the 2-dimensional, axisymmetric, primitive equation model described in Chapter 5. This vertical structure is illustrated in Figure 6.1. The resulting perturbation geopotential and velocity fields at 48 hours for 140, 380, 680, and 980 mb are shown in Figure 6.5a-d. The border label units are km with (0,0) being the center of the heat source. The contours are isopleths of perturbation geopotential (m^2s^{-2}) and the vectors represent perturbation velocity ($m\ s^{-1}$). In the following discussion only the region near the center of the output domain will be considered.

The vertical structure of the flow field induced in this experiment shows a pattern similar to the results from the locally induced 2-dimensional circulation over Saudi Arabia. The lower atmosphere (980 mb) is characterized by a cyclonic circulation with a minimum geopotential perturbation of -24 m^2s^{-2} near the center of the heat source. In the middle troposphere (680 mb), the cyclonic circulation has been replaced by an anticyclonic pattern characterized by a geopotential perturbation of +42 m^2s^{-2}. This pattern again reverses in the vertical so that the upper troposphere (380 mb, 140 mb) exhibits a cyclonic circulation pattern. At all levels in the vertical, the geopotential contours reflect the east-west elongation specified in the Guassian shape of the horizontal structure. While

140 MB AT 48.0 HRS

380 MB AT 48.0 HRS

680 MB AT 48.0 HRS

980 MB AT 48.0 HRS
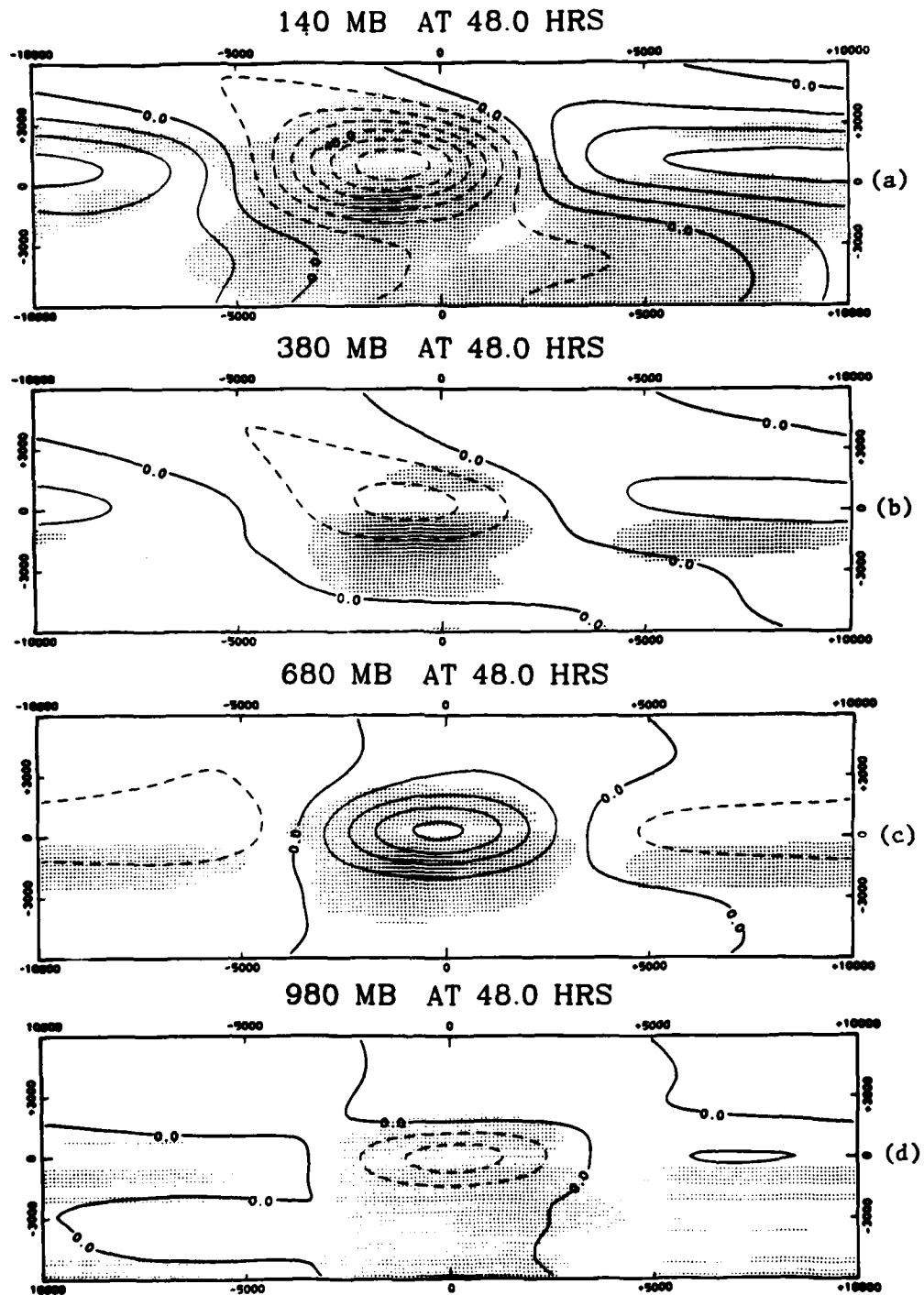
Figure 6.5 Geopotential and velocity distributions induced at 48 hours by the net 24 hour constant thermal forcing at 140 (a), 380 (b), 680 (c), and 980 (d) mb. Border labels are in units of km. Geopotential contour interval is 10 m^2s^{-2} and only velocities greater than 0.25 m s^{-1} are shown.

the maximum wind speeds occur equatorward of the center of the heat source at all levels, the winds at 48 hours are very light.

As for the temporal variation, the wind speeds at 48 hours are about twice as large as the wind speeds at 24 hours. This increase in energy is due to the undissipated constant thermal forcing specified in this experiment. Other than this change in magnitude, the fields at 48 hours are essentially unchanged from those at 24 hours.

3.2 1515L Diurnally Varying Forcing

In this experiment, the model atmosphere was forced with a heat source whose temporal structure was a cosine function with a frequency specified so that one heating cycle was completed each 24 hours. The amplitude of the cosine function was made asymetric about 0 by adding a constant offset factor of 0.5. This offset factor was specified so that the net forcing over a 24 hour cycle was positive and not zero. This temporal structure is shown in Figure 6.3. The vertical structure of the heat source was specified as the vertical structure of the total radiative and sensible heating over a clear desert at 1515L. This vertical structure is shown in Figure 6.2. The resulting perturbation geopotential and velocity fields at 24, 36, and 48 hours for 140, 380, 680, and 980 mb are shown in Figures 6.6a-d, 6.7a-d, and 6.8a-d, respectively. As in Figure 6.5, the border label units are km, the contours represent isopleths of perturbation geopotential (m^2s^{-2}), and the vectors represent perturbation velocity $(m\ s^{-1})$.

In the resulting geopotential perturbation field, at all hours, there is a tendency for the field to split into regions of positive and negative perturbations with the division occurring along a north-south line near the center of the heat source. This tendency is

153

140 MB   AT 24.0 HRS

(a)

380 MB   AT 24.0 HRS

(b)

680 MB   AT 24.0 HRS

(c)

980 MB   AT 24.0 HRS

(d)
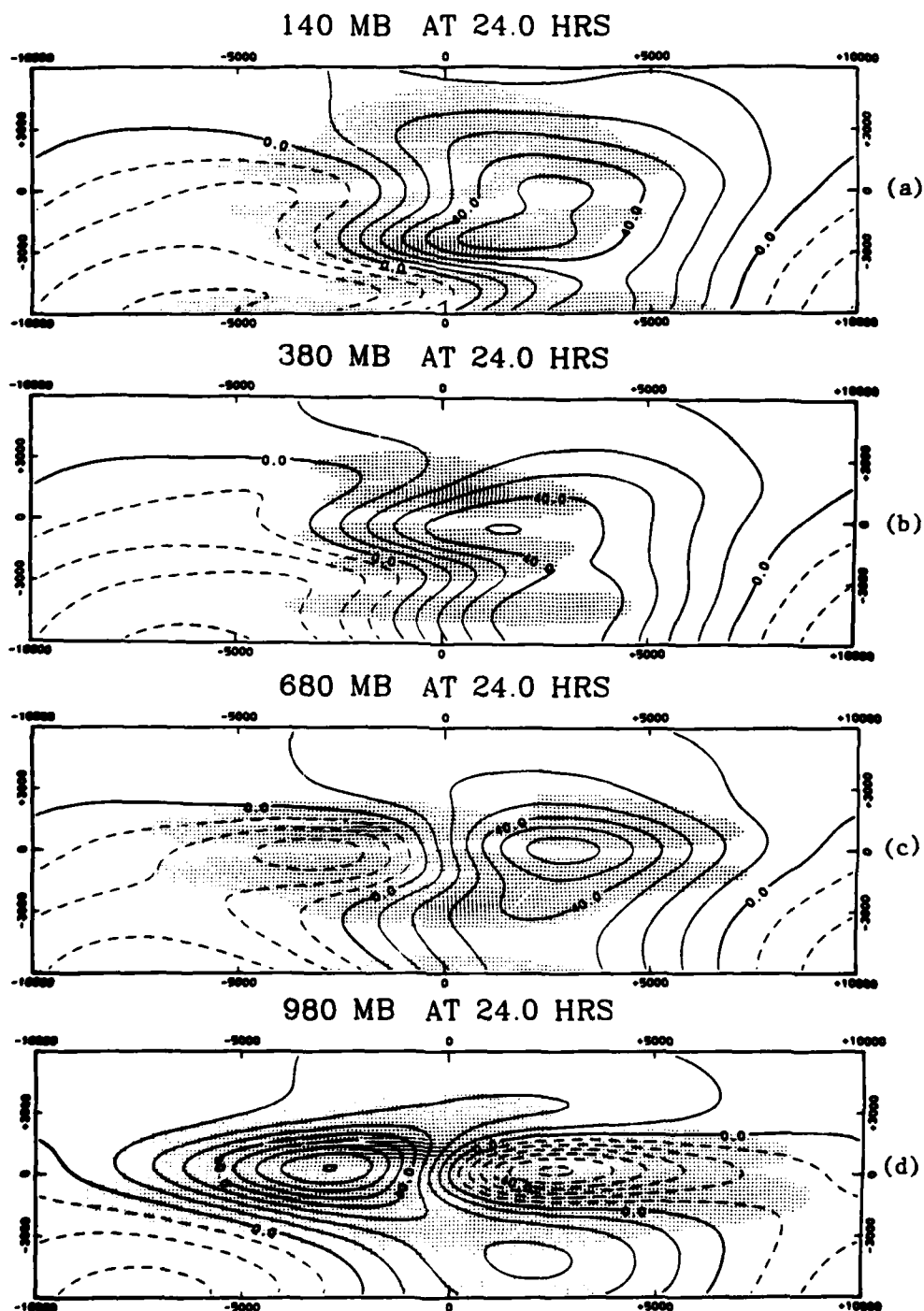
Figure 6.6 Geopotential and velocity distributions induced at 24
hours by the 1515L diurnal thermal forcing at 140 (a), 380 (b),
680 (c), and 980 (d) mb. Border labels are in units of km.
Geopotential contour interval is 10 m^2s^{-2} and only velocities
greater than 0.25 m s^{-1} are shown.

154

140 MB   AT 36.0 HRS

(a)

380 MB   AT 36.0 HRS

(b)

680 MB   AT 36.0 HRS

(c)

980 MB   AT 36.0 HRS

(d)
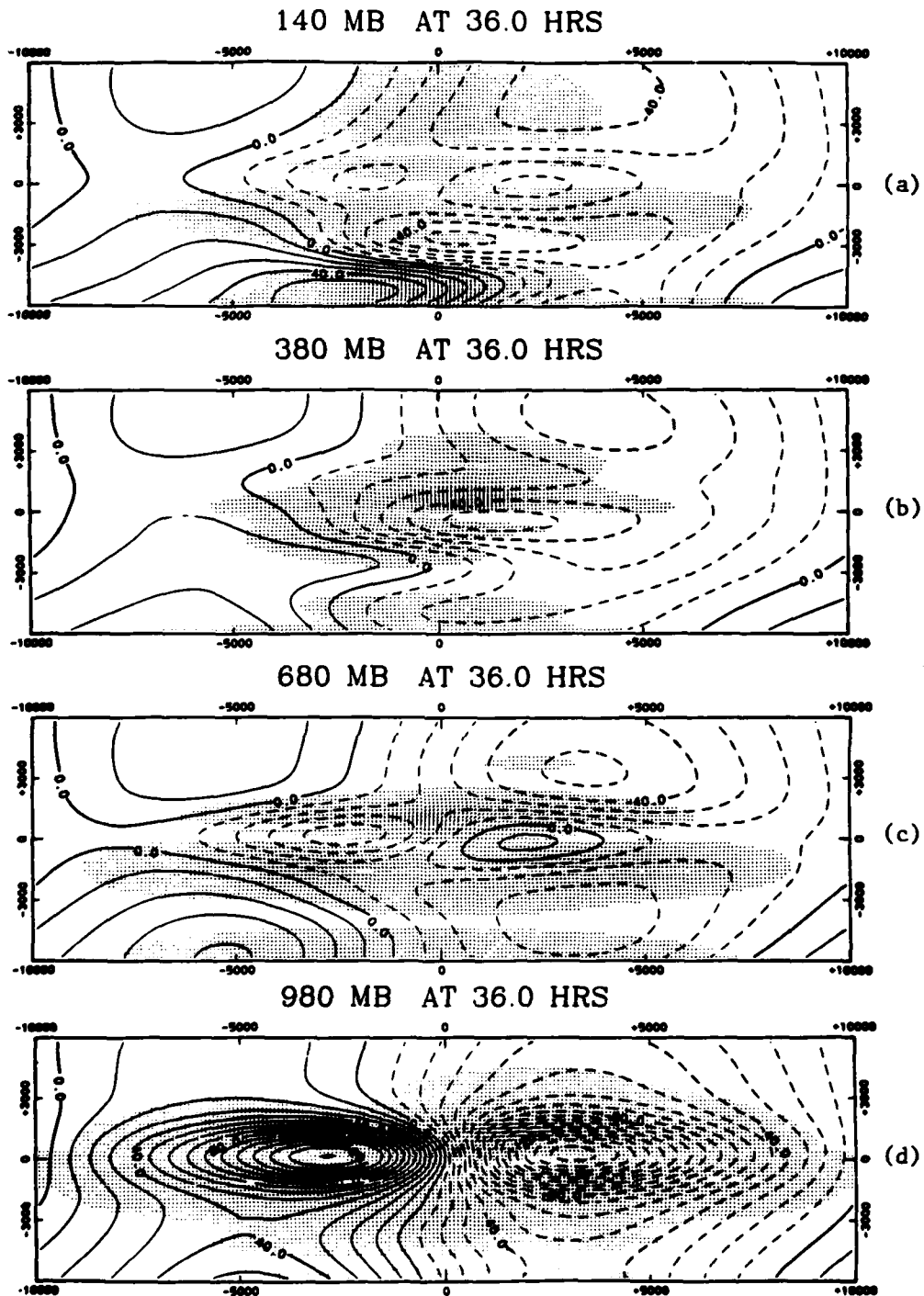
Figure 6.7   Geopotential and velocity distributions induced at 36 hours by the 1515L diurnal thermal forcing at 140 (a), 380 (b), 680 (c), and 980 (d) mb.   Border labels are in units of km. Geopotential contour interval is 10 m^2s^{-2} and only velocities greater than 0.25 $m\ s^{-1}$ are shown.

140 MB   AT 48.0 HRS

(a)

380 MB   AT 48.0 HRS

(b)

680 MB   AT 48.0 HRS

(c)

980 MB   AT 48.0 HRS

(d)
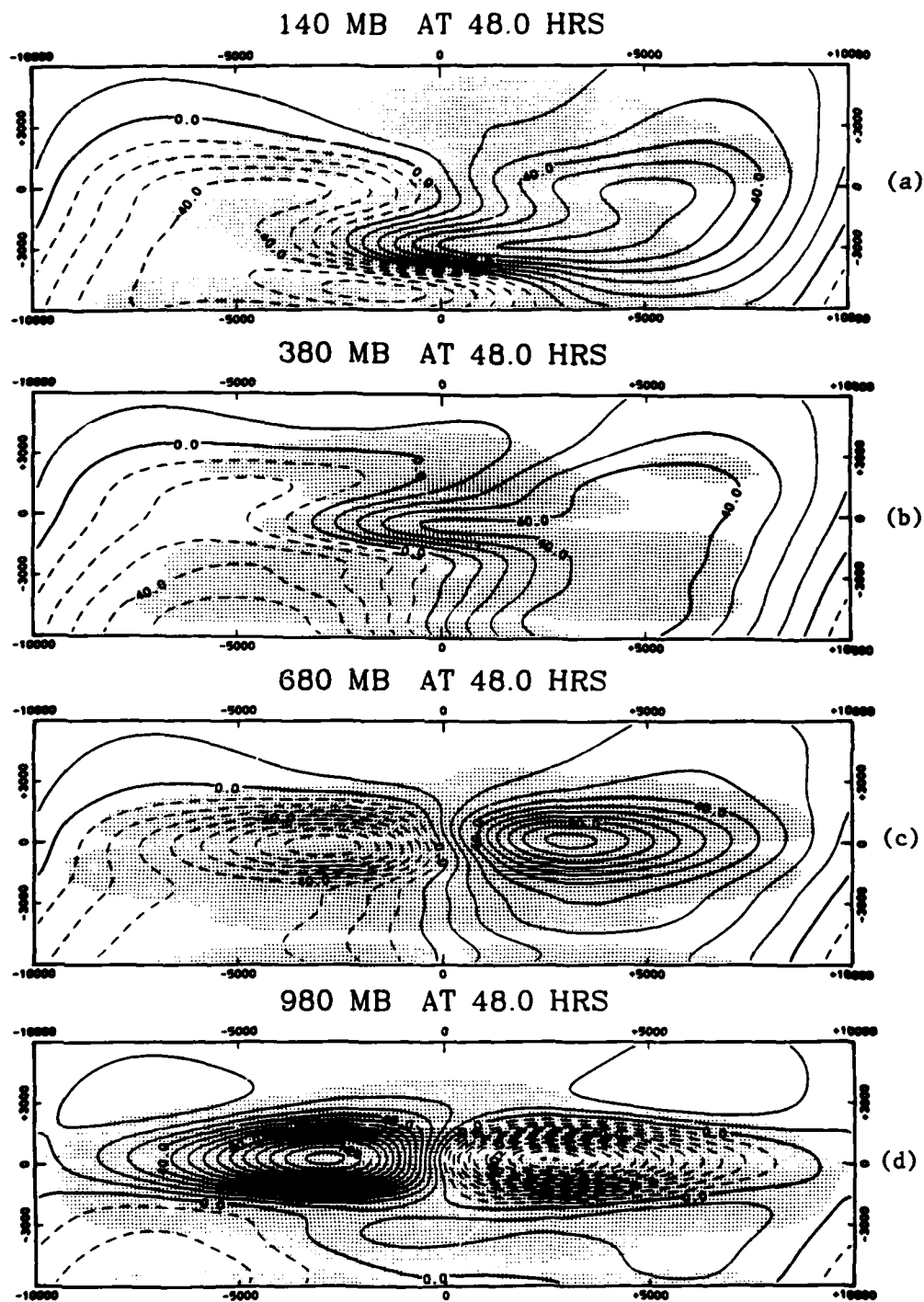
Figure 6.8 Geopotential and velocity distributions induced at 48
hours by the 1515L diurnal thermal forcing at 140 (a), 380 (b),
680 (c), and 980 (d) mb. Border labels are in units of km.
Geopotential contour interval is 10 m^2s^{-2} and only velocities
greater than 0.25 $m\ s^{-1}$ are shown.

especially evident in the fields in the middle and lower troposphere (680 mb, 980 mb). While this same tendency exists in the upper troposphere, the north-south demarcation is less well-defined.

The vertical structure of the induced circulation over the eastern portion of the heat source region -- that region which represents Saudi Arabia -- can be examined by considering the point located at (+3000 km, 0 km). At 48 hours, the circulation in the lower troposphere (980 mb) is cyclonic with a geopotential perturbation of about -120 m^2s^{-2}. In the middle troposphere (680 mb) the circulation becomes anticyclonic and the geopotential perturbation is about +100 m^2s^{-2}. In the upper troposphere (380 mb, 140 mb), the circulation is still anticyclonic, but the geopotential perturbation is considerably smaller than in the middle troposphere. West of the center of the heat source, the vertical structure at 48 hours is reversed with a low level anticyclonic pattern which reverses to a middle and upper level cyclonic circulation.

The diurnal pattern imposed in the temporal structure of the forcing is apparent in the geopotential and velocity fields for 140 mb and 380 mb. The sign of the geopotential perturbation changes between 24 and 36 hours and changes again between 36 and 48 hours. While a change in sign is not so apparent at 680 mb and 980 mb, it is apparent that large variations occur in the magnitude of the geopotential perturbations between 24 and 36 hours and between 36 and 48 hours. As in the constant forcing experiment, the wind speeds at 48 hours are about twice as strong as at 24 hours. Again, this results from the

fact that the net forcing in this experiment is positive and there is no mechanism for dissipation included in the model.

3.3 Comparison of Results

The results from these two experiments were very different from one another. In fact, the results were so different that very little can be concluded from the experiments. The one common result from the two experiments is that at the eastern edge of the heat source region -- that is, the region which represents the Saudi Arabian peninsula -- at 48 hours there is a cyclonic circulation induced in the lower troposphere (980 mb) and an anticyclonic circulation induced in the middle troposphere (680 mb). The flow field at 48 hours over the eastern edge of the heat source region in the lower troposphere (980 mb) in both cases indicates a south-southeasterly wind. In the middle troposphere at 48 hours, the wind field over the eastern edge of the heat source region is north-northwesterly. These flow patterns suggest that in the lower troposphere, the induced flow over the Saudi Arabian peninsula is from the Arabian Sea inland to the desert "heat low". In the middle troposphere, the flow which is induced over Saudi Arabia is directed from the desert region offshore to the Arabian Sea. In the upper troposphere, the wind fields in both cases over the eastern edge of the heat source region indicate a south-southeasterly flow. This would suggest that the flow is directed onshore from the Arabian Sea to the Saudi Arabian desert in the upper troposphere. These same general patterns were noted in the results from the 2-dimensional model experiments discussed in Chapter 5. While it can be noted that these similarities do exist between the 48 hour flow fields of the two experiments conducted with the 3-dimensional model,

because of the dissimilarity of the total output domain patterns between the two experiments, the validity of these similarities must be considered very tentative.

One of the possible causes of the extremely different results from the two experiments conducted with the 3-dimensional model is the treatment of the diurnal character of the heating as a smooth cosine function. In the experiments conducted with the 2-dimensional model, the diurnal character of the heating was applied explicitly by computing the vertical structure of the heating at each time step. The results produced by this explicit diurnal forcing in the 2-dimensional model compared very well with the 2-dimensional model results produced by the constant net 24 hour forcing. It may be that simply approximating the diurnal character of the forcing with a cosine curve is an inadequate method. Since the only motiviation for assuming a cosine curve for the temporal structure of the heat source was to solve equation 6.1.57 analytically, it would be possible to use a more realistic temporal structure and solve equation 6.1.57 numerically at each specified time step. This would involve computing the transformation of the vertical structure of the heating $\hat{\widetilde{W}}^n_{m,r}(k)$ at each time step, and using numerical techniques to solve 6.1.57 for $W^n_{m,r}(k,t)$ at each time step. Then, by inverting $W^n_{m,r}(k,t)$ to dimensional physical space as detailed earlier in this chapter, geopotential and velocity perturbations with a more realistic diurnal character could be obtained. This experiment has not yet been conducted.

Another possible explanation for the extreme differences in the fields between the two 3-dimensional experiments is that the results

from neither of the experiments are an accurate representation of what the induced circulation should be. It may be that applying a linear model with no dissipation to this problem is not a justifiable approach. Since all available observations contain influences from elements other than simply the surface sensible heat flux and radiative heating which are considered in this model, it is not possible to verify the results from either experiment. Again, this tends to suggest that these results must be considered very tentative.

4.0 Vertical Mode Analysis

Because the results from the two experiments conducted with the 3-dimensional model were so different as to allow only very tentative conclusions, an analysis of the solutions to the set of shallow water equations defined by 6.1.24, 6.1.25, and 6.1.26 was undertaken for each vertical mode n. This analysis was possible by simply eliminating the vertical inverse transform defined as step 9 in the solution process described in Section 1. By not performing the recombination of the solutions for each vertical mode n into a solution which was dependent on z, the geopotential and velocity perturbations were available at each horizontal grid location for each vertical mode n. This allowed an analysis at any time of the horizontal structure of each vertical mode n.

In order to determine whether or not particular vertical modes were excited more than others, a rather straightforward energy analysis was undertaken. In this section, the methodology and results of the modal energy analysis is described.

In performing the modal energy analysis, the Parceval relation must be invoked. One can show that for any two functions of z given

by $f(z)$ and $g(z)$, because the functions can be expanded in terms of the orthonormal and complete set of eigenfunctions of the finite Stürm-Liouville vertical structure problem defined by 6.1.19 and 6.1.20, the Parceval relation can be written

$$< f(z),g(z) > = \sum_{n=0}^{\infty} f_n \, g_n \qquad (6.4.1)$$

where the vertical inner product $< >$ is defined by 6.1.17.

To obtain the kinetic energy equation, one multiplies 6.1.12 by u and 6.1.13 by v and adds to get

$$\frac{\partial}{\partial t} \left[\frac{1}{2}(u^2+v^2)\right] + \vec{V} \cdot \vec{\nabla} \phi = 0 \qquad (6.4.2)$$

where $\vec{V}$ is the 2-dimensional horizontal velocity and $\vec{\nabla}$ is the 2-dimensional operator. Multiply 6.4.2 by $e^{-z}/(1-e^{-Z}T)$, integrate over z from 0 to Z_T, and invoke Parceval's relation to obtain

$$\sum_{n=0}^{\infty} \left[\frac{\partial}{\partial t} \left(\frac{1}{2}(\vec{V}_n \cdot \vec{V}_n)\right) + \vec{V}_n \cdot \vec{\nabla} \phi_n\right] = 0 \qquad (6.4.3)$$

as the total kinetic energy equation. The first term represents the time rate of change of total kinetic energy for mode n and the second term represents the conversion of mode n available potential energy to kinetic energy. No generation terms appear in 6.4.3 because there are no momentum sources or sinks in this model.

To obtain the available potential energy equation, multiply 6.1.14 by $\phi \, e^{-Z}/(1-e^{-Z}T)$, integrate over all z from 0 to Z_T, invoke Parceval's relation and the boundary conditions 6.1.15, 6.1.16, and 6.1.20 to get

$$\sum_{n=0}^{\infty} [\frac{\partial}{\partial t} (\frac{1}{2} \frac{\phi_n^2}{gh_n}) + \phi_n \, \vec{V} \cdot \vec{V}_n] =$$

$$\sum_{n=0}^{\infty} \phi_n [\frac{1}{1 - e^{-Z_T}} \, \{\frac{e^{-Z}\Psi_n \dot{Q}}{\Gamma C_p}\}|_0^{Z_T}$$

$$- \{e^Z \frac{\partial}{\partial z}(\frac{e^{-Z}\dot{Q}}{\Gamma C_p})\}_n] \qquad (6.4.4)$$

where $\{ \ \} \, |_0^{Z_T}$ means the term within brackets evaluated at Z_T minus the terms within brackets evaluated at 0, and $\{ \ \}_n$ means the mode n spectral coefficient of the term within brackets. The first term represents the time rate of change of available potential energy for mode n; the second term represents the conversion of mode n available potential energy to kinetic energy; and, the term on the right hand side represents the generation of mode n available potential energy. With these interpretations of the terms in 6.4.4, the total available potential energy $(\sum_{n=0}^{\infty} \frac{1}{2} \frac{\phi_n^2}{gh_n})$ and the portion of the available potential energy in each mode n at each horizontal grid point can be computed. This analysis can then be used to identify modes which contain most of the available potential energy.

For each experiment, the percent of the total available potential energy in each mode n for the center grid point of the model domain was computed at 24 and 48 hours. The results are given in Table 6.1.

TABLE 6.1

Percentage of the total available potential energy in each vertical
mode at 24 and 48 hours for the two cases of thermal forcing.

Mode	Net 24 Hour Constant Forcing		1515L Diurnal Forcing	
	24 Hours	48 Hours	24 Hours	48 Hours
0	0.00	0.00	0.00	0.00
1	0.80	0.75	0.00	0.00
2	0.07	0.68	2.50	1.57
3	31.35	26.76	6.02	2.59
4	0.06	0.07	23.07	15.91
5	13.65	15.50	18.80	14.15
6	2.33	2.80	10.57	10.68
7	7.74	9.97	22.40	30.00
8	3.45	4.85	15.31	24.86
9	0.00	0.00	0.00	0.00
10	0.00	0.00	0.00	0.00
11	0.00	0.00	0.00	0.00
12	0.00	0.00	0.00	0.00
13	0.00	0.00	0.00	0.00
14	0.00	0.00	0.00	0.00
15	0.01	0.01	0.00	0.00
16	0.01	0.01	0.00	0.00
17	0.09	0.08	0.01	0.00
18	40.43	38.50	0.69	0.22

In the case of the net 24 hour constant forcing at 48 hours, 90.73% of the total available potential energy is contained in modes 3,5,7, and 18. For the 1515L diurnal forcing case, 95.60% of the total available potential energy at 48 hours is contained in modes 4-8. It is interesting to note that none of the available potential energy in either case is contained in mode 0 which corresponds to the external mode with an equivalent depth of about 8.390 km. The large component of energy resident in mode 18 in the case of the net 24 hour constant forcing is a reflection of the large spike near the surface in the vertical heating profile shown in Figure 6.1. This large spike is well captured by the vertical structure of the mode 18 eigenfunction.

Recall that the vertically stratified solutions given in Figures 6.5-6.8 were derived by recombining all the vertical modes. In the construction of these total solutions, the dimensionalization process included a step in which the nondimensional u_n, v_n, and ϕ_n quantities at each horizontal grid point were multiplied by $(gh_n)^{1/2}$, $(gh_n)^{1/2}$, gh_n, respectively. In the case of $n = 0$, $(gh_n)^{1/2} \sim 287$ m s^{-1}. However, for $n = 18$, $(gh_n)^{1/2} \sim 0.65$ m s^{-1}. Therefore, the dimensionalized quantities for mode 0 have much larger magnitudes than the mode 18 dimensionalized quantities. Consequently, when the total solution for a particular value of z is obtained by recombining at each horizontal grid point the dimensionalized quantities for each vertical mode multiplied by the modal eigenfunction evaluated at z (see equation 6.1.22), it is likely that the large magnitudes associated with the lower order modes will dominate the total solution. To test this hypothesis, the 48 hour solution for 140 mb was reconstructed using only the mode 0 contribution for both cases of

thermal forcing. Figure 6.9a shows the mode 0 only 140 mb reconstruction for the case of the net 24 hour constant forcing case, and Figure 6.9b shows the same result for the 1515L diurnal forcing case. Comparing Figure 6.9a to Figure 6.5a and Figure 6.9b to Figure 6.8a clearly shows that the mode 0 contribution is dominating the total solution. The contributions from modes 1-18 to the total solutions at 140 mb shown in Figures 6.5a and 6.8a serve simply to refine the mode 0 contribution shown in Figures 6.9a and 6.9b. Therefore, in spite of the fact that essentially no energy is present in mode 0, the character of the total solution is dominated by the mode 0 contribution.

In an attempt to overcome this problem, a vertical reconstruction was undertaken using modes other than mode 0. Because -- as is indicated in Table 6.1 -- most of the energy was contained in a few vertical modes, the vertically dependent solutions were constructed for both experiments at 48 hours using only the modes with 10% or more of the available potential energy. In the case of the net 24 hour constant forcing, modes 3, 5, 7, and 18 were used in the determination of the vertical stratification. For the 1515L diurnal forcing case, modes 4-8 were recombined to yield the vertically dependent solution. The results of this selective mode recombination for the net 24 hour constant forcing case are shown in Figure 6.10, and the same results for the 1515L diurnal forcing case are given in Figure 6.11. The same general patterns which are present in the total solutions shown in Figures 6.5 and 6.8 are still evident in the results from the selective mode recombination. However, in the selective mode recombination, one additional change of sign is evident in the

140 MB   AT 48.0 HRS

(a)

140 MB   AT 48.0 HRS

(b)
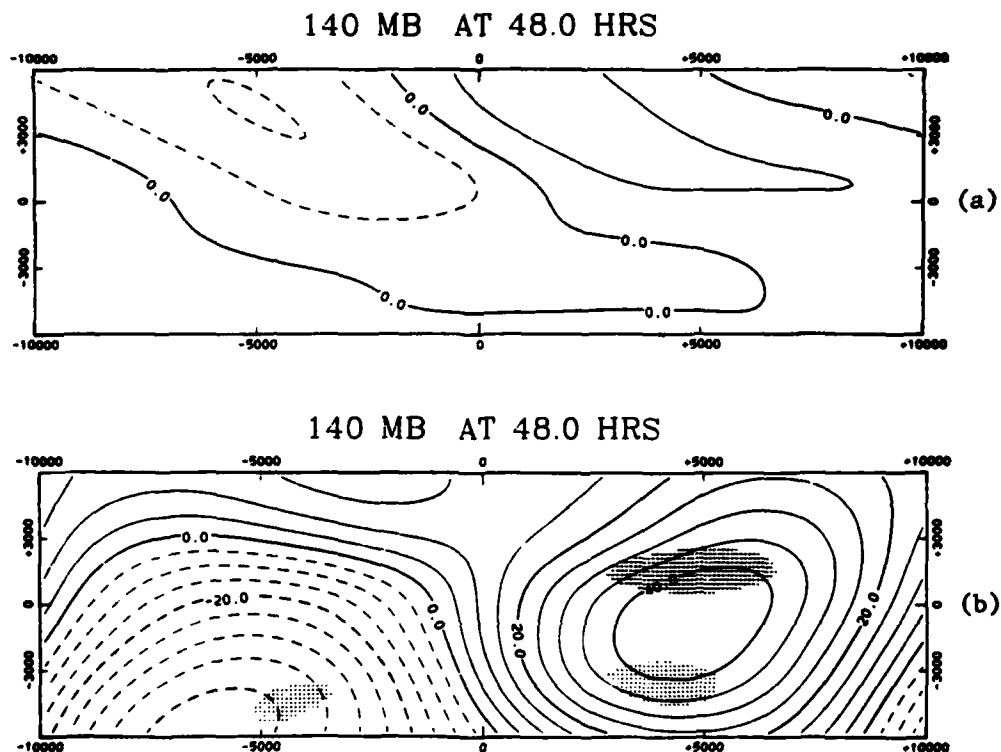
Figure 6.9 Geopotential and velocity distributions induced at 48
hours for the net 24 hour constant (a) and the 1515L diurnal (b)
thermal forcing determined by considering mode 0 only. Border
labels are in units of km. Geopotential contour interval is 5 m^2s^{-2}
and only velocities greater than 0.25 m s^{-1} are shown.

140 MB AT 48.0 HRS

380 MB AT 48.0 HRS

680 MB AT 48.0 HRS

980 MB AT 48.0 HRS
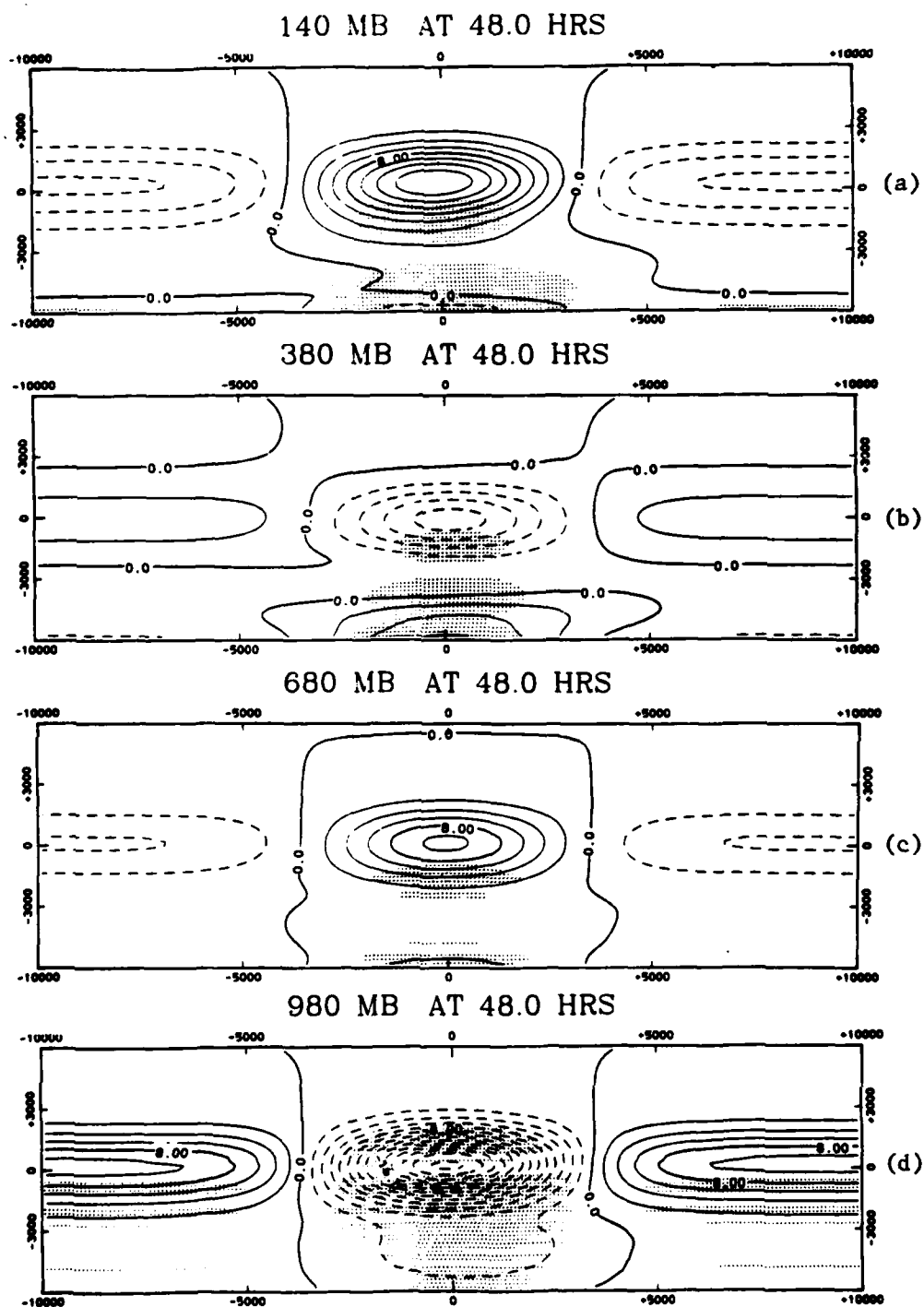
Figure 6.10 Geopotential and velocity distributions induced at 48 hours by the net 24 hour constant thermal forcing at 140 (a), 380 (b), 680 (c), and 980 (d) mb determined by considering modes 3, 5, 7, and 18 only. Border labels are in units of km. Geopotential contour interval is 2 m^2s^{-2} and only velocities greater than 0.25 $m\ s^{-1}$ are shown.

140 MB AT 48.0 HRS

(a)

380 MB AT 48.0 HRS

(b)

680 MB AT 48.0 HRS

(c)

980 MB AT 48.0 HRS

(d)
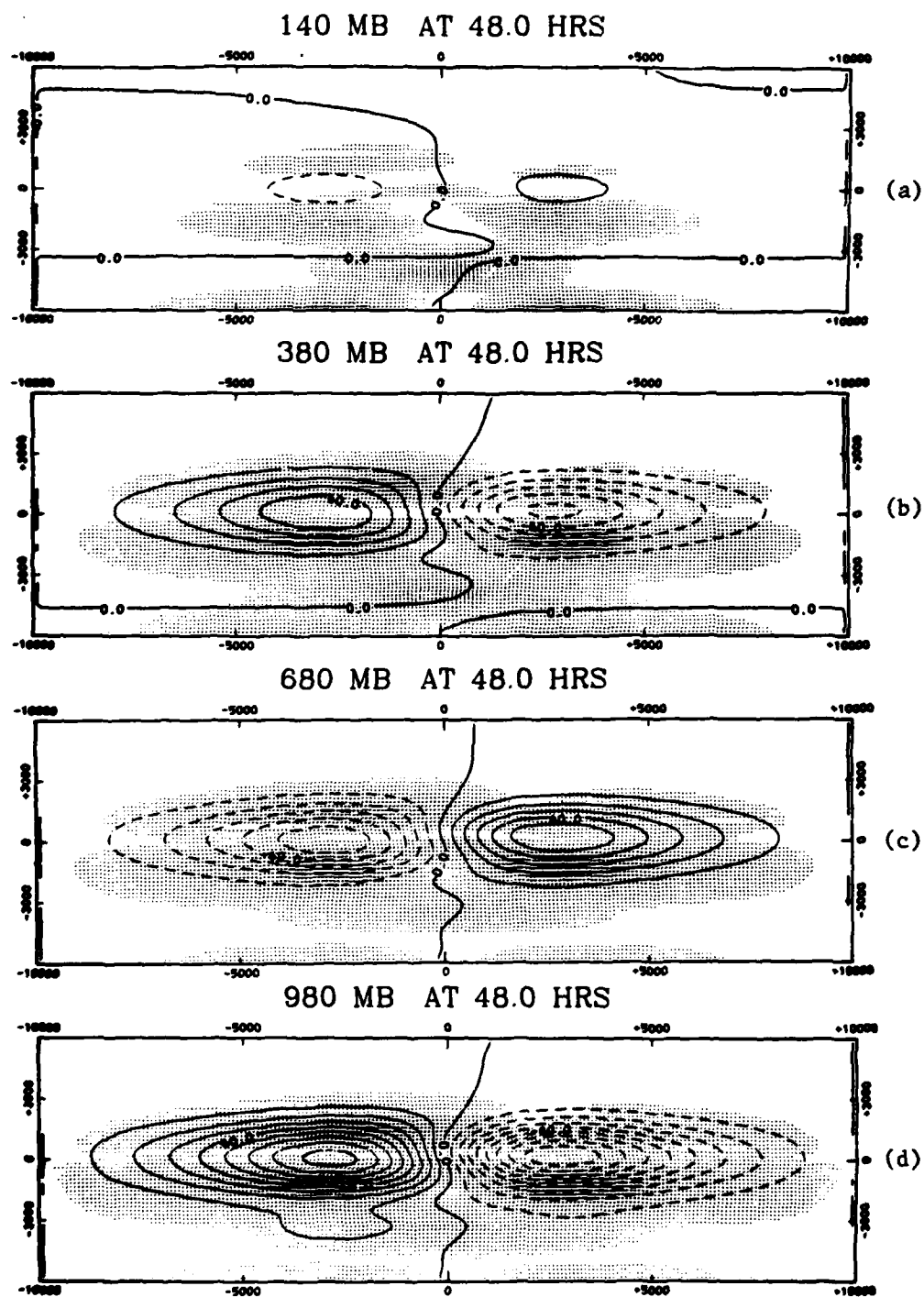
Figure 6.11 Geopotential and velocity distributions induced at 48 hours by the 1515L diurnal thermal forcing at 140 (a), 380 (b), 680 (c), and 980 (d) mb determined by considering modes 4-8 only. Border labels are in units of km. Geopotential contour interval is 15 $m^2 s^{-2}$ and only velocities greater than 0.25 m s^{-1} are shown.

vertical structure. The region of the output domain which represents Saudi Arabia (~ +3000 km, 0 km) is characterized in both cases by a cyclonic circulation at 980 mb, an anticyclonic circulation at 680 mb, a cyclonic circulation at 380 mb, and an anticyclonic circulation at 140 mb. Outside of the similarity in general vertical structure, the results from these two selective mode recombination experiments are just as different as the results for the two cases obtained in the recombination of all the vertical modes.

In summary, in spite of the fact that the modal energy analysis indicated that only a few vertical modes contain nearly all the available potential energy in the induced circulation, the flow patterns produced by recombining only selected vertical modes for the two cases of thermal forcing are still inconclusive.

5.0 Summary of the 3-Dimensional Experiments and Recommendations for

Further Study

Overall, the use of the 3-dimensional equatorial beta plane model to determine the impact of the desert region to the west on the local circulation induced by the heating gradients which exist between the Saudi Arabian desert and the western Arabian Sea was very disappointing. A brief description of the experiments and a summary of the results are presented in this section. Finally, a recommendation is included for further experiments with this 3-dimensional model.

5.1 <u>Summary of Results</u>

Experiments were conducted with a 3-dimensional equatorial beta plane model solved using transform techniques for two idealized cases of thermal forcing. In one experiment, a constant thermal forcing was applied with a vertical structure given by the vertical profile of the net 24 hour radiative and sensible heating as determined from observations over the Saudi Arabian desert during the 1979 Summer MONEX. The vertical structure of the thermal forcing in the second experiment was specified as the vertical profile of the 1515L radiative and sensible heating over the desert. In this second experiment, the temporal variation of the thermal forcing was specified as a cosine function with a frequency such that one cycle was completed in 24 hours. In both experiments, the horizontal structure of the thermal forcing was specified as an elongated 2-dimensional Guassian distribution about the center of the heat source region. The heat source center was located approximately 18°N of the equator and approximately 3000 km west of the Saudi Arabian desert. No sources or sinks of momentum were included in this model.

Because the transform method of solution was employed in all three spatial coordinates, it was possible to examine the horizontal structure of each vertical mode or the horizontal structure at a specified value of the vertical coordinate. The solutions at a particular value of the vertical coordinate were obtained by combining at each horizontal gridpoint the appropriately weighted contribution from each vertical mode. A comparison of the vertically stratified solutions for each case of the thermal forcing revealed very different

flow patterns. Neither of the two thermal forcing cases was capable of producing features of the large scale flow which could be considered representative of the observed flow over North Africa and Saudi Arabia. In fact, the flow fields from the two experiments were so dissimilar from one another and from available observations as to allow no significant conclusions to be drawn about the impact of the desert region to the west on the locally induced circulation over Saudi Arabia.

In spite of the failure of this modelling effort to accomplish the original objective of determining the impact of an external influence on the local desert-ocean circulation over Saudi Arabia, some general information about the modelling technique was revealed. An analysis of the available potential energy in the flow fields at 48 hours for each of the 19 vertical modes for both cases of thermal forcing revealed that more than 90% of the energy was resident in a few selected vertical modes. However, the energy analysis revealed essentially no energy in the lowest order mode (0) for either case of thermal forcing. Nevertheless, by comparing the horizontal structure of the vertically stratified solutions determined by recombining all the vertical modes (0-18) with the vertically stratified solutions determined using the contribution from only the lowest order vertical mode (0), a dominance of this lowest order mode was observed in the total solutions. This dominance is a result of the large phase speeds associated with the lower order modes -- those with large equivalent depths. The phase speeds for each vertical mode enter the vertical stratification process through a step which involves dimensionalizing the spectral coefficients for each vertical mode before they are

combined to yield the vertical stratification. The dimensionalization is accomplished by multiplying the nondimensional spectral wind and geopotential coefficients by the phase speed and the square of the phase speed, respectively, for each vertical mode. Since the lower order modes have the largest phase speeds, the dimensionalized results from the lower order modes tend to dominate the total solution when they are combined with all other modes. Because of this inherent problem in the method of handling the vertical structure, it may be that this modelling technique is best suited to applications where only one vertical mode is of interest. This was the case in the application of this model by Silva Dias et al., 1983. That is, this technique can best be applied to cases where the thermal forcing excites only one of the vertical modes. When that is the case, then the horizontal structure associated with that particular vertical mode should accurately represent the horizontal structure which would be induced in the "real" atmosphere by that thermal forcing.

5.2 Recommendations for Further Study

The two primary shortcomings of this modelling effort can be stated as follows:

1) The specification of the horizontal character of the thermal forcing for both the net 24 hour constant forcing case and the 1515L diurnal forcing case as an elongated 2-dimensional Gaussian distribution is not a very realistic treatment of what the "real" thermal forcing is; and

2) The specification of the temporal character of the thermal forcing for the 1515L diurnal forcing case as a simple cosine function is certainly not a very accurate method.

Both shortcomings were motivated out of a desire to keep the horizontal and temporal character of the thermal forcing in a form that would allow analytical solutions to the transformed system of equations. That is, the specifications of the horizontal and temporal character of the thermal forcing were chosen as much or more for their mathematical practicality as for their physical exactness. While the specifications did allow analytical solutions to be obtained, little information was contained in those analytical solutions. Even though it was convenient to be able to transform the horizontal character of the thermal forcing analytically and to obtain analytical solutions in time to the transformed system of equations, it was not necessary. It would be possible to perform the horizontal transforms numerically and to use numerical techniques to obtain the solutions to the transformed equations in time. After all, the vertical transform employed in this study was done numerically already. The recommendation for further research with this model is to use such numerical techniques.

If numerical techniques were used to perform the transforms in all three spatial coordinates, then it would be possible to use realistic thermal forcing in the model. The method of solution could then be outlined as follows:

1. Specify a large scale mean vertical temperature profile which can be used to compute the vertical structure functions and phase speeds for each vertical mode n using 6.1.19 and 6.1.20.

2. Determine the diurnal variation of the vertical profile of the thermal forcing at equally spaced horizontal gridpoints in the output domain.

At each time step, perform the operations below.

3. Use 6.1.18 to compute the vertical transform of the current u,v,and ϕ fields and the forcing numerically at each point in the horizontal for each vertical mode n.

4. Use 6.1.34 to compute the east-west transform of the current u,v, and ϕ fields and the forcing at each point in the north-south direction for each vertical mode n.

5. Use 6.1.46 to compute the north-south transform for each vertical mode n. The result is the spatially transformed u,v, and ϕ fields and the forcing at this time step.

6. Use 6.1.57 to step forward in time to obtain the transformed u,v, and ϕ fields for each vertical mode n at a new time.

7. Use 6.1.47 to obtain the u,v,and ϕ fields at the new time at each point in the north-south direction for each vertical mode n.

8. Use 6.1.35 to obtain the u,v, and ϕ fields at the new time at each horizontal point for each vertical mode n.

9. Use 6.1.22 to obtain the u,v, and ϕ fields at any specified location in the vertical at the new time.

10. Return to step 3 and use the vertical structure of the u,v,and ϕ fields and the forcing at the new time to repeat the process.

Admittedly, this is a very bold undertaking. However, the procedure is a much more accurate representation of the processes at work in the "real" atmosphere and therefore should yield more acceptable results.

END

MICROCOPY RESOLUTION TEST CHART
NATIONAL BUREAU OF STANDARDS-1963-A
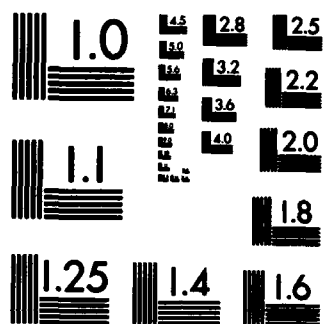
VII. SUMMARY AND CONCLUSIONS

The results from several experiments conducted with three separate numerical models are presented in this thesis. A 1-dimensional model is used to predict mixed layer growth over a dry desert caused by surface sensible heat flux. Results from this 1-dimensional model are then incorporated into two more complex numerical models to simulate the formation and evolution of a "heat low". A 2-dimensional, axisymmetric, primitive equation model formulated on a f-plane is used to examine the diurnal character of the circulation induced by the horizontal gradients in thermal forcing between a dry, hot desert and an adjacent ocean. A 3-dimensional model formulated on an equatorial beta plane and solved using transforms in the three spatial coordinates is employed in an attempt to examine the impact on a locally induced circulation of a nearby large desert region. The thermal forcing for each of these models is based on analyses of observations.

The observations consist of two data sets collected during the late spring and early summer season over the Saudi Arabian peninsula and the adjacent Arabian Sea. Data collected during the Pre-Onset Saudi Arabian Heat Source Phase of the Summer MONEX in May, 1979 are analyzed to obtain vertical profiles of temperature, water vapor mixing ratio, and dust loading over the Saudi Arabian desert and the western Arabian Sea. A second data set, collected during June, 1981 in the Saudi Arabian desert by a surface based observing station, is

used to determine the diurnal surface temperature trace over the desert and other surface characteristics. In addition to these observations, climatological vertical profiles of ozone and carbon dioxide concentrations are employed to determine the radiative components of the thermal forcing.

The forcing in the 1-dimensional mixed layer growth model consists of surface sensible heat flux as determined by the bulk aerodynamic equations. The diurnal surface temperature trace and the vertical profile of potential temperature above the mixed layer are specified as are the initial potential temperature of the mixed layer and the initial depth of the mixed layer. As the surface temperature increases during its diurnal cycle, the potential temperature and the depth of the mixed layer also increase. Eventually, when the surface temperature, on its diurnal cycle, falls below the temperature of the air in the mixed layer, the mixed layer growth stops and the diurnal growth cycle is completed. To begin the next diurnal cycle, the mixed layer is divided into two layers. A surface layer is established with a fixed depth. The potential temperature at the top of this surface layer is determined by adding to the surface potential temperature some fraction of the difference between the potential temperature within the mixed layer at the end of the last diurnal cycle and the surface potential temperature. Above this surface layer, an intermediate layer is established where the potential temperature increases from the value determined at the top of the surface layer to the potential temperature of the mixed layer at the end of the last diurnal cycle. The top of this intermediate layer is set at the depth of the mixed layer at the end of the last diurnal cycle. This

specification of the potential temperature profile results in a very stable surface layer and a weakly stable intermediate layer. Then, the diurnal surface sensible heat flux cycle is repeated. After several diurnal cycles are completed, a steady state emerges for the diurnal growth of the mixed layer. In this steady state, the surface sensible heat flux provides exactly enough energy to allow the mixed layer to grow through the strongly stable surface layer and through the slightly stable layer above the surface layer to the same height as at the end of the previous diurnal cycle. Several experiments were conducted by varying the surface layer depth and the fraction used to determine the temperature at the top of the surface layer. The primary results derived from the 1-dimensional model experiments are summarized in the following points.

⊚ After seven diurnal cycles, all experiments reach a
steady state for mixed layer growth.

⊚ A vertical potential temperature profile which best
matches the observations is produced with a surface layer
25 mb deep and a potential temperature at the top of the
surface layer determined by adding the surface potential
temperature to 85% of the difference between the mixed layer
potential temperature at the end of the previous diurnal
cycle and the surface potential temperature.

⊙ In the case which best matches observations, the
steady state diurnal cycle shows the mixed layer growing
through about 350 mb and reaching the 650 mb level.

⊙ Mixed layer growth is confined to the very stable
25 mb thick surface layer for about the first six hours
after sunrise. In the next four hours, the mixed layer
grows rapidly through a 325 mb-thick, weakly-stable
layer and reaches its maximum depth within about 10 hours
of sunrise.

The diurnal growth of the mixed layer depicted by the 1-dimensional
model experiments is used to vertically distribute surface sensible
heat in the 2 and 3-dimensional models.

In the 2 and 3-dimensional models, the thermal forcing is the sum
of a radiative component and a sensible component. The vertical
distribution of the radiative heating component is generated by
radiative transfer calculations which rely upon vertical profiles of
temperature, water vapor mixing ratio, ozone mixing ratio, carbon
dioxide mixing ratio, and dust loading as input data. The vertical
profiles of temperature, water vapor mixing ratio, and dust loading
are determined for the desert and for the oceanic regions from
observations. Climatological vertical profiles of ozone mixing ratio
and carbon dioxide mixing ratio are used to supplement the
observational data. The radiative heating as a function of height is
determined as a function of time of day for both the desert and the
oceanic regions. The surface sensible heating component over the

desert is parameterized in terms of the net radiation at the surface.
Once the magnitude of the total surface sensible heating component is
determined as a function of time of day, the sensible heat is
distributed vertically in accordance with the diurnal growth of the
mixed layer determined by the 1-dimensional model described above. By
considering and ignoring the dust loading in the atmosphere, it is
possible to determine the radiative and sensible components of the
thermal forcing for a dust laden atmosphere and for a clear
atmosphere. The results of the determination of the radiative and
sensible heating components of the thermal forcing are presented in
the following points.

⊙ In the clear atmosphere, there is a region of radiative
   heating during the middle part of the day through the middle
   troposphere. Over the desert, the radiative heating occurs
   from about 0800-1700 L and from 920 mb to 320 mb at its peak
   near 1200 L. Over the ocean, the radiative heating occurs
   from about 0830-1530 L and from 770 mb to 320 mb at its
   peak near 1200 L. The maximum heating over the desert occurs
   at 620 mb at 1200L and has a magnitude of 0.0818 K hr^{-1}
   while over the ocean the maximum heating occurs at 680 mb at
   1200 L and has a magnitude of 0.0390 K hr^{-1}.

⊙ In the dust laden atmosphere, the radiative heating
   is enhanced over the desert and the ocean in time, in space,
   and in magnitude. The magnitude of the maximum heating
   becomes 0.1941 K hr^{-1} over the desert and 0.0949 K hr^{-1}

over the ocean. The time period over which radiative heating
occurs increases by about one hour over the desert (0700-
1700 L) and by about two hours over the ocean (0730-1630 L).
Over the ocean, the region of radiative heating at 1200 L is
extended downward to about 800 mb.

⊚ The vertical profiles of 24 hour net radiative heating
for a clear atmosphere indicate net radiative cooling every-
where over the desert and over the ocean. In the dust laden
atmosphere, 24 hour net radiative heating occurs in the region
between 830 mb and 530 mb over the desert. Over the ocean,
the dust laden atmosphere simply exhibits less net radiative
cooling than in the case of a clear atmosphere.

⊚ The impact of the dust on the sensible component
over the desert is to reduce the magnitude of the surface
sensible heating at all times. Near local noon, the
sensible component for the dust laden atmosphere is
about 20% less than the sensible component for the
clear atmosphere. The sensible heating is positive from
about 0545 L until 1715 L for the clear atmosphere.
However, in the dust laden atmosphere, the sensible
heating is positive between about 0630 L and 1630 L --
a total reduction of 1.5 hours in the time during which
the atmosphere experiences surface sensible heating.

These results are in agreement with previous results reported by Ackerman and Cox (1982). The thermal forcing for both the clear atmosphere and the dust laden atmosphere are used in the 2-dimensional model to examine the induced circulation in both cases and to determine the impact of the dust on the induced circulation. Only the clear atmosphere profiles are used in the 3-dimensional model to examine the impact of a large desert region on the local circulation induced by the desert-ocean gradients in thermal forcing.

In the 2-dimensional model, the thermal forcing is defined for two regions of the model domain. The vertical profile of the thermal forcing determined for the desert is specified as a function of time at the center of the model domain. A weakly decaying exponential factor is then applied to this vertical profile at each time step to provide the horizontal distribution of the thermal forcing over the desert region. Over the oceanic region of the model domain, the vertical profile of the thermal forcing determined for the ocean is specified as a function of time at each horizontal location with no horizontal variability. The thermal forcing over the desert region and the thermal forcing over the oceanic region are meshed by a linear interpolation over a narrow transition region. With the thermal forcing gradients specified, several experiments were conducted with the 2-dimensional model. In all cases, the basic pattern of the induced circulation remains unchanged. The major results of the experiments with the 2-dimensional model are summarized in the following points.

⊙ The horizontal gradients in thermal forcing between
the desert and the ocean induce a surface pressure pattern
with a region of low pressure over the desert and a horizontal
pressure difference between the desert and the ocean regions
of about 4-5 mb in the late afternoon and about 1 mb in the
early morning. The diurnal pressure variation over the
desert is about 4 mb. However, over the ocean, the
diurnal pressure change is less than 1 mb.

⊙ The tangential flow field shows a low-level cyclonic
circulation over the desert and a mid-level anticyclonic
circulation. This tangential circulation pattern persists
throughout the diurnal cycle with the strength of the
tangential flow exhibiting a diurnal character. The
cyclonic circulation extends upward from the surface
to near the 700 mb level over the desert and the
circulation is strongest near local midnight.

⊙ The radial flow field exhibits a strong diurnal
characteristic with late afternoon low-level radial
inflow from the ocean to the desert and early
morning low-level radial outflow from the desert to
the ocean. The mid-level radial flow patterns are
opposite from the low-level patterns. The late

afternoon low-level radial inflow peaks at about
1900 L and decreases in intensity until the
inflow is replaced by radial outflow after local
midnight. By mid morning, the radial inflow
returns at low-levels.

⊙ The vertical motion field is characterized by
upward vertical motion from the surface to about 500 mb
in the late afternoon over the desert. Weak subsidence
occurs over the ocean. In the early morning, subsidence
occurs over the desert from about 550 mb to the surface.
The transition from upward to downward motion occurs in
the early morning hours after local midnight. The
subsidence continues until after sunrise when the
upward motion begins in the low-levels over the desert.
This diurnal pattern in the vertical motion field is
consistent with the diurnal patterns in the radial
and tangential flow fields.

⊙ The circulation patterns which result from the
thermal forcing for a dust laden atmosphere are weaker
than the patterns which result from the clear air thermal
forcing. The impact of the dust on the induced
circulations is to reduce the intensity of the circulation
because of the reduced surface sensible heat flux in the
dust laden case. The increased radiative heating aloft

caused by the dust has no appreciable impact on the induced circulation. The surface sensible heat flux over the desert is the factor which controls the intensity of the resulting circulation.

⊙ The circulation patterns produced by a constant thermal forcing such that during a 24 hour period the total forcing is exactly equal to the 24 hour net forcing in the diurnally forced cases are similar in form but weaker in magnitude than the late afternoon patterns produced by the cases with diurnal forcing.

These results from the 2-dimensional model must be interpreted with some caution. The 2-dimensional model contains no influences from regions outside the model domain. The results are a reflection only of the circulation which would be induced by the horizontal gradients in thermal forcing which are imposed on the model domain.

One of the many possible external influences on the locally induced 2-dimensional circulation between the Saudi Arabian desert and the western Arabian Sea is the westward expanse of the Sahara Desert across North Africa. To try to examine the impact that this desert region might have on the circulation patterns obtained in the experiments with the 2-dimensional model, a large scale 3-dimensional model is employed. In the 3-dimensional model, the governing equations are formulated in log pressure coordinates on an equatorial beta plane. After linearizing the equations about a resting basic state, the equations are solved using transform techniques. The

vertical transform reduces the system to a set of equations which have the same form as the shallow water equations. A fourier transform is employed in the east-west direction, and a generalized hermite transform is employed in the north-south direction. These transforms in the two horizontal spatial coordinates reduce each set of shallow water equations to a first order differential equation in time which can be solved analytically if the time dependence of the specified thermal forcing is chosen appropriately. The analytical solutions are then inverse transformed to solutions in x, y, z, t physical space. The vertical structure of the thermal forcing for the experiments with the 3-dimensional model is based on the vertical structure of the net radiative and sensible components of the thermal forcing for a clear atmosphere which are used in the 2-dimensional model. The horizontal structure of the thermal forcing is specified as an east-west elongated Gaussian distribution with an e-folding radius in the east-west direction of about 3170 km and a north-south e-folding radius of about 870 km.

Results are reported from two experiments conducted with the 3-dimensional numerical model. In the first experiment, the vertical structure of the thermal forcing is specified as the vertical profile of the net 24 hour radiative and sensible heating as determined from the observations over the Saudi Arabian desert. In this experiment, the thermal forcing is constant -- there is no temporal variation. The second experiment allows a thermal forcing which exhibits a simple cosine dependence in time with a period of 1 day. The vertical structure of the thermal forcing for this second experiment is specified as the vertical profile of the radiative and sensible

heating over the desert at 1515L. Unlike the results from the 2-dimensional model, the 3-dimensional model results for the constant thermal forcing case are very different from the results for the case of a diurnally varying thermal forcing. Neither case of thermal forcing produces large scale flow fields which resemble observations of the patterns of North Africa and Saudi Arabia. Unfortunately, the results are so dissimilar from one another and from observations that no firm conclusions can be drawn about the impact of the Sahara desert on the local circulation over Saudi Arabia.

Nevertheless, an energy analysis of the induced flow fields reveals that the vertically stratified solutions obtained with this 3-dimensional transform technique are dominated by the contributions from the lowest order vertical mode. This is true in spite of the fact that little energy is resident in that particular vertical mode. The implication is that this technique may hold little promise for determining solutions which are fully stratified in the vertical. The best application of this technique is to cases where the vertical structure of the thermal forcing projects nearly entirely onto a single vertical mode. Then, the horizontal structure of that vertical mode will likely represent the general horizontal structure which the thermal forcing will induce in the atmosphere.

REFERENCES

Ackerman, S. A., and S. K. Cox, 1982: The Saudi Arabian heat low: aerosol distributions and thermodynamic structure. J. Geophys. Res. 87, C11, 8991-9002.

Ackerman, S. A., E. A. Smith and S. K. Cox, 1983: Surface and atmospheric radiative exchange over the Arabian Peninsula, Preprint Volume of Fifth Conference on Atmospheric Radiation, 31 October - 4 November, 1983, Baltimore, Maryland, 481-483.

Arakawa, A., 1972: Design of the UCLA general circulation model. Numerical simulation of weather and climate, Technical Report 7, Department of Meteorology, University of California, Los Angeles.

Arfken, G., 1970: Mathematical Methods for Physicists, Second Edition, New York, Academic Press, 815 pp.

Asselin, R., 1972: Frequency filter for time integrations. Mon. Wea. Rev., 100, 487-490.

Blake, D. W., T. N. Krishnamurti, S. V. Low-Nam, and J. S. Fein, 1983: Heat low over the Saudi Arabian Desert during May 1979 (Summer MONEX), Mon. Wea. Rev., 111, 1759-1775.

Bolhofer, W., M. Chambers, D. Frey, J. Kuettner, and S. Unninayar, 1981: Summer MONEX U.S. Research Flight Missions, May - July 1979. U.S. MONEX Project Office, National Center for Atmospheric Research, Boulder, CO., 220 pp.

Busch, N. E., S. W. Chang, and R. A. Anthes, 1976: A multi-level model of the planetary boundary layer suitable for use with mesoscale dynamic models. J. Appl. Meteorol., 15, 909-919.

Cox, S. K., M. C. Polifka, K. Griffith, A. Rockwood, and D. Starr, 1976: Radiative transfer computational routines for atmospheric science applications. Atmospheric Science Research Report, Colorado State University, Fort Collins, CO., 75 pp.

Dixit, C. M., and D. R. Jones, 1965: A kinematic and dynamical study of active and weak monsoon conditions over India during June and July 1964, International Meteorological Center, Bombay (Prepublication).

Driedonks, A. G. M., 1982: Models and observations of the growth of atmospheric boundary layer. Boundary Layer Meteorology, 23, 283-306.

Erdélyi, A., W. Magnus, F. Oberhettinger, and F. G. Tricomi, 1954: Tables of Integral Transforms, 2 volumes, McGraw-Hill, New York.

Fingerhut, W. A., 1978: A numerical model of diurnally varying tropical cloud cluster disturbance. Mon. Wea. Rev., 106, 255-264.

Fulton, S. R., 1982: Numerical evaluation of vertical transforms. Unpublished report in Department of Atmospheric Science, Colorado State University, Fort Collins, CO., 16 pp.

Fulton, S. R., and W. H. Schubert, 1984: Vertical normal mode transforms: theory and application. Submitted to Mon. Wea. Rev., May,1984.

Hack, J. J., and W. H Schubert, 1976: Design of an axisymmetric primitive equation tropical cyclone model. Atmospheric Science Paper, #263, Colorado State University, Fort Collins, CO., 70 pp.

Hack, J. J. and W. H. Schubert, 1980: The role of convective scale processes in tropical cyclone development. Atmospheric Science Paper, #330, Colorado State University, Fort Collins, CO., 206 pp.

Hildebrand, F. B., 1962: Advanced Calculus for Applications, Englewood Cliffs, New Jersey, Prentice-Hall, 646 pp.

Holton, J. R., 1979: An Introduction to Dynamic Meteorology, 2nd Edition, New York, Academic Press, 391 pp.

Kidwell, K. B., 1979: NOAA polar orbiter data (TIROS-N and NOAA-6) users guide, NOAA-NESDIS, Washington, D.C., 147 pp.

Krishnamurti, T. N., P. Greiman, Y. Ramanathan, R. Pasch, and P. Ardanuy, 1980: Quick Look Summer MONEX Atlas, Part 1, Saudi Arabia Phase, Florida State University Report Number 80-4, Department of Meteorology, Florida State University, Tallahassee, Florida 32306, 71 pp.

Kurihara, Y. and R. E. Tuleya, 1974: Structure of a tropical cyclone developed in a three-dimensional numerical simulation model. J. Atmos. Sci., 31, 893-919.

Lilly, D. K., 1968: Models of cloud-topped mixed layers under a strong inversion. Quart. J. Roy. Meteorol. Soc., 94, 292-309.

Manabe, S., and R. F. Strickler, 1964: Thermal equilibrium of the atmosphere with a convective adjustment. J. Atmos. Sci., 24, 361-385.

Matsuno. T., 1966a: Quasi-geostrophic motions in the equatorial area.
    Journal of the Meteorological Society of Japan, 44, 25-43.

Matsuno, T., 1966b: Numerical integrations of the primitive equations
    by a simulated backward difference method. Journal of the
    Meteorological Society of Japan, Series 2, 44, 76-84.

McBride, J. L. and W. M. Gray, 1978: Mass divergence in tropical
    weather systems. Atmospheric Science Paper, #299, Colorado
    State University, Fort Collins, CO., 109 pp.

McClatchey, R. A., R. W. Fenn, J. E. A. Selby, F. E. Volz, and J. S.
    Garing, 1972: Optical properties of the atmosphere, 3rd Edition.
    Air Force Cambridge Research Laboratories (AFCRL-72-0497)
    Environmental Research Papers, No. 411, 108 pp.

Meteorological Atlas of the International Indian Ocean Expedition,
    Volume 1, The Surface Climate of 1963 and 1964, A joint project
    of the U.S. National Science Foundation and India Meteorological
    Department, U. S. Government Printing Office, 1972.

Ooyama, K., 1969: Numerical simulation of the life cycle of tropical
    cyclones. J. of Atmos. Sci., 26, 3-40.

Paltridge, G. W., and C. M. R. Platt, 1976: Radiative Process in
    Meteorology and Climatology, New York, Elsevier Scientific
    Publishing Company, 318 pp.

Patterson, E. M., G. W. Grams, and C. O. Pollard, 1983: Aircraft
    measurements of aerosol optical properties during the MONEX
    program. Final Technical Report, NSF Project ATM 7820149, School
    of Geophysical Sciences, Georgia Institute of Technology, Atlanta,
    Georgia 30332.

Ramage, C. S., 1971: Monsoon Meteorology, New York, Academic
    Press, 296 pp.

Rao, Y. P., 1976: Southwest Monsoon, Meteorological Monograph
    Synoptic Meteorology Number 1, India Meteorological Department,
    367 pp.

Sellers, W. D., 1965: Physical Climatology, Chicago, University of
    Chicago Press, 272 pp.

Silva Dias, P. L., W. H. Schubert, and M. DeMaria, 1983: Large scale
    response of the tropical atmosphere to transient convection.
    J. Atmos. Sci., 40, 2689-2707.

Smith, E. A., S. A. Ackerman, S. K. Cox, and T. H. Vonder Haar, 1980:
    Summer MONEX high altitude aircraft radiation measurements.
    Department of Atmospheric Science, Colorado State University,
    Fort Collins, CO., 84 pp.

Smith, E. A., M. M. Sakkal, S. A. Ackerman, S. K. Cox, and T. H. Vonder Haar, 1981a: An investigation of the radiative boundary conditions during the development of the southwest monsoon Saudi Arabian heat low. Atmospheric Science Paper, #339, Colorado State University, Fort Collins, CO., 52 pp.

Smith, E. A., S. K. Cox, and T. H. Vonder Haar, 1981b: Preliminary results from an Arabian heat low boundary layer experiment. Post print volume of International Conference on the Scientific Results of the Monsoon Experiment, 26-30 October 1981, Denpasar, Bali, Indonesia, pp. 1-7 - 1-12.

Summer MONEX Field Phase Report, 1981: First GARP Global Experiment Operations Report Series, Volume 8. International MONEX Management Center (summer), New Delhi, 315 pp. (Available from the World Meteorological Organization, Geneva).

Tennekes, H. and A. G. M. Driedonks, 1981: Basic entrainment equations for the atmospheric boundary layer. Boundary Layer Meteorology, 20, 515-531.

Trewartha, G. T., and L. H. Horn, 1980: An Introduction to Climate, New York, McGraw-Hill Book Company, 416 pp.

van de Boogaard, H. M., 1977: The mean circulation of the tropical and sub-tropical atmosphere - July. NCAR Technical Note 118, National Center for Atmospheric Research, Boulder, CO.

APPENDIX A

Derivation of the Radiative Heating Rate Equation and Description of

IRADLON, IRADSOL, and Dust Impact.

The equation used to compute the radiative heating rates can be
arrived at by starting with the form of the 1st Law given by

$$\frac{dQ}{dt} = C_p \frac{dT}{dt} - \alpha \frac{dp}{dt} \qquad (A.1)$$

where Q is the energy per unit mass supplied to the atmospheric layer,
T is the temperature of the layer, α is the specific volume of the
layer, p is the prevailing pressure in the layer and C_p is the
specific heat capacity for dry air. Assuming that the only diabatic
heat source is radiation, that the atmospheric layer is plane parallel
and horizontally homogeneous, and that the process is an
isobaric one so that $\frac{dp}{dt} = 0.0$, then for this atmospheric layer,
the 1st Law may be written

$$\frac{dQ}{dt} = C_p \frac{dT}{dt} \quad . \qquad (A.2)$$

Now, $\frac{dQ}{dt}$ has units of energy/(mass * time). The radiative heat source
terms must then be expressed in the units of energy/(mass * time).
Figure A1 illustrates the information available from IRADSOL and IRADLON
for a given atmospheric layer. The units of the net irradiance
$E_{net} = E_D - E_U$ are W m^{-2} or energy/(time * area). Therefore,

$$\Delta P \left\{ \begin{array}{l} P_1 \quad \underline{ \downarrow E_{1D} \quad \uparrow E_{1U} } \; Z_1 \\ \\ P_0 \quad \underline{ \downarrow E_{OD} \quad \uparrow E_{OU} } \; Z_0 \end{array} \right\} \Delta Z$$

$$E_{net\,1} = E_{1D} - E_{1U}$$
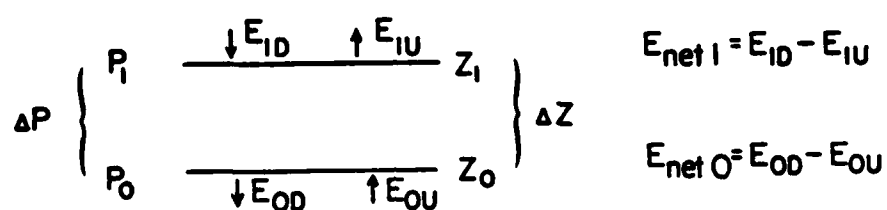
$$E_{net\,O} = E_{OD} - E_{OU}$$

Figure A.1 Illustration of the information available from the broad-band radiative transfer routines IRADLON (LW) and IRADSOL (SW) which can be used to compute radiative heating rates. Numerical subscripts identify levels in pressure or height. E is irradiance.

the units of $\frac{1}{\rho} \frac{\Delta E_{net}}{\Delta Z}$ are energy/(mass * time) where ρ is density
and ΔZ is the thickness of the layer. From the hydrostatic relation,
$\frac{1}{\rho} \frac{1}{\Delta Z} = -\frac{g}{\Delta p}$. So, substituting into equation (A.2) yields
the expression for the heating rate of the layer as

$$\frac{dT}{dt} = -\frac{g}{C_p} \frac{\Delta E_{net}}{\Delta p} \quad . \tag{A.3}$$

This expression is used in both IRADLON and IRADSOL to determine the
longwave and shortwave heating rates, respectively.

The longwave routine IRADLON employs the method of isothermal
emissivities to determine the upward or downward irradiance at a given
pressure level P. That is, the irradiance at a given level P is given
by

$$E(P) = \int \sigma T^4 \, d\bar{\epsilon} + \sigma T_{P_o}^4 \left[1 - \int d\bar{\epsilon} \right] \tag{A.4}$$

where $\bar{\epsilon}$ represents the emissivity of a given layer due to all
possible constituents, T_{P_o} is the temperature of the bounding
surface (ground for an upward irradiance calculation and space for a
downward irradiance calculation), and σ is the Stefan-Boltzmann
constant given by $\sigma = 5.67 \times 10^{-8}$ W m^{-2}K^{-4}. In finite
difference form A.4 is

$$E(P) = \sum_i \sigma T_i^4 \, \Delta\bar{\epsilon}_i + \sigma T_{P_o}^4 \left[1 - \sum_i \Delta\bar{\epsilon}_i \right] \tag{A.5}$$

where the index i is over all layers from level P to the boundary. In
terms of the three most important constituents, (A.5) can be written

$$E(P) = \sum_i \sigma T_i^4 \left[\Delta\bar{\epsilon}_{i_{H_2O}} + \Delta\bar{\epsilon}_{i_{CO_2}} + \Delta\bar{\epsilon}_{i_{O_3}} - \Delta\bar{\epsilon}_{i_{overlap}} \right] +$$

$$\sigma T_{P_o}^4 \left[1 - \sum_i \Delta\bar{\epsilon}_{i_{H_2O}} - \sum_i \Delta\bar{\epsilon}_{i_{CO_2}} - \sum_i \Delta\bar{\epsilon}_{i_{O_3}} + \sum_i \Delta\bar{\epsilon}_{i_{overlap}} \right]$$

$$(A.6)$$

where the H_2O - CO_2 overlap spectral region is accounted for
by the $\Delta\bar{\epsilon}_{i_{overlap}}$ correction terms. IRADLON includes
corrections for collisional broadening during the computation of the
optical path for each constituent. For the downward irradiance
calculations, it is assumed that there is no longwave radiation
incident on the top of the atmosphere and therefore
$\sigma T_{P_o}^4 = 0.0$.

The shortwave routine IRADSOL computes the atmospheric heating
rates due to absorption of the downward broadband solar irradiance and
the upward broadband shortwave irradiance reflected from an underlying
surface with a specified albedo. The absorptivity of a given layer is
determined by considering the individual absorptivities of H_2O,
CO_2 and O_3 as reported by Manabe and Strickler (1964). A
solar zenith angle calculation accounts for diurnal variations in path
lengths through the atmosphere and consideration is made for the
seasonal variation in the solar constant due to the eccentricity of
the earth's orbit. In addition IRADSOL contains a pressure weighted
correction for Rayleigh scattering of the incident shortwave
radiation. The total amount of Rayleigh scattering is designed to be
7%.

Ackerman and Cox (1982) compared observations of the upward and
downward longwave and shortwave irradiances collected by aircraft

during May 1979 in dust laden air with theoretical calculations in order to determine the impact of the dust on the radiative heating of the atmosphere. They concluded that the impact of the dust on the longwave flux was negligible. However, the dust had a significant impact on the shortwave radiation. Using measurements from a Forward Scattering Spectrometer Probe, the dust mass loading was determined as a function of height. Therefore, for a given distance into the dust layer, the density weighted path length of the dust (u) could be determined by the relation

$$u = \sec \theta \int M \, dz \qquad (A.7)$$

where θ is the solar zenith angle, M is the dust mass loading (gm^{-3}) and dz is the depth into the layer. In addition, they defined the fractional absorptance of a layer by the relationship

$$FA = \frac{(\downarrow SW_1 - \uparrow SW_1) - (\downarrow SW_2 - \uparrow SW_2)}{(\downarrow SW_1 + \uparrow SW_2)} \qquad (A.8)$$

where the arrows indicate upward or downward shortwave fluxes, and the subscripts 1 and 2 represent the upper and lower boundaries of a layer. Then, by comparing the observations of fractional absorptance in given layers to theoretical calculations of fractional absorptance, they were able to deduce the fractional absorptance which was due to the presence of dust in the layer. Ackerman and Cox then found a simple relationship to predict the fractional absorptance of the dust as a function of the density weighted path length. Using this relationship and the observations of the dust mass loading described

in Chapter 2, it was possible to include the impact of the dust on the shortwave heating of the atmosphere.

APPENDIX B

2-Dimensional Model Governing Equations and Method of Numerical

Solution

The governing equations in horizontal cartesian vertical pressure coordinates on an f plane are given by

(Eastward Momentum) $\quad \frac{\partial u}{\partial t} + u \frac{\partial u}{\partial x} + v \frac{\partial u}{\partial y} + \omega \frac{\partial u}{\partial p} - fv + \frac{\partial \phi}{\partial x} = F_u \qquad$ (B.1)

(Northward Momentum) $\quad \frac{\partial v}{\partial t} + u \frac{\partial v}{\partial x} + v \frac{\partial v}{\partial y} + \omega \frac{\partial v}{\partial p} + fu + \frac{\partial \phi}{\partial y} = F_v \qquad$ (B.2)

(Hydrostatic) $\qquad\qquad\qquad \frac{\partial \phi}{\partial p} + \alpha = 0 \qquad\qquad\qquad$ (B.3)

(Thermodynamic) $\quad \frac{\partial T}{\partial t} + u \frac{\partial T}{\partial x} + v \frac{\partial T}{\partial y} - \omega \left(\frac{\alpha}{C_p} - \frac{\partial T}{\partial p} \right) = \frac{\dot{Q}}{C_p} + F_T \qquad$ (B.4)

(Continuity) $\qquad\qquad\qquad \frac{\partial u}{\partial x} + \frac{\partial v}{\partial y} + \frac{\partial \omega}{\partial p} = 0 \qquad\qquad$ (B.5)

(Equation of State) $\qquad\qquad\qquad p\alpha = RT \qquad\qquad\qquad$ (B.6)

where u is the eastward component of wind, v the northward component of wind, ω the vertical motion, ϕ the geopotential, T the temperature, α the specific volume, p the pressure, f the Coriolis parameter (constant), R the gas constant for dry air, C_p the specific heat capacity for dry air, $\dot{Q}$ the energy source per unit mass per unit time, and F_u, F_v, and F_T the momentum and thermodynamic sources/sinks.

The vertical coordinate chosen for the numerical model was the sigma coordinate which is defined as

$$\sigma = \frac{P - P_T}{P_S - P_T} = \frac{P - P_T}{\pi} \tag{B.7}$$

where P_T is the fixed pressure at the top of the atmosphere and P_S is the surface pressure which is allowed to vary in both space and time. The sigma coordinate is a generalized pressure coordinate in which the top boundary of the model atmosphere ($P = P_T$) and the bottom boundary of the model atmosphere ($P = P_S$) always have the respective σ values 0 and 1. Therefore, the top and bottom boundary conditions, namely that air parcels do not cross the boundaries, can be written as

$$\frac{d\sigma}{dt} = \dot{\sigma} = 0 \quad \text{at } \sigma = 0, 1. \tag{B.8}$$

It can be shown that the horizontal and vertical derivatives in pressure coordinates can be written in sigma coordinates as follows:

$$\frac{\partial}{\partial x}\Big)_p = \frac{\partial}{\partial x}\Big)_\sigma - \frac{\sigma}{\pi} \frac{\partial \pi}{\partial x} \frac{\partial}{\partial \sigma} \tag{B.9}$$

$$\frac{\partial}{\partial y}\Big)_p = \frac{\partial}{\partial y}\Big)_\sigma - \frac{\sigma}{\pi} \frac{\partial \pi}{\partial y} \frac{\partial}{\partial \sigma} \tag{B.10}$$

and

$$\frac{\partial}{\partial p}\Big)_{x,y} = \frac{\partial}{\partial(\sigma\pi + P_T)}\Big)_{x,y} = \frac{1}{\pi} \frac{\partial}{\partial \sigma} \tag{B.11}$$

where the subscripts represent the variable held constant. Also, the total time derivative in sigma coordinates becomes

$$\frac{d()}{dt} = \frac{\partial()}{\partial t} + u \frac{\partial()}{\partial x} + v \frac{\partial()}{\partial y} + \dot{\sigma} \frac{\partial()}{\partial \sigma} . \tag{B.12}$$

Transforming the horizontal momentum equations to the vertical sigma coordinate yields

$$\frac{\partial u}{\partial t} + u \frac{\partial u}{\partial x} + v \frac{\partial u}{\partial y} + \dot{\sigma} \frac{\partial u}{\partial \sigma} - fv + \frac{\partial \phi}{\partial x} - \frac{\alpha}{\pi} \frac{\partial \pi}{\partial x} \frac{\partial \phi}{\partial \sigma} = F_u \tag{B.13}$$

and

$$\frac{\partial v}{\partial t} + u \frac{\partial v}{\partial x} + v \frac{\partial v}{\partial y} + \dot{\sigma} \frac{\partial v}{\partial \sigma} + fu + \frac{\partial \phi}{\partial y} - \frac{\alpha}{\pi} \frac{\partial \pi}{\partial y} \frac{\partial \phi}{\partial \sigma} = F_v \quad . \tag{B.14}$$

The hydrostatic equation can be written

$$\frac{\partial \phi}{\partial \sigma} = -\pi \alpha \tag{B.15}$$

in the sigma coordinate. The thermodynamic equation transformed to the sigma coordinate becomes

$$\frac{\partial}{\partial t} (C_p T) + u \frac{\partial}{\partial x} (C_p T) + v \frac{\partial}{\partial y} (C_p T) + \dot{\sigma} \frac{\partial}{\partial \sigma} (C_p T)$$

$$- \alpha \sigma \left(\frac{\partial \pi}{\partial t} + u \frac{\partial \pi}{\partial x} + v \frac{\partial \pi}{\partial y} \right) - \dot{\sigma} \pi \alpha = \dot{Q} + F_T \quad . \tag{B.16}$$

Finally, the continuity equation can be written as

$$\frac{\partial \pi}{\partial t} + u \frac{\partial \pi}{\partial x} + v \frac{\partial \pi}{\partial y} + \pi \frac{\partial u}{\partial x} + \pi \frac{\partial v}{\partial y} + \pi \frac{\partial \dot{\sigma}}{\partial \sigma} = 0 \tag{B.17}$$

in sigma coordinates. The equation of state remains unchanged. The set of equations can be summarized in vector form as follows:

(Momentum)

$$\frac{\partial \vec{V}}{\partial t} + \dot{\sigma} \frac{\partial \vec{V}}{\partial \sigma} + (f + \zeta)\ \hat{k} \times \vec{V} + \vec{\nabla} \left(\frac{\vec{V} \cdot \vec{V}}{2} + \phi\right)$$

$$+ \sigma \alpha \vec{\nabla} \pi = \vec{F} \tag{B.18}$$

(Hydrostatic)

$$\frac{\partial \phi}{\partial \sigma} = -\pi \alpha \tag{B.19}$$

(Continuity)

$$\frac{\partial \pi}{\partial t} + \vec{\nabla} \cdot (\pi \vec{V}) + \frac{\partial (\pi \dot{\sigma})}{\partial \sigma} = 0 \tag{B.20}$$

(Thermodynamic)

$$\frac{\partial (C_p T)}{\partial t} + \vec{V} \cdot \vec{\nabla} (C_p T) + \dot{\sigma}\ \frac{\partial (C_p T)}{\partial \sigma} - \alpha \sigma \left(\frac{\partial}{\partial t} + \vec{V} \cdot \vec{\nabla}\right)\pi$$

$$- \dot{\sigma} \pi \alpha = \dot{Q} + F_T \tag{B.21}$$

(Equation of State)

$$p\alpha = RT \tag{B.22}$$

(Definition of Sigma)

$$\sigma = \frac{P - P_T}{P_S - P_T} = \frac{P - P_T}{\pi} \tag{B.23}$$

where ζ is the relative vorticity given by $\zeta = \frac{\partial v}{\partial x} - \frac{\partial u}{\partial y}$, $\hat{k}$ is the vertical unit vector, and all $\vec{\nabla}$ operators are on a constant σ surface.

To put the equations into computationally convenient axisymmetric form, the horizontal cartesian x, y coordinates are transformed to cylindrical r, λ coordinates. During this transformation, the

axisymmetric assumption (i.e. $\frac{\partial}{\partial \lambda} = 0$) is invoked and the equations are combined with the continuity equation to yield the flux forms. The resulting system of equations can be written

(Radial Momentum)
$$\frac{\partial(\pi r u)}{\partial t} = -\frac{\partial(\pi r u \dot{\sigma})}{\partial \sigma} - \frac{\partial}{\partial r}(\pi r u^2) + \pi r v \left(f + \frac{v}{r}\right)$$
$$- \pi r \left(\frac{\partial \phi}{\partial r} + \sigma \alpha \frac{\partial \pi}{\partial r}\right) + \pi r F_u \qquad (B.24)$$

(Tangential Momentum)
$$\frac{\partial(\pi r v)}{\partial t} = -\frac{\partial(\pi r v \dot{\sigma})}{\partial \sigma} - \frac{\partial}{\partial r}(\pi r u v)$$
$$- \pi r u \left(f + \frac{v}{r}\right) + \pi r F_v \qquad (B.25)$$

(Hydrostatic)
$$\frac{\partial \phi}{\partial \sigma} = -\pi \alpha \qquad (B.26)$$

(Thermodynamic)
$$\frac{\partial(\pi r T)}{\partial t} = -\frac{\partial(\pi r T u)}{\partial r} - (P/P_o)^{R/C_p} \frac{\partial}{\partial \sigma}(\pi r \dot{\sigma} \theta)$$
$$+ \frac{\pi r \alpha \sigma}{C_p} \left(\frac{\partial}{\partial t} + u \frac{\partial}{\partial r}\right)\pi + \frac{\pi r}{C_P} \dot{Q} + \pi r F_T \qquad (B.27)$$

(Continuity)
$$\frac{\partial \pi}{\partial t} + \frac{\pi}{r}\frac{\partial(r u)}{\partial r} + u \frac{\partial \pi}{\partial r} + \frac{\partial}{\partial \sigma}(\pi \dot{\sigma}) = 0 \qquad (B.28)$$

(Equation of State)
$$p\alpha = RT \qquad (B.29)$$

(Poissons's Equation)
$$\theta = T\left(P_o/P\right)^{R/C_P} \qquad (B.30)$$

(Definition of Sigma)
$$\sigma = \frac{P-P_T}{P_S-P_T} = \frac{P-P_T}{\pi} \ . \qquad \text{(B.31)}$$

The first five equations in this set constitute a system of equations in the six variables u, v, T, ϕ, π and $\dot{\sigma}$. In order to close the system, the continuity equation (B.28) is replaced by two equations which are derived from it. First, the continuity equation is integrated through the depth of the model atmosphere from $\sigma = 0$ to $\sigma = 1$ and the boundary conditions $\dot{\sigma} = 0$ at $\sigma = 0$ and $\sigma = 1$ are imposed. The result is the surface pressure tendency equation given by

$$\frac{\partial(\pi r)}{\partial t} = - \frac{\partial}{\partial r} \int_0^1 (\pi r u) \ d\sigma' \quad . \qquad \text{(B.32)}$$

The second equation is obtained by integrating the continuity equation from $\sigma = 0$ to some level σ in the model atmosphere. The result is a modified form of the continuity equation given by

$$\pi r \dot{\sigma} = - \sigma \frac{\partial(\pi r)}{\partial t} - \frac{\partial}{\partial r} \int_0^\sigma (\pi r u) \ d\sigma' . \qquad \text{(B.33)}$$

Replacing the continuity equation with these two equations then yields a closed system of six equations in six unknowns. Knowing initial states for u, v, T and π, this system of equations is used to predict u, v, T, and π at some future time. The process can be summarized as follows:

1. Calculate the surface pressure tendency using B.32.

2. Calculate $\dot{\sigma}$ from B.33 using the result of step 1.

3. Calculate p using B.31.

4. Calculate α from B.29.

5. Use B.26 to compute ϕ using the results of steps 3 and 4.

6. Calculate the tendency of u and v from B.24 and B.25, respectively.

7. Compute θ from B.30.

8. Calculate the tendency of T from B.27 using the result of step 7.

9. Step forward in time to obtain new values of u, v, T and π.

10. Using these new values of u, v, T and π, repeat steps 1-9.

In order to use these continuous equations, they must be discretized. That is, finite difference forms of the equations were written for a 2-dimensional r, σ grid. The horizontal and vertical finite differencing schemes were designed following those schemes employed by Arakawa (1972) in the UCLA general circulation model. For a complete description of the horizontal and vertical differencing schemes, see Hack and Schubert (1976). As for the time differencing scheme, the initial step in the model is accomplished using the Matsuno (1966b) simulated backward difference method. Thereafter, the leapfrog scheme is used with an Asselin (1972) filter imposed to avoid separation of the odd and even time steps. A time step of 20 seconds was employed in this study.

APPENDIX C

Determination of K_{H_O}

In order to determine a reasonable value for K_{H_O}, the linear portion of the eddy diffusion coefficient, an analysis technique used by Hack and Schubert (1980) was undertaken. The analysis begins with a simplified form of the tangential momentum equation given by

$$\frac{\partial v}{\partial t} = K_{H_O} \left[\frac{1}{r} \frac{\partial}{\partial r} \left(r \frac{\partial v}{\partial r} \right) - \frac{v}{r^2} \right] \tag{C.1}$$

Recall that a first order Hankel transform pair is given by

$$g(r,t) = \int_0^\infty \hat{g}(k,t) \, J_1(kr) \, k \, dk$$

$$\tag{C.2}$$

$$\hat{g}(k,t) = \int_0^\infty g(r,t) \, J_1(kr) \, r \, dr$$

where $J_1(kr)$ is the Bessel function of the first kind of order 1 (Arfken, 1970). Then, the first order Hankel Transform of C.1 can be written

$$\int_0^\infty \frac{\partial v(r,t)}{\partial t} J_1(kr) \, r \, dr = K_{H_0} \left[\int_0^\infty \frac{1}{r} \frac{\partial v(r,t)}{\partial r} J_1(kr) \, r \, dr \right.$$

$$+ \int_0^\infty \frac{\partial}{\partial r} \left(\frac{\partial v(r,t)}{\partial r} \right) J_1(kr) \, r \, dr$$

$$\left. - \int_0^\infty \frac{v(r,t)}{r^2} J_1(kr) \, r \, dr \right] . \tag{C.3}$$

The integral on the left hand side of C.3 is simply the time derivative of the first order Hankel transform of $v(r,t)$. Integrating the first two integrals on the right hand side of (C.1) by parts yields the following simplification of C.3:

$$\frac{\partial \hat{v}(k,t)}{\partial t} = K_{H_0} \int_0^\infty v(r,t) \left[\frac{1}{r} \frac{\partial}{\partial r} \left(r \frac{\partial J_1(kr)}{\partial r} \right) - \frac{1}{r^2} J_1(kr) \right] r \, dr . \tag{C.4}$$

Using the definition of $J_1(kr)$ given by

$$J_1(kr) = \sum_{n=0}^\infty \frac{(-1)^n \left(\frac{kr}{2} \right)^{2n+1}}{n! \, (n+1)!} \tag{C.5}$$

the terms within brackets in equation C.4 can be written as $-k^2 J_1(kr)$. Therefore,

$$\frac{\partial \hat{v}(k,t)}{\partial t} = -K_{H_0} \int_0^\infty v(r,t) \, k^2 \, J_1(kr) \, r \, dr \tag{C.6}$$

or, since k^2 can be brought outside the integral,

$$\frac{\partial \hat{v}(k,t)}{\partial t} = -k^2 \, K_{H_0} \, \hat{v}(k,t) . \tag{C.7}$$

The solution to (C.7) is given by

$$\hat{v}(k,t) = \hat{v}(k,t=0) \exp\left[-k^2 K_{H_o} t\right] \tag{C.8}$$

where $\hat{v}(k,t=0)$ represents the transformed initial condition of the tangential wind field. The solution in physical space is obtained by multiplying (C.8) by $J_1(kr)$ k and integrating the equation over all k from 0 to ∞. The inverse transformed solution is then given by

$$v(r,t) = \int_0^\infty \hat{v}(k,t=0) \exp\left[-k^2 K_{H_o} t\right] J_1(kr) \; k \; dk. \tag{C.9}$$

If an initial tangential wind field is assumed whose shape is given by

$$v(r,t=0) = \overset{*}{V} \frac{r}{r_o} \exp\{\tfrac{1}{2}[1-\tfrac{1}{3}\tfrac{r^2}{r_o^2}]\} \tag{C.10}$$

where $\overset{*}{V}$ is some amplitude factor, then the first order Hankel transform of this field as can be written

$$\int_0^\infty v(r,t=0) \; J_1(kr) \; r \; dr = \int_0^\infty \overset{*}{V} \frac{r}{r_o} \exp\{\tfrac{1}{2}[1-\tfrac{1}{3}\tfrac{r^2}{r_o^2}]\} \; J_1(kr) \; r \; dr. \tag{C.11}$$

After performing the integral on the right hand side, (Erdelyi et al., 1954) C.11 can be written

$$\hat{v}(k,t=0) = 9 \overset{*}{V} r_o^3 \; k \; \exp\{\tfrac{1}{2}[1-3r_o^2 \; k^2]\} \quad . \tag{C.12}$$

Then, substituting this expression into equation C.9, and performing the integral on the right hand side, the final expression for $v(r,t)$ is

$$v(r,t) = \overset{*}{V} \left(\frac{r}{r_o}\right) \frac{1}{\left(1+\frac{2K_H t}{3r_o^2}\right)^2} \exp\left[\frac{1}{2}\left\{1-\frac{r^2}{r_o^2}\left(\frac{1}{3+\frac{2K_H t}{r_o^2}}\right)\right\}\right]. \qquad (C.13)$$

The assumed initial tangential wind field is shown in Figure C1. This profile was assumed because it can be thought to fairly accurately represent what the tangential wind field might be around a thermally induced cyclone over the desert. Most of the energy is concentrated in the broad region from $r = 0$ to $r = 6\,r_o$ where the heat source is most intense. At the outer edges of the desert and over the ocean $(r > 6\,r_o)$, there is little energy as might be expected. Also, shown in Figure C1 is the tangential velocity field at several times after the initial time $t = 0$. As the dissipation occurs, it acts most rapidly on the portion of the wind field where the velocity is greatest.

Now, by defining a measure of kinetic energy as

$$KE(t) = \int_o^\infty \frac{1}{2} v^2(r,t)\ r\ dr \qquad (C.14)$$

the ratio of kinetic energy at time t to that at time t=0 can be computed. The ratio is
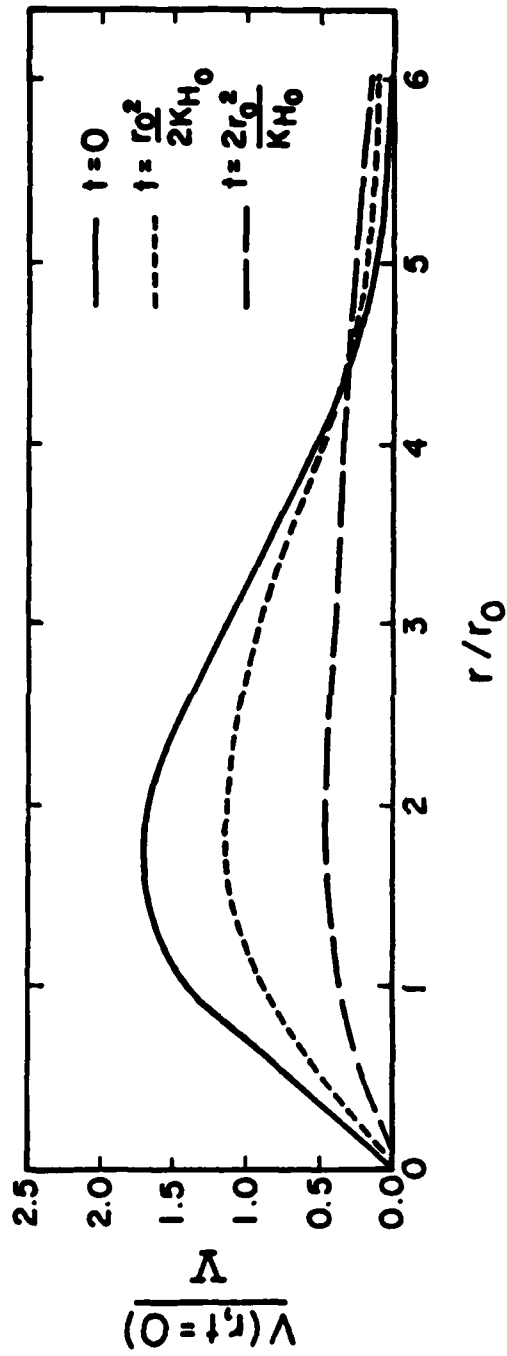
Figure C.1 Assumed initial radial distribution of the tangential wind field and the radial distribution at two later times.

$$\frac{KE(t)}{KE(t=0)} = \frac{\int_0^\infty \frac{1}{2}\{V^* \left(\frac{r}{r_o}\right) \frac{1}{\left(1+\frac{2K_{H_o}t}{3r_o^2}\right)^2} \exp\left[\frac{1}{2}\{1-\frac{r^2}{r_o^2}\left(\frac{1}{3+\frac{2K_{H_o}t}{r_o^2}}\right)\}\right]\}^2 r\ dr}{\int_0^\infty \frac{1}{2}\{V^* \left(\frac{r}{r_o}\right) \exp[\frac{1}{2}(1-\frac{r^2}{3r_o^2})]\}^2\ r\ dr}$$

(C.15)

or

$$\frac{KE(t)}{KE(t=0)} = \frac{1}{\left(1+\frac{2K_{H_o}t}{3r_o^2}\right)^2}$$

(C.16)

This ratio of kinetic energy at time t to the initial kinetic energy will be used to try to determine a reasonable range for K_{H_o}. To do so, it is necessary to estimate how much energy may be available in a day which would need to be dissipated. The primary heat source over the desert is the sensible heat flux from the desert surface to the atmosphere. The net 24 hour sensible heating can be written as

$$NET_{24}\ SEN = \sum_{k=1}^{24} S_k\ \Delta t$$

(C.17)

where S_k is the sensible heat flux from the surface at hour k and Δt is the time over which that sensible heat flux is valid (one hour). Using the parameterized values of sensible heating (see Chapter 4) for a clear atmosphere over the desert, the net 24 hour sensible energy flux is calculated to be about 10^7 J m^{-2}. Assuming this energy is input into the atmosphere over the first

360 km from the center of the model, the net sensible energy received by the atmosphere in a 24 hour period is given by $(10^7 \text{ J m}^{-2})*$ $*[\pi (360000\text{m})^2] = 4.09 \times 10^{18}$ J. Now, assume this energy is input into the well mixed layer of the atmosphere. Most of the sensible heat flux occurs during the period when the mixed layer is well developed. By assuming the depth of the well mixed layer is about 350 mb, the mass of this layer is computed to be about 1.45×10^{15} kg and therefore, the energy supplied per unit mass is about 2816 m^2s^{-2}. It is assumed that only a portion of this energy would be translated into tangential wind speed. Some of the energy will be consumed in producing radial wind speed, vertical convection, and increasing the temperature of the air. As a lower limit 1% or ~28.2 m^2s^{-2} is assumed and as an upper limit 25% or ~703 m^2s^{-2} is assumed. The average tangential component of wind speed which would result in each case can then be computed from the classical definition of kinetic energy per unit mass given by $KE_c = \frac{1}{2}\bar{v}^2$. The lower limit case yields an average wind speed of 7.50 m/s and the upper limit case yields an average wind speed of 37.52 m/s. Therefore, without dispersion, in one day the sensible energy could cause average tangential wind speed increases of between 7.5 and 37.5 m/s over the normally observed values of ~10 m/s. The average wind speed for the assumed initial tangential wind field can be defined as

$$\bar{v}(t=0) = \frac{\int_0^\infty V^* \frac{r}{r_0} \exp[\frac{1}{2}(1 - \frac{r^2}{3r_0^2})] \, r \, dr}{\int_0^\infty r \, dr} \tag{C.18}$$

and therefore, it is always possible to determine a V* amplitude factor
which would yield the mean wind speeds associated with the upper and
lower limits discussed above. Also, an amplitude factor for the case
with a mean wind speed equal to the normally observed value of ~10
m/s could be determined. For each of these cases, the kinetic energy
defined by (C.14) can then be calculated. Finally, knowing the
kinetic energy associated with the normally observed flow (10 m/s) and
the kinetic energy associated with the upper and lower limit cases
(47.5 and 17.5 m/s) above, one could compute the ratio between the
kinetic energy associated with the normally observed flow and the
upper and lower limit cases of the undispersed flow. These values
have been calculated and are presented in Table C1. Since tangential
winds in excess of about 10 m/s are not normally observed over the
desert, it is reasonable to expect the horizontal dispersion process
to be strong enough to be able to diminish the kinetic energy in one
day from the value it would have in the nondispersed cases to the
normally expected value. Therefore, using equation C.16, assuming
r_o is approximately 1/10 of the total radial expanse of the mixed
layer (i.e. r_o = 36000m), with t = 86400s a range of values can be
computed within which K_{H_o} should lie. For the lower limit
K_{H_o} = 16871 m^2s^{-1} and for the upper limit, K_{H_o} = 84400 m^2s^{-1}. The
intermediate value of 50000 m^2s^{-1} has been chosen which is within
the range of 1000 m^2s^{-1} to 100000 m^2s^{-1} which have been reported
in previous numerical studies (Ooyama,1969; Fingerhut,1978). The value
of 50000 m^2s^{-1} was used within the mixed layer over the desert.
Outside this desert mixed layer, a value of 5000 m^2s^{-1} was used

TABLE C.1

Amplitude factor (V) and kinetic energy (KE) associated with the mean
wind speeds ($\bar{v}$) and the ratio of the kinetic energy for the 10 m/s
mean wind speed case to the kinetic energy in the other mean wind
speed cases.

$\bar{v}(m\ s^{-1})$	$V^{*}\ (m\ s^{-1})$	$KE\ (m^2 s^{-2} r_o^2)$	$\dfrac{KE\ (10\ m\ s^{-1})}{KE\ (\bar{v})}$
10	16.76	3435.38	1.0
17.5	29.33	10520.84	.3266
47.5	79.64	77575.99	.0443

in the assumption that the dispersion processes are much more important within the mixed layer than elsewhere in the model domain.

END

FILMED

10–84

DTIC